Technische Universität München

Ingenieurfakultät Bau Geo Umwelt

Lehrstuhl für Statik

Aeroelastic Modeling and Simulation for the Assessment of Wind Effects on a Parabolic Trough Solar Collector

Michael S. Andre

Vollständiger Abdruck der von der Ingenieurfakultät Bau Geo Umwelt der Technischen Universität München zur Erlangung des akademischen Grades eines

Doktor-Ingenieurs

genehmigten Dissertation.

Vorsitzender:

Prof. Dr.-Ing. habil. Fabian Duddeck

Prüfer der Dissertation:

1. Prof. Dr.-Ing. Kai-Uwe Bletzinger
2. Prof. Dr. Rainald Löhner
3. Prof. Riccardo Rossi, Ph.D.

Die Dissertation wurde am 16.01.2018 bei der Technischen Universität München eingereicht und durch die Ingenieurfakultät Bau Geo Umwelt am 09.05.2018 angenommen.

Schriftenreihe des Lehrstuhls für Statik TU München

Band 37

Michael Andre

AEROELASTIC MODELING AND SIMULATION FOR THE ASSESSMENT OF WIND EFFECTS ON A PARABOLIC TROUGH SOLAR COLLECTOR

München 2018

Veröffentlicht durch

Kai-Uwe Bletzinger
Lehrstuhl für Statik
Technische Universität München
Arcisstr. 21
80333 München

Telefon: +49(0)89 289 22422
Telefax: +49(0)89 289 22421
E-Mail: kub@tum.de
Internet: www.st.bgu.tum.de

ISBN: 978-3-943683-50-9

Abstract

In the first part of this work, a modeling and simulation approach for computational wind engineering is presented for the estimation of structural wind loads. The model is applied to a parabolic trough solar collector where it is validated with a boundary layer wind tunnel experiment for the evaluation of mean, root mean square and peak wind loads in a simulated atmospheric boundary layer.

In the second part of this work, the numerical approach is extended to include fluid-structure interaction and an analytical model problem is presented for benchmarking fluid-structure interaction algorithms. The presentation includes a survey and assessment of some partitioned procedures and an analysis of the temporal accuracy and stability for the selected time discretizations: the generalized-α method for the structure and the second-order backward difference formula for the fluid. After assessing its accuracy and stability, the fluid-structure interaction solver is applied to the aeroelastic simulation of a parabolic trough solar collector.

The aeroelastic study of the parabolic trough solar collector conducted in this work goes beyond existing studies found in the literature by considering feedback effects of the structural motion on the wind loads. It is shown that significant self-excited vibrations can occur when the collector is exposed to vortex shedding from its leading edge. The extensive numerical results are used to provide insight into the synchronization of vortex shedding with the vibration of the collector. The current analysis is discussed in the context of existing literature on self-excited vibrations. Additionally, fluid-structure interaction simulation is compared with the classical technique in which the aerodynamic damping is estimated by controlled periodic oscillations. The strengths and weaknesses of both approaches are discussed.

Zusammenfassung

Der erste Teil dieser Arbeit beschäftigt sich mit der Entwicklung und Validierung einer numerischen Vorgehensweise für die prädiktive Ermittlung von Windlasten. Diese wird zur Berechnung eines Solarrinnenkollektors eingesetzt. Mittelwerte, quadratische Mittelwerte und Höchstwerte der in einer simulierten atmosphärischen Grenzschicht ermittelten aerodynamischen Beiwerte werden mit Ergebnissen von einem Windkanalversuch verglichen.

Im zweiten Teil dieser Arbeit wird die vorgeschlagene Herangehensweise erweitert, um Fluid-Struktur-Wechselwirkung zu simulieren, und ein analytisches Modell wird präsentiert, um ausgewählte Kopplungsalgorithmen zu evaluieren. Die Darstellung beinhaltet eine systematische Bewertung der Kopplungsverfahren und eine Untersuchung der Stabilität und Genauigkeit für die gewählten Zeitdiskretisierungen: die Generalized-α-Methode für die Struktur und der Rückwärtsdifferenzenquotient zweiter Ordnung für das Fluid. Nach der Überprüfung der Genauigkeit und Stabilität wird die komplette Implementierung eingesetzt, um eine aeroelastische Simulation des Rinnenkollektors durchzuführen.

Die aeroelastische Analyse des Rinnenkollektors geht über bisherige Untersuchungen von Rinnenkollektoren hinaus, indem die Rückkopplung der Bewegung der Struktur auf die Windlasten berücksichtigt wird. Es wird gezeigt, dass erhebliche aeroelastische Effekte auftreten können, wenn ein wesentlicher Teil der Belastung durch den Wirbelablösungsprozess an der Vorderkante entsteht. Die umfangreichen numerischen Ergebnisse werden detailliert ausgewertet, um Einsicht in die Synchronisierung des Wirbelablösungsprozesses mit der Vibration des Rinnenkollektors zu gewinnen. Die numerischen Ergebnisse werden im Zusammenhang mit der Fachliteratur über aeroelastische Effekte diskutiert. Des Weiteren wird die moderne Fluid-Struktur-Wechselwirkungssimulation mit dem klassischen Verfahren, in dem die aerodynamische Dämpfung durch kontrollierte periodische Schwingungen ermittelt wird, verglichen. Die Vor- und Nachteile beider Verfahren werden dabei erläutert.

Acknowledgments

This work would not have been possible without the support of a number of people and organizations. Firstly, I wish to acknowledge Prof. Dr.-Ing. Kai-Uwe Bletzinger for providing me with the opportunity to work as a member of the Chair of Structural Analysis. I would like to thank PD Dr.-Ing. habil. Roland Wüchner for always taking the time for discussions and for his interest in my work. I would like to thank Abengoa for funding a large part of my research and the examiners for their efforts in reviewing my thesis. I would also like to express my gratitude to my colleagues, both at the Chair of Structural Analysis and at the International Center for Numerical Methods in Engineering, Barcelona, for their support and for the numerous discussions, but, above all, I wish to thank them for motivating and inspiring me through their enthusiasm and dedication to their work. I would also like to express my gratitude to the Leibniz Supercomputing Center for providing the cluster resources on which many of the results presented in this thesis were computed. Finally, I wish to thank my family, who have supported and encouraged me at every step.

Michael Andre
Technische Universität München
December, 2017

Contents

Contents vii

List of Abbreviations xi

List of Symbols xiii

1 Introduction 1

2 Simulation of Natural Wind 5
2.1 Surface Layer Characteristics 5
2.2 Wind Gust Statistics 6
2.3 Synthetic Wind Generator 8
2.3.1 Generation of Time-Varying Wind 8
2.3.2 Linearized Model of Turbulent Shear Flow 11
2.3.3 Library Implementation 14

3 Large-Eddy Simulation 19
3.1 Finite Element Formulation 19
3.2 Near Wall Model 23
3.3 Backward-Facing Step 25

4 Boundary Layer Wind Tunnel Validation 29
4.1 Experimental Setup 30

4.2 Computational Setup 32
4.3 Wind Simulation 35
4.3.1 Generation of Inlet Data 35
4.3.2 Empty Channel Simulation 35
4.4 Wind Load Simulation 38
4.5 Summary 42

5 Fluid-Structure Interaction 47
5.1 Analytical Model Problem 50
5.1.1 Inviscid Fluid Problem 51
5.1.2 Membrane Problem 53
5.1.3 Beam Problem 54
5.1.4 Viscous Fluid Problem 55
5.2 Time-Discrete Problem 56
5.3 Iterative Coupling 60
5.3.1 Relaxation 64
5.3.2 Interface Compressibility 67
5.3.3 Variation of Mesh Resolution 69
5.3.4 Performance of Coupling Algorithms 72
5.4 Staggered Coupling 74
5.5 Verification of Mesh Motion Solver 78
5.5.1 Description of Mesh Motion Solver 78
5.5.2 Flow-Induced Vibration of a Flexible Beam 81
5.6 Summary 88

6 Aeroelastic Simulation 91
6.1 Section Model 92
6.2 Dimensional Analysis 94
6.3 Equation of Motion 96
6.4 One-Way and Two-Way Coupling 96
6.5 Design of Experiment 97
6.6 Full-Scale Wind Simulation 101
6.7 Effect of Varying Pitch Angle 101
6.8 Wind-Excited Response for Pitch Angle $\alpha = 60^o$ 106
6.8.1 Comparison of One-Way and Two-Way Solutions 106
6.8.2 Synchronization Process 108
6.9 Wind-Excited Response for Pitch Angle $\alpha = 90^o$ 111
6.9.1 Comparison of One-Way and Two-Way Solutions 111

6.9.2 Synchronization Process 113
6.10 Wind-Excited Response for Pitch Angle $\alpha = 120^o$ 114
6.11 Effect of Varying Reduced Velocity 116
6.11.1 Controlled-Oscillation Simulation 118
6.11.2 Two-Way Coupled Analysis 120
6.12 Summary 122

7 Conclusions and Outlook 123

A Calculation of Statistics 125
A.1 Mean Velocity 125
A.2 Standard Deviation 125
A.3 Spectral Density 126
A.4 Autocorrelation 126

B Viscous Fluid-Structure Interaction Model Problem 127

Bibliography 133

List of Abbreviations

ABL	Atmospheric Boundary Layer
API	Application Program Interface
BDF	Backward Difference Formula
BLWT	Boundary Layer Wind Tunnel
CFD	Computational Fluid Dynamics
CSM	Computational Structural Mechanics
CR	Constant Relaxation
CWE	Computational Wind Engineering
DES	Detached Eddy Simulation
DFT	Discrete Fourier Transform
FEM	Finite Element Method
FSI	Fluid-Structure Interaction
HDF	Hierarchical Data Format
IBL	Internal Boundary Layer

IC	Interface Compressibility
LES	Large Eddy Simulation
MPI	Message Passing Interface
OSS	Orthogonal Subgrid Scales
PTSC	Parabolic Trough Solar Collector
RANS	Reynolds-Averaged Navier-Stokes
RMS	Root Mean Square
SDOF	Single Degree of Freedom
VMM	Variational Multiscale Method

List of Symbols

$(\cdot)_i$	i^{th} vector component
$(\cdot)_{ij}$	matrix component at i^{th} row and j^{th} column
$\overline{(\cdot)}$	mean value
$(\cdot)'$	$(\cdot)-\overline{(\cdot)}$
$\hat{(\cdot)}$	Fourier coefficient
$\tilde{(\cdot)}$	intermediate variable
$(\cdot)^*$	complex conjugate
$(\cdot)^n$	value at n^{th} time step
$(\cdot)^m$	value at m^{th} iteration step
$(\cdot)^\alpha$	power law exponent in (2.3)
$(\cdot)_h$	finite element function
$[\cdot]^d$	space of functions with values in $\mathbb{R}^d$
$(\cdot)_s$	property of the structure problem
$(\cdot)_f$	property of the fluid problem

$(\cdot)_{,t}$	$d(\cdot)/dt$
$\|\|\cdot\|\|_0$	Norm defined in (5.77)
$\|\|\cdot\|\|_1$	Norm defined in (5.78)
$\mathcal{L}[\cdot]$	Laplace transform
∇	gradient operator
$\nabla\cdot$	divergence operator
α	collector pitch angle
α_f	generalized-α parameter defined in (5.46)
α_{fs}	added-mass ratio
$\overline{\alpha}_{fs}$	upper bound of stable added-mass ratios
α_m	generalized-α parameter defined in (5.46)
β	Newmark parameter defined in (5.47)
β_{LT}	dimensionless eddy lifetime defined in (2.11)
β_{SC}	staggered coupling parameter in (5.85)
γ	Newmark parameter defined in (5.47)
γ_{IC}	interface compressibility parameter in (5.73)
δ	distance between mirror vertex and rotation axis in figure 6.1
$\delta_t(\cdot)$	discrete time derivative
$\boldsymbol{\epsilon}(\cdot)$	$(\nabla(\cdot)+\nabla(\cdot)^T)/2$
ϵ	dimensionless viscous FSI parameter defined in (5.33)
ϵ^*	dimensionless viscous FSI parameter defined in (5.33)
ζ	mechanical damping ratio
ζ_a	aerodynamic damping ratio
η	relaxation parameter
θ	angle of collector rotation
θ_0	amplitude of controlled oscillation in (6.8)
κ	von Kármán constant ($\kappa = 0.4$)
μ	dynamic viscosity
ν	kinematic viscosity
$\boldsymbol{\xi}$	distance vector between two points
$\boldsymbol{\pi}_{hc}, \boldsymbol{\pi}_{hp}, \pi_{hd}$	subscale projections in (3.9), (3.10), (3.11)

π_i	dimensionless π-groups in (6.2)
ρ	mass density
$\rho(\boldsymbol{A})$	spectral radius of $\boldsymbol{A}$
ρ_u	autocorrelation of streamwise velocity defined in (2.9)
ρ_∞	spectral radius of the generalized-α method
$\boldsymbol{\sigma}$	Cauchy stress tensor
σ_s	tension
σ_u	standard deviation of streamwise velocity
τ	dimensionless time defined in (5.33)
τ_{dyn}	time step stabilization parameter in (3.12)
τ_0	ground shear stress in (2.2)
τ_1, τ_2	stabilization parameters in (3.12), (3.13)
ϕ	scalar potential
$\boldsymbol{\psi}_h$	finite element mesh displacement
ψ_z	stream function
ω_n	angular wetted natural frequency $\omega_n = 2\pi f_n$
ω_{n0}	angular natural frequency in vacuum $\omega_{n0} = 2\pi f_{n0}$
ω_z	z-component of vorticity
Γ_D	Dirichlet boundary
Γ_{fs}	fluid-structure interface
Γ_i	inlet boundary
Γ_s	slip boundary
Γ_{LT}	anisotropic eddy lifetime parameter in (2.11)
Γ_o	outlet boundary
Γ_w	wall boundary
$\Delta\boldsymbol{k}$	$(2\pi)^{3/2}/\sqrt{L_x L_y L_z}$
Δt	time step size
Δx_i	grid spacing in the i^{th} direction
$\boldsymbol{\Phi}$	spectral tensor defined in (2.6)
Ψ_z	stream function coefficient in (B.16)
Ω_f	fluid domain
Ω_h	meshed domain

$\overline{\Omega}_h$	closure of Ω_h
$\partial\Omega_h$	boundary of Ω_h
Ω_z	vorticity coefficient in (B.9)
a	interface amplitude
c_{p-k}	k^{th} coefficient of $p_{\boldsymbol{A}}$ in (5.54)
$\det(\boldsymbol{J}_K)$	determinant of the Jacobian of the simplex $K \in \mathcal{T}_h$
d_s	interface normal displacement
$\boldsymbol{d}_s$	structural displacement
$\boldsymbol{d}_s$	vector of nodal structural displacements
f	frequency in cycles per second
$\hat{f}$	modal interface force
$\boldsymbol{f}$	vector of nodal forces on Γ_{fs}
$\boldsymbol{f}_B$	body force per unit mass
f_n	wetted natural frequency in cycles per second
f_{n0}	natural frequency in vacuum in cycles per second
f_o	frequency of oscillation in cycles per second
$\boldsymbol{f}_p$	predictor for $\boldsymbol{f}$ defined in (5.82)
f_{sh}	vortex shedding frequency in cycles per second
h	characteristic mesh size
h_s	structural thickness
i	imaginary unit $i = \sqrt{-1}$
k	wave number $k = \lvert\boldsymbol{k}\rvert$
$\boldsymbol{k}$	wave vector
k_θ	torsional stiffness
m_r	added-mass ratio defined in section 6.2 ($m_r = \rho LW^4/J$)
$\boldsymbol{n}$	surface normal vector
$\boldsymbol{n}(\boldsymbol{k})$	independent Gaussian complex random vector of unit variance
p	pressure
$\boldsymbol{p}$	vector of nodal pressures
p_p	pressure from the potential solution in (B.28)
p_v	viscous pressure correction in (B.26)

$p_{\boldsymbol{A}}$	characteristic polynomial of $\boldsymbol{A}$ in (5.54)
r	scalar residual
$\boldsymbol{r}$	residual vector
t	time or time-distance
$\boldsymbol{t}$	traction vector
$\boldsymbol{u}$	vector of nodal velocities
$\boldsymbol{u}$	fluid velocity vector
$\boldsymbol{u}_p$	irrotational fluid velocity vector ($\boldsymbol{u}_p = \nabla\phi$)
$\boldsymbol{u}_v$	viscous fluid velocity correction ($\boldsymbol{u}_v = \boldsymbol{u} - \boldsymbol{u}_p$)
u_*	friction velocity in (2.2)
u_{cr}	critical velocity
$\boldsymbol{u}_D$	prescribed velocity
u, v, w	fluid velocity components
$\boldsymbol{x}$	spatial coordinate
y_w	wall distance
z	height above the ground
z_0	roughness height
z_{ref}	reference height
$\boldsymbol{A}$	amplification matrix
B	width of solar collector module
$\boldsymbol{C}(\boldsymbol{k})$	synthetic wind generator matrix defined in (2.14)
C_D	drag coefficient defined in (4.2)
C_f	friction coefficient ($\tau_0 = \frac{1}{2}\rho U_\infty^2 C_f$)
C_L	lift coefficient defined in (4.3)
C_M	moment coefficient defined in (6.5)
C_{M_b}	base moment coefficient defined in (4.4)
$\mathcal{C}^0$	space of continuous functions
D	characteristic eddy dimension
$\boldsymbol{D}$	finite element divergence operator
E	Young's modulus
$E(k)$	von Kármán spectrum at wavenumber k
E_0	von Kármán spectrum scaling parameter in (2.10)

F_x	drag force
F_z	lift force
$\mathcal{F}$	fluid operator mapping displacements to forces on Γ_{fs}
${}_2F_1$	hypergeometric function
$\boldsymbol{G}$	finite element gradient operator
H	height of the pitching axis above the ground
H_s	backward facing step height
J	moment of inertia
$\boldsymbol{J}_K$	Jacobian of the simplex $K \in \mathcal{T}_h$
L	structural wave length (length unit in (6.1))
$\boldsymbol{L}$	Laplacian approximation of $\boldsymbol{L} \approx \boldsymbol{D}\boldsymbol{M}^{-1}\boldsymbol{G}$
L_i	domain dimension in the i^{th} direction
L_{iso}	isotropic turbulence length scale parameter
$\boldsymbol{M}$	finite element mass matrix
M	moment about pitching axis (mass unit in (6.1))
M_b	moment about collector base shown in figure 4.1
N	number of terms in a sequence
N_{corr}	number of fractional-step pressure corrections
N_{dof}	number of degrees of freedom
N_{el}	number of elements
N_i	number of grid points in the i^{th} direction
$\mathbb{P}_k$	space of functions spanned by polynomials of degree k
R	radius
Q_h	pressure finite element space defined in (3.5)
$\tilde{Q}_h$	scalar finite element space defined in (3.2)
$\boldsymbol{R}$	covariance tensor defined in (2.5)
$\mathcal{R}$	relaxation operator in (5.60)
$\mathbb{R}$	space of real numbers
$\mathcal{S}$	structural operator mapping forces to displacements on Γ_{fs}
S_{C_M}	one-sided spectrum of moment coefficient
S_u, S_v, S_w	one-sided spectra of velocity components defined in (2.8)
S_θ	one-sided spectrum of angle of rotation

T	simulation time or period of oscillation (time unit in (6.1))
$\mathcal{T}_h$	finite element mesh with characteristic size h
$T.I.$	streamwise turbulence intensity defined in (2.7)
U_∞	freestream velocity
U_B	bulk velocity
U_r	reduced velocity $U_r = U_{ref}/W f_n$
$U_{r,cr}$	critical reduced velocity
U_{ref}	streamwise reference velocity at height z_{ref}
V_h	velocity finite element test space defined in (3.4)
$\tilde{V}_h$	vector finite element space defined in (3.1)
W	mirror aperture
W_h	velocity finite element solution space defined in (3.3)

The purpose of computing is insight, not numbers.

Richard Hamming

Chapter 1

Introduction

Computational wind engineering (CWE) is increasingly being applied to microscale flow problems, including structural wind engineering, since its inception nearly 50 years ago [14]. Its emergence has provided researchers and practitioners with a new tool, enabling the unrestricted measurement of data at arbitrary scale and the preliminary assessment of structural wind loads for design.

Despite its potential, computational fluid dynamics (CFD) is not commonly used in structural wind engineering. According to [15], this is due to a limited knowledge about the estimation of wind loads using CFD models and the required complexity of the (time-dependent) models themselves. In contrast to environmental wind engineering problems, time-dependent analysis is generally required for structural wind engineering in order to predict peak pressures and wind loads [14, 107]. Tamura et. al. [107] further emphasize the importance of modeling inflow turbulence for wind load estimation. This is similar to boundary layer wind tunnel (BLWT) experiments, which use spires and roughness elements to simulate the turbulent characteristics of the upstream flow. In fact, some numerical studies have directly modeled the BLWT to simulate the approaching flow [108, 115].

Figure 1.1: A parabolic trough solar collector [61].

In order to advance the field, further research into two important aspects is required:

1. the development of comprehensive numerical models,

2. extensive experimental validation and cross-comparison between numerical approaches.

Previous contributions to this research include a 29 m umbrella [73], the Silsoe cube [62], the long-span roof of the Shenzhen railway station [68], low-rise buildings [45, 88], high-rise buildings [80, 87, 108], the CAARC tall building model [34] and a building with a setback [115].

The current work centers around the application of the finite element method (FEM) for the large-eddy simulation (LES) of wind loads on a parabolic trough solar collector (PTSC) (figure 1.1). It includes modeling and simulation of a neutrally-stable atmospheric boundary layer (ABL), the validation of mean, root mean square (RMS) and peak wind loads with experimental data from a BLWT, the development of an analytical fluid-structure interaction (FSI) benchmark problem, an assessment of several partitioned FSI coupling algorithms and a complete aeroelastic study of a PTSC section model in a simulated ABL flow at full scale. Using the validated numerical model, the range of reduced velocities and pitch angles for which self-excited vibrations can occur is identified and the mechanism of self-excited vibration is described by a detailed analysis of the numerical simulation results.

The remaining chapters in this thesis are organized as follows:
CHAPTER 2 discusses properties of the ABL that affect structural wind loads. Modeling assumptions and simplifications are presented, several turbulence statistics used throughout this work are defined, and the method used for simulating the ABL is described.
CHAPTER 3 describes the FEM discretization used for LES in this work. The description includes the complete set of equations solved at each time step and the definition of the subgrid scale terms. The near wall modeling problem is discussed, and the chosen numerical approach is tested using a backward-facing step experiment.
CHAPTER 4 presents a validation study for the simulation of wind loads on a PTSC. The ability of the numerical model to reproduce the turbulence statistics observed in a BLWT is investigated, a mesh refinement study is performed to assess the sensitivity of the estimated wind loads to the mesh size, and the wind load statistics are compared with BLWT measurements for 9 pitch angle configurations.
CHAPTER 5 discusses FSI in the context of wind engineering. The analytical model problem is presented and subsequently used to assess the accuracy, stability and efficiency of several partitioned coupling procedures. The chapter concludes with a nonlinear benchmark problem and an assessment of the mesh motion scheme used in this work.
CHAPTER 6 proceeds with the aeroelastic study of the PTSC in a simulated ABL. The need for an aeroelastic study is first justified by a review of existing knowledge found in the literature. This is followed by a discussion of the section model and a dimensional analysis of the parameters used for the current study. One-way and two-way coupled simulations are used to quantify the amplification of the response due to feedback effects of the structural motion. The self-excitation mechanism is then explained through a detailed analysis of the numerical results. It is shown that the observed results are consistent with the existing knowledge of self-excited vibrations found in the literature. Finally, the aerodynamic damping is estimated through a controlled-oscillation simulation in a smooth flow and is shown to be consistent with the onset of self-excited vibrations in ABL flow as predicted by the FSI simulations.
CHAPTER 7 summarizes the outcomes of this work and provides some recommendations for future studies.

The publications [5, 7, 8] have resulted from this thesis work.

Chapter 2

Simulation of Natural Wind

2.1 Surface Layer Characteristics

For the simulation of structural wind loads, wind effects in the region of the ABL closest to the ground need to be modeled. This region is referred to as the surface layer. It extends 50-100 m above the ground and is characterized by constant shear stress in the vertical direction [57].

Within this layer, wind effects depend on the shear stresses resulting from the friction of the earth and on the vertical gradient of temperature. At high wind speeds, the buoyancy forces due to temperature gradients are small compared to surface driven friction forces and may therefore be neglected for structural wind load simulations. This condition corresponds to a Richardson number equal to zero, and the surface layer is said to be neutrally stable.

Ground friction is affected by pressure drag, which normally dominates viscous surface drag [119]. Pressure drag refers to pressure differences across obstacles, ranging from soil and grass to forest and urban canopies, that act as a momentum sink. The local terrain type is characterized by a roughness height z_0, which strongly influences the turbulent conditions in the vicinity of the structure and the resulting wind loads. Its value for

various terrain categories is reviewed in detail by [119].

Under the conditions of neutral stability, homogeneous roughness of the upstream terrain and stationary turbulence, the variation of the mean velocity with height follows the widely known logarithmic profile

$$\bar{u}(z) = \frac{u_*}{\kappa} \ln\left(\frac{z}{z_0}\right) \tag{2.1}$$

with $\kappa \approx 0.4$ the von Kármán constant. The friction velocity u_* is related to the shear stress on the ground by

$$\tau_0 = \rho\, u_*^2 \tag{2.2}$$

and depends on both the terrain and wind speed [57].

An alternative to (2.1), which is commonly used in wind engineering, is the power law

$$\bar{u}(z) = U_{ref}\left(\frac{z}{z_{ref}}\right)^{\alpha} \tag{2.3}$$

where the exponent α may be computed for a given value of z_0 by a curve fitting of (2.1).

The suitability of (2.1) or (2.3) depends on the distance of the upstream fetch over which the roughness is approximately uniform. A sudden change in the upstream roughness results in an internal boundary layer (IBL), identified by a discontinuity in the velocity gradient $\frac{\partial \bar{u}}{\partial z}$. The growth of the IBL is generally considered to be consistent with the growth of a turbulent boundary layer over a smooth flat plate, which was shown by [97] to scale with $x^{0.8}$ [41]. If the height of the structure is comparable to the height of the IBL, the mean profile may be better approximated by a modified power law [116]. In the remainder of this work, only uniform roughness conditions are considered.

2.2 Wind Gust Statistics

In structural wind engineering, the mean velocity is used to describe the component of velocity that varies gradually over the course of several hours or days as a result of changes in weather. Superimposed on this are time-resolved fluctuations or wind gusts with time scales on the order of seconds

and minutes. Gust-induced wind loading, also referred to as buffeting, is a form of externally-induced excitation [77]. It contributes to the overall peak wind loads and may cause resonant excitation of structures if the structural eigenfrequencies coincide with the buffeting frequencies, which are described by the gust spectrum (also discussed below). If dynamic effects are negligible, the time-varying fluctuations may be combined with the mean load using a method such as [59] to obtain static design wind loads. As in the case of mean velocity, time varying gusts depend strongly on the terrain roughness.

Modeling turbulent gusts is generally more difficult than modeling the mean velocity. In the time domain, the velocity fluctuations $\boldsymbol{u}'$ are defined by

$$\boldsymbol{u}' = \boldsymbol{u} - \bar{\boldsymbol{u}}. \tag{2.4}$$

The spectral gap [114] facilitates the definition of (2.4) where $\bar{\boldsymbol{u}}$ and $\boldsymbol{u}'$ describe the wind effects from the meso- and microscales, respectively. The latter may be filtered out by averaging the velocity over a period of approximately 10 minutes.

For the description of the turbulent fluctuations, it is useful to define the covariance tensor [112]

$$R_{ij}(\boldsymbol{x};\boldsymbol{\xi}) = \overline{u_i'(\boldsymbol{x})u_j'(\boldsymbol{x}+\boldsymbol{\xi})} \tag{2.5}$$

and its Fourier transform, the spectral tensor[1]

$$\boldsymbol{\Phi}_{ij}(\boldsymbol{x};\boldsymbol{k}) = \frac{1}{(2\pi)^3}\int_{-\infty}^{\infty}\int_{-\infty}^{\infty}\int_{-\infty}^{\infty} R_{ij}(\boldsymbol{x};\boldsymbol{\xi})\exp(-i\boldsymbol{k}\cdot\boldsymbol{\xi})d\boldsymbol{\xi}. \tag{2.6}$$

From the practical standpoint, (2.5) cannot be directly calculated since measurements are usually only available at a small number of measurement positions. Based on these measurements, several useful statistics can nevertheless be computed. These statistics are defined here to be consistent with the results presented throughout this work. They include the turbulence intensity

[1] Under the assumption of homogeneity in the x- and y-direction, the dependence of statistics on position reduces to $R_{ij}(\boldsymbol{x};\boldsymbol{\xi}) = R_{ij}(z;\boldsymbol{\xi})$ and $\boldsymbol{\Phi}_{ij}(\boldsymbol{x};\boldsymbol{k}) = \boldsymbol{\Phi}_{ij}(z;\boldsymbol{k})$.

$$T.I. = \frac{\sigma_u}{\bar{u}}, \tag{2.7}$$

with $\sigma_u^2 = \overline{u'u'}$, the one-sided power or energy spectrum

$$S_i(f) = 2 \int_{-\infty}^{\infty} \overline{u_i'(t_0) u_i'(t_0 + t)} \exp(-2\pi i f t) dt \tag{2.8}$$

and the autocorrelation

$$\rho_u(t) = \frac{\overline{u'(t_0) u'(t_0 + t)}}{\sigma_u^2}, \tag{2.9}$$

which are understood to also depend on the height above the ground.

Here we recall that $\rho_u(t) = \rho_u(-t)$ and thus $S_i(f)$ is a real-valued, even function and $\sigma_u^2 = \int_0^\infty S_u(f) df$. These statistics, which are based on time series at a fixed point, are converted to a form based on distance using Taylor's frozen turbulence hypothesis [109], i.e. by setting $(\xi_x, 0, 0) = (\bar{u}t, 0, 0)$, and vice versa in order to relate the point statistics to statistics based on (2.5) and (2.6).

The discrete counterparts to the above statistics are included in appendix A.

2.3 Synthetic Wind Generator

2.3.1 Generation of Time-Varying Wind

The challenge for the time-resolved simulation of wind is to generate a physically realistic field of velocity fluctuations from a limited set of statistics such as mean velocity (2.1), turbulence intensity (2.7) and spectrum (2.8). This transformation is depicted in figure 2.1.

A range of techniques exists for performing this transformation (see, e.g., [106] and the references therein), all of which involve a set of parameters that must be adjusted to fit the data. One of the most obvious techniques mimics the approach used in wind tunnels. Roughness elements are distributed over the ground and a large-eddy simulation is performed. The initial size and distribution of roughness elements may be estimated

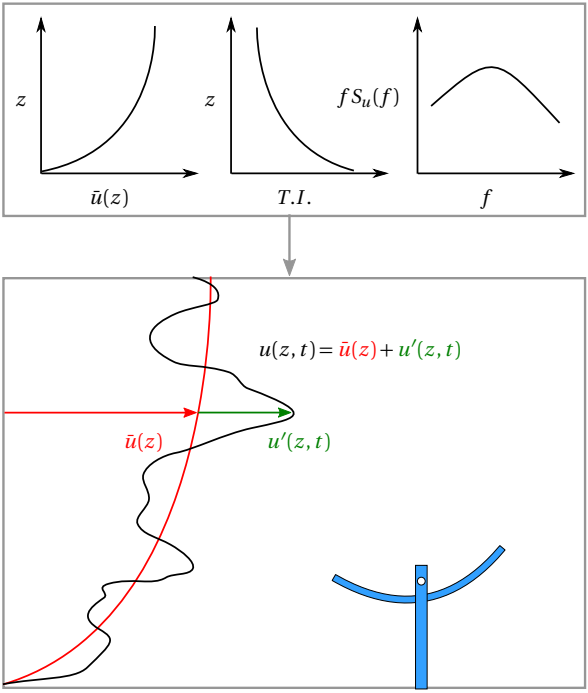

Figure 2.1: Transformation from a statistical description of wind to time-varying inflow conditions (adapted from [3]).

with the aid of the empirical formula of [67]. The numerical statistics are then evaluated and compared with the reference data. If the results do not match, the size and distribution of the roughness elements is adjusted and the procedure is repeated. Such techniques may be applied to a periodic domain to reduce the problem size. The domain size must however still be large enough to capture the range of turbulent length scales existing in the surface layer. The velocities are extracted and applied in a subsequent simulation as an inlet boundary condition. Such methods are referred to as precursor simulations [106].

The alternative to precursor simulation is synthetic generation. Synthesis techniques are based on simplified models with varying degrees of physical modeling. Their primary advantage over precursor simula-

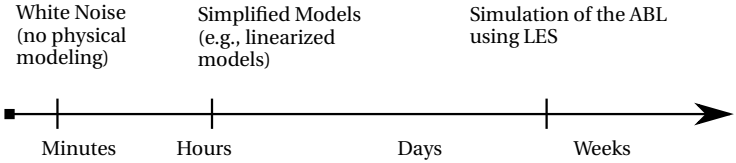

Figure 2.2: Wind modeling approaches versus computational cost [3].

tion is their lower computational cost, which is typically several orders of magnitude lower (figure 2.2). When choosing a synthesis method, it is important to consider the assumptions behind the model and whether these are sufficient to capture the relevant physics of the problem for the quantities being investigated. Reviews of some synthesis techniques for wind field simulation are provided by [49, 72, 90]. Important properties for such methods include the fulfillment of the divergence free condition, the ability to model anisotropic spectra and control over the turbulence length scale. The discretizing and synthesizing random flow generation (DSRFG) method, proposed by [49] satisfies these criteria. However, the model is unlikely to reproduce additional physical properties, which are not explicitly accounted for, since it is not derived from physical principles. It is shown by [1] that the DSRFG method fails to reproduce the dependency of coherence on frequency. The same authors propose and extension of the method, called the consistent DSRFG (CDSRFG) method, to correct this deficiency by introducing additional tuning parameters and empirical models. An alternative method satisfying the same criteria is developed by [71]. This method is derived from physical principles and has been used by [72] for LES of a large-span umbrella. It is chosen in this work for its ability to reproduce physical properties, including spectra and coherence, to a close approximation using a small number of tuning parameters. A brief review of the J. Mann model in [71] and its implementation in this work is provided in the remainder of this section to highlight some of the modeling assumptions.

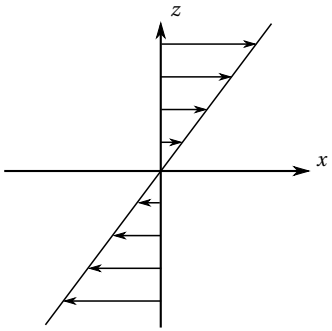

Figure 2.3: Uniform shear profile [70].

2.3.2 Linearized Model of Turbulent Shear Flow

The difficulty associated with solving the Navier-Stokes equations is rooted in their nonlinearity. This problem can be simplified to some extent by introducing certain assumptions about the nature of the turbulence. Under the assumption of homogeneous turbulence, the gradient of the mean velocity $\nabla \bar{\boldsymbol{u}}$ and the Reynolds stresses $\rho \overline{u_i' u_j'}$ are constant in space. For uniform ABL flow over flat terrain, the only nonzero component of $\nabla \bar{\boldsymbol{u}}$ is $\frac{\partial \bar{u}}{\partial z}$ and, assuming $\frac{\partial \bar{u}}{\partial z}$ to be constant, $\bar{u} = z \frac{\partial \bar{u}}{\partial z}$ as depicted by the uniform shear profile in figure 2.3.

Based on these assumptions, a set of equations can be obtained that describe the shearing effect of the mean velocity field on the turbulent fluctuations. Neglecting the nonlinear interaction of the velocity fluctuations and viscous effects leads to a set of linear ordinary differential equations based on the wave number in Fourier space, which are referred to as the rapid distortion equations. The reader is referred to [112] for a detailed overview.

The assumption of a constant gradient of mean velocity is a clear contradiction to the mean profile in (2.1). Nevertheless, the results show that it leads to a model of turbulent eddies capable of reproducing several of the characteristics observed in natural wind to a good approximation.

By solving the rapid distortion equations, [70] presents an explicit model of the spectral tensor as $\boldsymbol{\Phi}(\beta_{LT})$ with $\beta_{LT} = t \frac{\partial \bar{u}}{\partial z}$ a dimensionless eddy lifetime. For $\beta_{LT} = 0$, the spectral tensor corresponds to isotropic

turbulence with the von Kármán energy spectrum [58]

$$E(k) = E_0 L_{iso}^{5/3} \frac{(L_{iso}k)^4}{(1+(L_{iso}k)^2)^{17/6}}. \tag{2.10}$$

The length scale L_{iso} and coefficient E_0 are model parameters, which control the initial turbulence length scale and turbulence intensity.

The initially isotropic turbulence is distorted by the rapid distortion equations as β_{LT} increases. A consequence of the linearized model is that the eddies remain stable as they deform. To simulate real turbulent flow, an eddy lifetime model is assumed. In [70], the lifetime model

$$\beta_{LT}(k) = \Gamma_{LT}(L_{iso}k)^{-2/3} \left[\ {}_2F_1\left(\frac{1}{3}, \frac{17}{6}; \frac{4}{3}; -\frac{1}{(L_{iso}k)^2}\right)\right]^{-1/2} \tag{2.11}$$

is proposed, based on the wave number k and a characteristic velocity determined from the integral of (2.10) over wave numbers smaller than k. ${}_2F_1$ is the hypergeometric function and Γ_{LT} is a model parameter, which controls the anisotropy or stretching of the turbulent eddies. The spectral tensor model is evaluated at $\beta_{LT}(k)$ in order to freeze the stretching of the eddies.

The velocity fluctuations are generated in a periodic domain on a Cartesian grid consisting of $N_1 \times N_2 \times N_3$ grid points with grid spacing $\Delta x_i = L_i/N_i$. This is done by computing the inverse of the discrete Fourier transformation (DFT)

$$\boldsymbol{u}'(\boldsymbol{x}) = \sum_{\boldsymbol{k}} \hat{\boldsymbol{u}}'(\boldsymbol{k}) \exp(i\boldsymbol{k}\cdot\boldsymbol{x})\, \Delta\boldsymbol{k} \tag{2.12}$$

with

$$\hat{\boldsymbol{u}}'(\boldsymbol{k}) = \frac{\sqrt{L_1 L_2 L_3}}{(2\pi)^{3/2}} \boldsymbol{C}(\boldsymbol{k})\boldsymbol{n}(\boldsymbol{k}). \tag{2.13}$$

By letting $\boldsymbol{n}(\boldsymbol{k})$ be independent Gaussian complex random vectors of unit variance, the 3×3 matrix $\boldsymbol{C}(\boldsymbol{k})$ is related to the spectral tensor by [71]

$$\begin{aligned} C_{il}^*(\boldsymbol{k})C_{jl}(\boldsymbol{k}) &= \overline{\hat{u}_i'^*(\boldsymbol{k})\hat{u}_j'(\boldsymbol{k})} \\ &= \int_{-\infty}^{\infty}\int_{-\infty}^{\infty}\int_{-\infty}^{\infty} \Phi_{ij}(\boldsymbol{s}) \prod_{l=1}^{3} \operatorname{sinc}^2\left(\frac{(k_l - s_l)L_l}{2}\right) d\boldsymbol{s}. \end{aligned} \tag{2.14}$$

For the s_1 component or for wave numbers $k > 3/L_{iso}$, the spectral tensor is nearly constant over the first zero and the sinc function is approximated by a weighted delta distribution [71]. Otherwise, the convolution integral is carried out numerically (using the midpoint rule) over a domain restricted to the first zero of the sinc function ($|k_l - s_l|L_l/2 < \pi$) for components s_2 and s_3. Spectral decomposition is used to factorize the right hand side of (2.14) with the eigenvalues calculated explicitly by the formulas in [99]. Finally, since the velocity fluctuations are real numbers, Hermitian symmetry of the Fourier components $\hat{u}_i'(\boldsymbol{k}) = \hat{u}_i'^*(-\boldsymbol{k})$ is enforced.

The complete model has three adjustable parameters (Γ_{LT}, L_{iso}, E_0), which control the statistical properties of the synthesized turbulence, including anisotropy or stretching of the eddies, a length scale of the initial isotropic turbulence and the turbulence intensity. These parameters are chosen in an optimal way, for example, by minimization of the nonlinear least-squares problem, to fit experimental data. The current work uses the Kaimal spectra given by [56]:

$$\frac{fS_u(f)}{u_*^2} = \frac{105fz/\bar{u}}{(1+33fz/\bar{u})^{5/3}}, \tag{2.15}$$

$$\frac{fS_v(f)}{u_*^2} = \frac{17fz/\bar{u}}{(1+9.5fz/\bar{u})^{5/3}}, \tag{2.16}$$

$$\frac{fS_w(f)}{u_*^2} = \frac{2fz/\bar{u}}{1+5.3(fz/\bar{u})^{5/3}}. \tag{2.17}$$

The corresponding model parameters are provided in table 2.1.

L_{iso}	E_0	Γ_{LT}
$0.59z$	$3.2u_*^2/z^{2/3}$	3.9

Table 2.1: Kaimal model parameters [71].

To illustrate the approximation quality, longitudinal spectra of the uniform shear model are compared with the reference spectra in figure 2.4.

The spatially varying turbulent fluctuations are transformed to temporally varying inlet data using Taylor's frozen turbulence hypothesis [109]. The time-dependent inlet velocities are computed on the yz-plane slicing

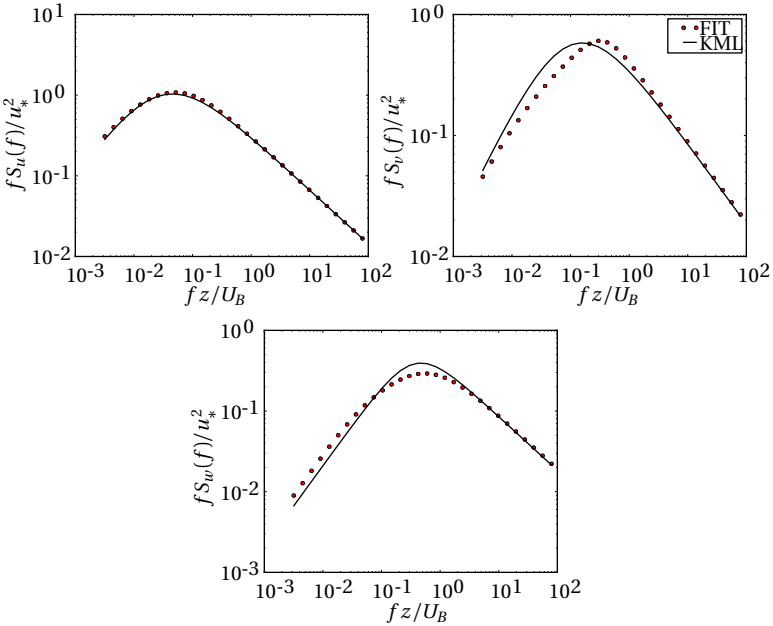

Figure 2.4: Model spectra fitted to Kaimal spectra from [56].

through the frozen wind field at the x-coordinate $x(t) = x_0 - U_B t$ with x_0 an arbitrary starting position and U_B taken as the average of (2.1) over the domain height. Choosing U_B to be constant satisfies the assumption of homogeneity and preserves the structure and divergence free condition of the fluctuations. However, eddies with characteristic size D before the inlet are stretched or compressed in the streamwise direction to $\bar{u}(z)/U_B D$ after the inlet as depicted in figure 2.5.

2.3.3 Library Implementation

In this work the wind simulation model is implemented in the C library [4] with support for distributed memory parallelism using MPI. The inverse DFT in equation (2.12) is computed by the FFTW3 library in [39] with complexity $\mathcal{O}(N \log N)$. As a consequence of this transformation, the entire wind field must be generated before the inlet data can be used. This

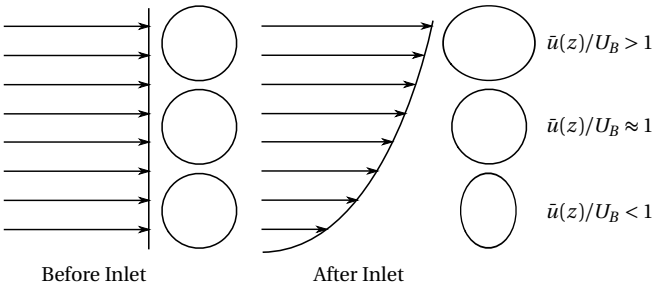

Figure 2.5: Characteristic eddy sizes before and after the inlet [3].

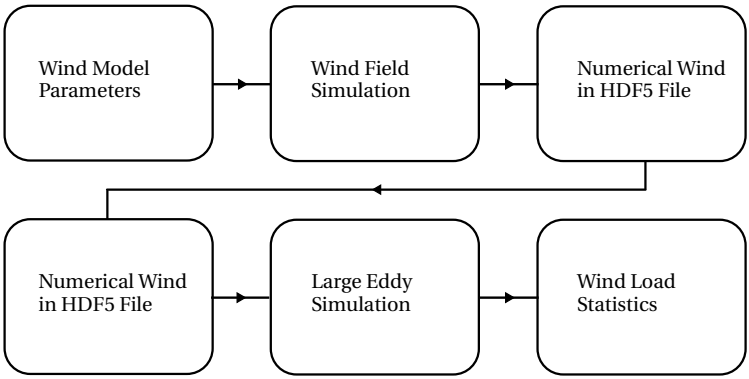

Figure 2.6: Workflow for simulating wind loads [3].

typically results in large data sets. A small subset of data is read by the flow solver at each time step and assigned as time-varying velocities on the inlet boundary. The wind field is stored efficiently in the self-describing, portable HDF5 format. The HDF5 library [111] supports shared file access and collective reading and writing across MPI processes and provides the necessary functionality for accessing metadata and data subsets, thus greatly reducing the programming overhead required to add the wind inlet boundary condition to existing flow solvers. In addition to the file format and API, tools such as HDFView [111] and h5py [25] are available for view-

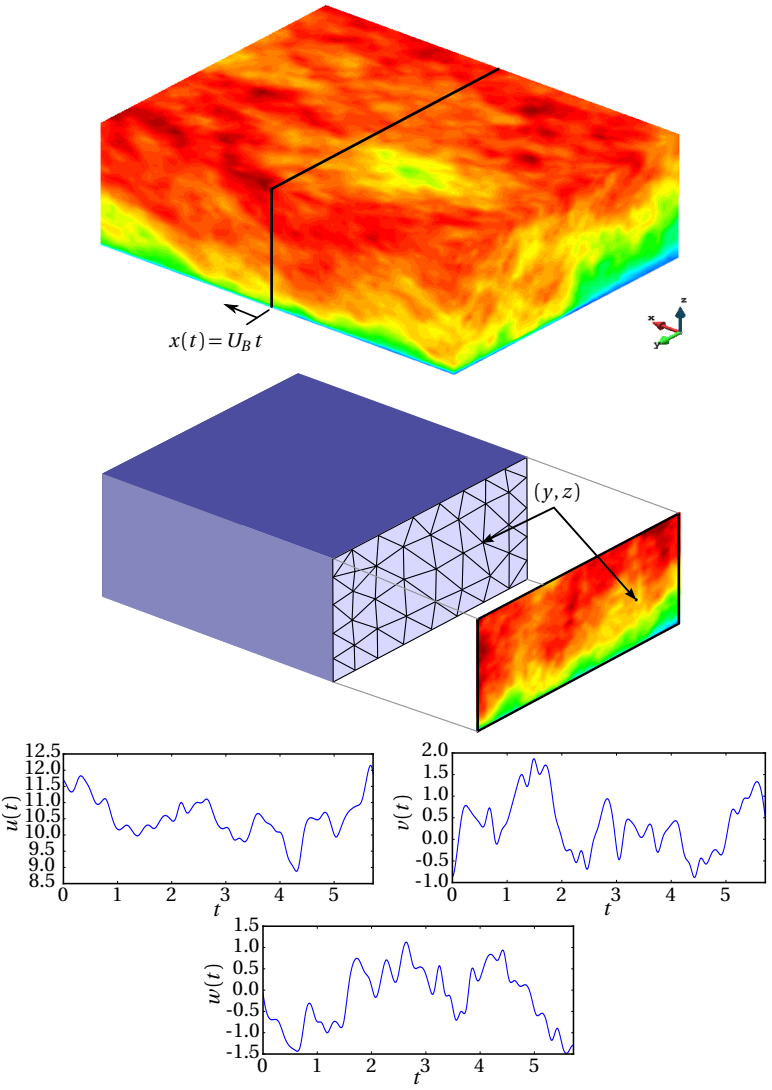

Figure 2.7: Transformation from a frozen wind field to time-varying inlet boundary conditions on an LES domain [3].

ing and manipulating HDF5 formatted files. The complete workflow for simulating wind loads using the current modeling approach is shown in figure 2.6. The transformation from the frozen wind field generated by the uniform shear model to a time-varying inlet boundary condition on an discretized LES domain is depicted in figure 2.7.

Chapter 3

Large-Eddy Simulation

3.1 Finite Element Formulation

The finite element implementation developed in the work of [27] within the open source software Kratos [28] is used for the simulations presented in this work. A brief review of the finite element formulation and some of its properties is given in this section.

The incompressible Navier-Stokes equations are discretized using simplicial Lagrange finite elements with linear shape functions for both velocity and pressure. Formally, the finite element spaces are given by[1]

$$\tilde{V}_h = \{\boldsymbol{v}_h \in [\mathcal{C}^0(\overline{\Omega}_h)]^d \ : \ \boldsymbol{v}_h|_K \in [\mathbb{P}_1]^d, \ \forall K \in \mathcal{T}_h\} \tag{3.1}$$

and

$$\tilde{Q}_h = \{q_h \in \mathcal{C}^0(\overline{\Omega}_h) \ : \ q_h|_K \in \mathbb{P}_1, \ \forall K \in \mathcal{T}_h\} \tag{3.2}$$

where $\mathcal{T}_h$ is the mesh of simplices (triangles in 2D or tetrahedra in 3D). It is well known that this choice of finite element spaces leads to spurious

[1] The notation used here closely follows that of [36].

pressure modes in the Stokes problem due to the violation of the Babuška-Brezzi condition (see, e.g., §4.2, [36]). Some pressure stability based on the time step size is recovered by applying the fractional-step method [22]. However, this is not sufficient for second-order schemes. An additional problem arising from the standard Galerkin method is the loss of coercivity in the advection-diffusion problem with increasing Péclet number (see, e.g., §3.5, [36]).

The fractional-step solver in Kratos overcomes both of these issues by using quasi-static orthogonal subgrid-scale stabilization (OSS) as introduced in [23] and discussed by [27]. Denoting the part of the boundary where the velocity has the prescribed value $\boldsymbol{u}_D$ by Γ_D[2], we define the finite element subspaces

$$W_h = \{\boldsymbol{w}_h \in \tilde{V}_h \,:\, \boldsymbol{w}_h|_{\Gamma_D} = \boldsymbol{u}_D\}, \tag{3.3}$$

$$V_h = \{\boldsymbol{v}_h \in \tilde{V}_h \,:\, \boldsymbol{v}_h|_{\Gamma_D} = \boldsymbol{0}\}, \tag{3.4}$$

and

$$Q_h = \{q_h \in \tilde{Q}_h \,:\, q_h|_{\partial\Omega_h - \Gamma_D} = 0\}. \tag{3.5}$$

For consistency with chapters 5 and 6, the mesh velocity $\delta_t \boldsymbol{\psi}_h$ is also included here. Both here and in chapter 4, its value is understood to be zero. At each time step, the solution variables are initialized by the their values at the previous time step. For example, velocity and pressure are initialized by $\boldsymbol{u}_h^{n,0} = \boldsymbol{u}_h^{n-1}$ and $p_h^{n,0} = p_h^{n-1}$. A sequence of pressure iterations, denoted by the superscript m, are then performed by solving the fractional-step problem shown below. For simplicity, we drop the superscript denoting the current time step and simply write $\boldsymbol{u}_h^{n,m} = \boldsymbol{u}_h^m$ and $p_h^{n,m} = p_h^m$ for velocity and pressure with similar notation for the subscale projections $\boldsymbol{\pi}_{hc}$, $\boldsymbol{\pi}_{hp}$ and π_{hd}. For the time discretization, the second-order BDF2 scheme is used.

[2] Here $\boldsymbol{u}_D$ and Γ_D are assumed to conform to the finite element discretization.

Fractional-Step Solver: m^{th} pressure iteration.

Given $\boldsymbol{u}_h^{m-1}, \boldsymbol{u}_h^{n-1}, \boldsymbol{u}_h^{n-2}, \delta_t \boldsymbol{\psi}_h^m, \boldsymbol{\pi}_{hc}^{m-1}, \boldsymbol{\pi}_{hp}^{m-1}, p_h^{m-1}, \pi_{hd}^{m-1}$:

1. Seek $\tilde{\boldsymbol{u}}_h^m \in W_h$ such that:

$$\begin{aligned}
&\int_{\Omega_h} \boldsymbol{v}_h \cdot \rho \delta_t \tilde{\boldsymbol{u}}_h^m d\Omega_h + \int_{\Omega_h} \boldsymbol{v}_h \cdot \rho(\tilde{\boldsymbol{u}}_h^m - \delta_t \boldsymbol{\psi}_h^m) \cdot \nabla \tilde{\boldsymbol{u}}_h^m d\Omega_h \\
&+ \int_{\Omega_h} 2\mu \left[\boldsymbol{\epsilon}(\boldsymbol{v}_h) : \boldsymbol{\epsilon}(\tilde{\boldsymbol{u}}_h^m) - \frac{1}{3}(\nabla \cdot \boldsymbol{v}_h)(\nabla \cdot \tilde{\boldsymbol{u}}_h^m) \right] d\Omega_h \\
&+ \sum_{K \in \mathcal{T}_h} \int_K \rho(\tilde{\boldsymbol{u}}_h^m - \delta_t \boldsymbol{\psi}_h^m) \cdot \nabla \boldsymbol{v}_h \cdot \tau_1 \rho(\tilde{\boldsymbol{u}}_h^m - \delta_t \boldsymbol{\psi}_h^m) \cdot \nabla \tilde{\boldsymbol{u}}_h^m dK \\
&+ \sum_{K \in \mathcal{T}_h} \int_K (\nabla \cdot \boldsymbol{v}_h) \tau_2 (\nabla \cdot \tilde{\boldsymbol{u}}_h^m) dK \\
&= \int_{\Omega_h} (\nabla \cdot \boldsymbol{v}_h) p_h^{m-1} d\Omega_h + \int_{\Omega_h} \boldsymbol{v}_h \cdot \rho \boldsymbol{f}_B d\Omega_h \\
&+ \sum_{K \in \mathcal{T}_h} \int_K \rho(\tilde{\boldsymbol{u}}_h^m - \delta_t \boldsymbol{\psi}_h^m) \cdot \nabla \boldsymbol{v}_h \cdot \tau_1 \boldsymbol{\pi}_{hc}^{m-1} dK \\
&+ \sum_{K \in \mathcal{T}_h} \int_K (\nabla \cdot \boldsymbol{v}_h) \tau_2 \pi_{hd}^{m-1} dK, \qquad \forall \boldsymbol{v}_h \in V_h. \qquad (3.6)
\end{aligned}$$

2. Seek $p_h^m \in Q_h$ such that:

$$\begin{aligned}
&-\int_{\Omega_h} \frac{2\Delta t}{3\rho} \nabla q_h \cdot \nabla (p_h^m - p_h^{m-1}) d\Omega_h \\
&- \sum_{K \in \mathcal{T}_h} \int_K \tau_1 \nabla q_h \cdot \nabla p_h^m dK = \int_{\Omega_h} q_h \left(\nabla \cdot \tilde{\boldsymbol{u}}_h^m \right) d\Omega_h \\
&- \sum_{K \in \mathcal{T}_h} \int_K \nabla q_h \cdot \tau_1 (\rho \boldsymbol{f}_B + \boldsymbol{\pi}_{hp}^{m-1}) dK, \qquad \forall q_h \in Q_h. \qquad (3.7)
\end{aligned}$$

Fractional-Step Solver: m^{th} pressure iteration (continued).

3. Seek $\boldsymbol{u}_h^m \in W_h$ such that:

$$\int_{\Omega_h} \boldsymbol{v}_h \cdot (\boldsymbol{u}_h^m - \tilde{\boldsymbol{u}}_h^m) d\Omega_h$$
$$= \frac{2\Delta t}{3\rho} \int_{\Omega_h} (\nabla \cdot \boldsymbol{v}_h)(p_h^m - p_h^{m-1}) d\Omega_h, \qquad \forall \boldsymbol{v}_h \in V_h. \tag{3.8}$$

4. Seek $\boldsymbol{\pi}_{hc}^m, \boldsymbol{\pi}_{hp}^m \in \tilde{V}_h, \pi_{hd}^m \in \tilde{Q}_h$ such that:

$$\int_{\Omega_h} \boldsymbol{v}_h \cdot \boldsymbol{\pi}_{hc}^m d\Omega_h = \int_{\Omega_h} \boldsymbol{v}_h \cdot \rho(\tilde{\boldsymbol{u}}_h^m - \delta_t \boldsymbol{\psi}_h^m) \cdot \nabla \tilde{\boldsymbol{u}}_h^m d\Omega_h, \ \forall \boldsymbol{v}_h \in \tilde{V}_h, \tag{3.9}$$

$$\int_{\Omega_h} \boldsymbol{v}_h \cdot \boldsymbol{\pi}_{hp}^m d\Omega_h = \int_{\Omega_h} \boldsymbol{v}_h \cdot (\nabla p_h^m - \rho \boldsymbol{f}_B) d\Omega_h, \qquad \forall \boldsymbol{v}_h \in \tilde{V}_h, \tag{3.10}$$

$$\int_{\Omega_h} q_h \pi_{hd}^m d\Omega_h = \int_{\Omega_h} q_h \nabla \cdot \tilde{\boldsymbol{u}}_h^m d\Omega_h, \qquad \forall q_h \in \tilde{Q}_h. \tag{3.11}$$

The stabilization parameters are defined as

$$\tau_1 = \left[\rho \left(\frac{\tau_{dyn}}{\Delta t} + 4\frac{\nu}{h_K^2} + 2\frac{|\tilde{\boldsymbol{u}}_h^m - \delta_t \boldsymbol{\psi}_h^m|}{h_K} \right) \right]^{-1} \tag{3.12}$$

and

$$\tau_2 = \rho \left(\nu + \frac{1}{2} h_K |\tilde{\boldsymbol{u}}_h^m - \delta_t \boldsymbol{\psi}_h^m| \right). \tag{3.13}$$

Moreover, the element integrals on the left-hand sides of (3.8)-(3.11) are computed with the quadrature points on the nodes, resulting in lumped mass matrices.

In the case of a deforming domain, all integrals in the above algorithm are computed at the current time step. According to [37], this ensures geometric conservation in the sense that it preserves a constant velocity field.

In addition to providing stabilization, variational multiscale methods (VMMs), including the OSS method described above, can also be applied as implicit LES models for turbulent flows [26, 40, 83]. This idea follows from their interpretation as a model for the unresolved component of the continuous velocity and pressure fields as originally presented by [51]. The interested reader is referred to [27] for a detailed analysis of the turbulence modeling properties of the subgrid-scale models in Kratos.

3.2 Near Wall Model

LES uses simplified subgrid scale models for the small scales, which are assumed to have a universal structure. Although the required resolution of the interior domain is typically a fixed fraction of the geometric scale, the number of degrees of freedom required in the near wall region increases approximately with the square of the Reynolds number [10, 19].

One approach to alleviate the resolution requirements in the wall layer is to use a hybrid RANS/LES model or detached eddy simulation (DES) [102]. The approach uses a RANS model for the wall layer while LES is used to model the flow in the interior of the domain. A review of DES and its formulations can be found in [100]. Meshing requirements are discussed by [101]. DES requires anisotropic grid refinement to within the viscous sublayer in the wall normal direction. This significantly increases the meshing difficulty compared to isotropic mesh generation for complex geometries and may lead to problems with shape-regularity as well as robustness under mesh deformation when simulating FSI. Moreover, the study of [62] showed that when DES is applied on coarse grids with high Reynolds numbers, the LES zone may behave similar to a RANS zone, resulting in poor accuracy compared to LES models with a wall function. For these reasons, DES is not considered further in this work.

Another possibility consists of using simplified boundary layer theory in the near wall region. In this approach, a boundary layer grid with refinement in the wall normal direction is embedded in the LES mesh between the wall and the first LES grid point. The pressure and velocity of the first LES grid point are applied as upper boundary conditions and a no-slip condition is applied at the wall. This approach, introduced in [12], is referred to as a two-layer model and has been used successfully for predicting channel flow, favourable and adverse pressure gradients [117]

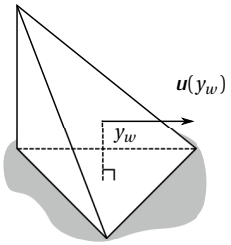

Figure 3.1: Wall function parameters in a tetrahedron element.

and separated flows [17]. Due to the complexity of creating a second mesh of the wall layer and coupling with the initial mesh, this approach is not considered further here.

Wall stress models using equilibrium laws such as the log-law provide the simplest solution to the near wall problem. A one-dimensional problem is solved based on the values of the flow variables and possibly their gradients at a point with a distance y_w from the wall in order to compute the wall stress. The wall stress is then applied as a boundary condition in the wall tangent direction. The one-dimensional problem eliminates the meshing problem associated with the more sophisticated models described earlier. On the other hand, the reduction in dimensionality leads to essential simplifications of the physical models, which are often based on channel flow, and modeling errors may be expected for more complex problems such as flows with separation [17, 76]. Even relatively simple problems such as flow through a square duct can result in significant variation of the empirical constants [43].

In this work, the one-dimensional wall function model is used in combination with tetrahedral finite elements as shown in figure 3.1. The integral of the wall stress is calculated over the element face using a one point quadrature. The choice of y_w is not constrained by the wall stress model. The classical approach for applying wall functions in the finite volume method uses the flow values at the first off the wall grid point. In [60], it is argued that this approach leads to under-resolved flow information being supplied to the wall stress model which adds to the modeling errors. It is proposed to instead use better resolved flow information from interior grid points. In order to restrict the implementation to the local element

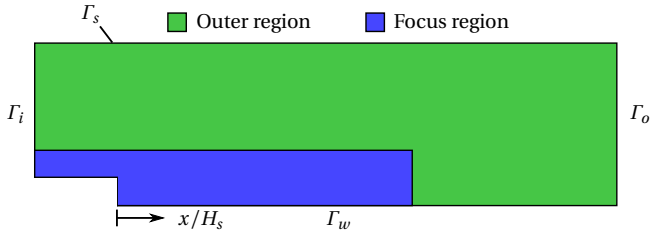

Figure 3.2: Backward-facing step domain and mesh regions.

level, the choice of y_w is taken to be the intersection point of the boundary face normal director with the interior face as illustrated in figure 3.1. This choice maximizes the weight given to the interior node which is assumed to have better resolution properties than the wall nodes. The velocity used by the wall stress model is computed as the projection of the instantaneous velocity onto the plane defined by the boundary face. The model can be combined with any one-dimensional wall model. In this work it has been combined with the models of [118] and [98].

3.3 Backward-Facing Step

The backward-facing step problem is simulated as an initial test case for the flow solver used in this work. The results are compared with the experiment of [54], which was conducted at NASA Ames Research Center at a Reynolds number of Re=5000 based on the step size.

In the experiment, an initial channel of width 30.5 cm and height 9.6 cm is suddenly expanded by a step of height 0.98 cm. The turbulence intensity upstream of the step is below 1%, allowing a steady inlet boundary condition to be used in the numerical simulation. The experimental data includes skin friction, mean velocity profiles and Reynolds stress profiles downstream of the step. The measurements are estimated to be within ±2% for the mean velocity and ±15% for the Reynolds stresses. The reattachment is estimated to occur at $x/H_s = 6 \pm 0.15$.

The simulation domain and mesh parameters are shown in figure 3.2 and table 3.1, respectively. The mean velocity profile on the inlet boundary Γ_i at $x/H_s = -3.12$ is prescribed by the experimental measurement data at the same position. A slip condition is prescribed on the upper boundary

Mesh	Mesh Size (H_s/h)		$\frac{y_w u_*}{\nu}$	N_{el}
	Focus	Outer		
Coarse	6.5	2.6	30	694293
Fine	9.8	2.6	20	1907304

Table 3.1: Backward-facing step mesh settings.

Γ_s, a zero pressure outlet condition is applied on the outlet Γ_o, and the wall function in [98] is applied on the bottom boundary Γ_w. The domain dimension perpendicular to the plane is $6H_s$, and a periodic boundary is used.

The simulation results are shown in figure 3.3. For both meshes, the mean velocity behind the step is in close agreement with the experiment. Larger differences are observed for the Reynolds stress or RMS velocity fluctuations. On the experimental side, the measurement uncertainty is larger for the RMS velocity fluctuations than for the mean velocity. Additionally, the numerical results are more sensitive to the difference in mesh size. The appearance of larger uncertainties in RMS results compared to mean results is observed consistently throughout this work.

The skin friction appears to be well approximated by the fine mesh but fails to predict the profile in the recirculation region on the coarser mesh. Thus, if the quantity of interest depends on the accurate prediction of skin friction, high near wall resolution may still be necessary when using the current modeling approach.

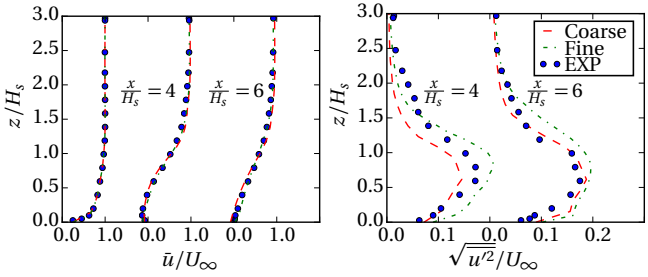

(a) Mean velocity

(b) RMS velocity fluctuations

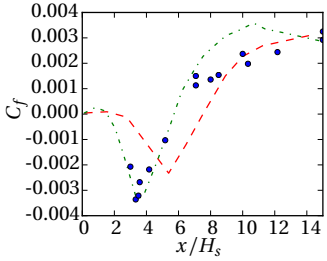

(c) Friction coefficient

Figure 3.3: Comparison of backward-facing step simulation results with experimental results from [54].

Chapter 4

Boundary Layer Wind Tunnel Validation

When validating numerical models of ABL flows, one must either compare with field measurements or with experimental data obtained from a BLWT. Field measurement data for PTSCs is quite limited. At the time of this writing, the only known available study is by [44]. Further, variability in wind conditions during field measurements may introduce additional uncertainty in the data. This can result in larger differences between measured data and numerical results than would otherwise be observed if the wind conditions could be more precisely determined. Alternatively, BLWT experiments offer an environment in which conditions such as roughness, wind direction and wind speed can be more carefully controlled, enabling a more precise comparison of physical measurement with numerical simulation. For these reasons, the conditions measured in a BLWT experiment are simulated using the numerical approach presented in this work and the estimated wind loads are compared.

Still, uncertainties in the simulated wind conditions cannot be completely eliminated since often only a limited set of point data is available. The ability of numerical models to reproduce the conditions of a wind

tunnel experiment is ultimately limited by the amount and quality of information from the wind tunnel. This presents a significant challenge for the field of CWE, which is not yet established as a reliable alternative to wind tunnel experiments. Presently, wind tunnel experiments are still considered to be more reliable for the assessment of wind loads on solar collectors [105].

The primary aim of this chapter is to investigate the ability of the proposed numerical model to simulate wind loads on a PTSC in an ABL flow. The broader aim is to contribute a high quality comparison of numerical simulation with physical experiment for the estimation of structural wind loads to the field of CWE. The need for such studies has recently been emphasized by [14]. Part of the work presented in this chapter has been published in [7] where the FEM results were further compared with results from the lattice Boltzmann method. It is included here with permission from the publisher.

In section 4.1, the wind tunnel experiment used in this work is described. The computational domain, boundary conditions and discretization parameters are described in section 4.2. The turbulent conditions in the simulated ABL are calibrated from experimental data in section 4.3. Wind loads are then simulated at wind tunnel scale on three different meshes in section 4.4 and compared with measurement data.

4.1 Experimental Setup

The experimental model consists of a 1:25 scale isolated collector module with the dimensions shown in figure 4.1. Mean, RMS, maximum and minimum values of drag F_x, lift F_z and base moment M_b are determined for the 9 pitch angles depicted in figure 4.2 for the case of uniform upstream roughness. At full scale, the roughness is $z_0 = 0.02\,\mathrm{m}$ and corresponds to open country terrain [119]. In all cases, the wind direction is perpendicular to the pitch axis. Based on the study of [47], this is expected to result in the largest aerodynamic wind loads.

The wind tunnel experiment was carried out at the Boundary Layer Wind Tunnel Laboratory at Western University, Canada, and reported by [110]. The Reynolds number was $\mathrm{Re} = 85000$ and is defined as

$$\mathrm{Re} = \frac{U_{ref} W}{\nu}. \tag{4.1}$$

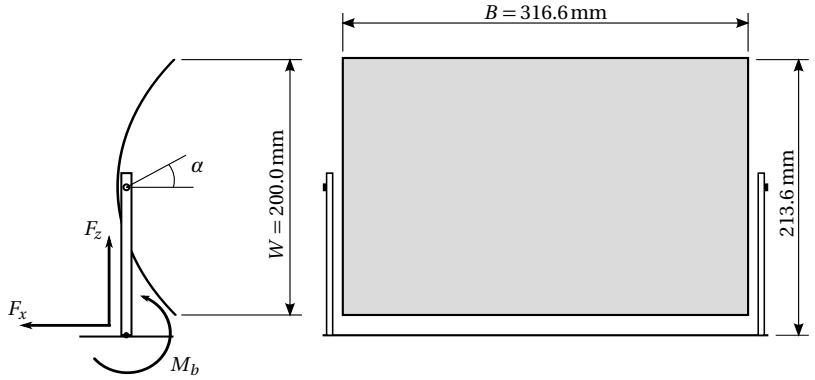

Figure 4.1: Model geometry with force and moment definitions [110].

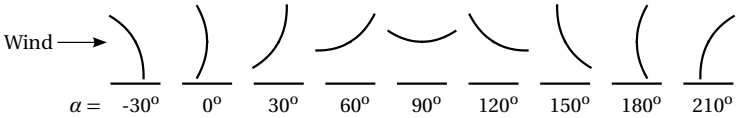

Figure 4.2: Pitch angle configurations [74].

Here U_{ref} is the mean reference velocity measured at a reference height of $z_{ref} = 0.4\,\text{m}$, $W = 0.2\,\text{m}$ is the aperture of the collector and $\nu = 1.5 \times 10^{-5}\,\text{m}^2/\text{s}$ is the kinematic viscosity of air. Time series of forces and moment were measured using a JR3 multi-axis force-torque sensor [55]. The uncertainty range of the sensor is given as ±0.25% of the standard measuring range for the drag, lift and pitching moment, respectively, and is constant over all pitch angle configurations.

The force and moment measurements are transformed into aerodynamic load coefficients defined according to

$$C_D = \frac{F_x}{0.5\rho U_{ref}^2 BW}, \tag{4.2}$$

$$C_L = \frac{F_z}{0.5\rho U_{ref}^2 BW}, \tag{4.3}$$

$$C_{M_b} = \frac{M_b}{0.5\rho U_{ref}^2 BW^2}. \tag{4.4}$$

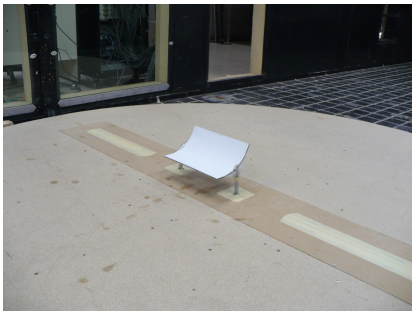

Figure 4.3: BLWT model [110].

In addition to the force and moment statistics, mean velocity and turbulence intensity profiles were provided along with a time series of the modulus of velocity at the reference height. Statistics are computed from time series with a total time of approximately $W/U_{ref} \times 10^4$.

The BLWT experiment is shown in figure 4.3. As requested by Abengoa[1], aerodynamic load coefficients presented in this chapter are normalized by the maximum experimental value.

4.2 Computational Setup

The parameters of the numerical model are chosen to approximate the BLWT experiment as accurately as possible for the given information. The simulations are performed at the wind tunnel scale and Reynolds number. The cross section of the LES domain is identical to that of the wind tunnel with dimensions 3.5 m wide × 2.6 m high. The length in the streamwise direction is truncated to 4.1 m with the collector located 1.4 m from the inlet.

In the present study, the limitations of wind tunnel size restrict the Reynolds number. This is not a major concern since it is generally accepted that variations in Reynolds number above 10^4 do not significantly influence aerodynamic wind loads of parabolic troughs [47, 86]. For more complicated problems such as modeling the effects of ridges and escarpments, it becomes more difficult to restrict the blockage ratio to acceptable

[1] The experimental data used in this chapter is provided by Abengoa.

levels. In such cases, a numerical approach is less restrictive. Relatively large domain sizes can be efficiently modeled on unstructured meshes to effectively reduce blockage ratios. An alternative approach is the development of more realistic boundary conditions on the sides, top and outlet of the domain such as the boundary condition proposed in [32]. As the current investigation is restricted to uniform, flat terrain, these alternatives are not considered further here.

Time-varying velocities computed from the wind simulation technique described in section 2.3 are prescribed on the inlet of the truncated LES domain in order to model the effects from the uniform upstream roughness. On the ground and surface of the collector, the wall function technique described in section 3.2 is used with the wall function model described in [98]. The effects of ground roughness due to pressure drag were not explicitly modeled in the wall function in this study since the smooth wall function was found to accurately reproduce the mean velocity and turbulence intensity profiles in the vicinity of the collector. Nevertheless, wall roughness models may be included and could be useful in future studies where the distance from the inlet to the structure is larger. Given the maximum blockage ratio of the collector as 0.7%, the effects of the sides and top of the wind tunnel on the aerodynamic loads are expected to be negligible. To avoid the need to resolve the fine boundary layers developing on these surfaces, slip boundary conditions are applied to the top and sides of the LES domain. Finally, a zero pressure boundary condition is applied on the outlet.

The computational domain is subdivided into a focus region, extending from the inlet until approximately $80W$ downstream with a cross section of $7W$ wide $\times$ $3W$ high centered around the collector, and an outer region encompassing the remainder of the domain. Aerodynamic loads are calculated using three meshes in order to quantify the extent to which the results depend on the mesh. The primary mesh has a mesh size of $0.02W$ on the surface of the collector and transitions to approximately $0.16W$ in the focus region. The second mesh differs from the first in the focus region where the mesh size is halved to $0.08W$. This mesh is used to see the sensitivity of results to the resolution in the approach flow and wake region. The third mesh uses the same mesh size as the first in the focus region but halves the mesh size on the surface of the collector. This mesh is used to investigate the sensitivity of results to the mesh resolution next to the surface of the collector. In all three meshes, the mesh size of the outer

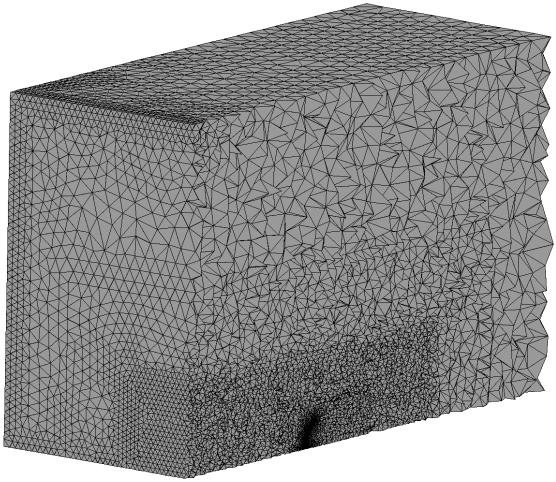

Figure 4.4: Finite element mesh 1.

region is fixed to $0.7W$. The three meshes are summarized in table 4.1.

W/h	Surface	Focus region	Outer region
Mesh 1	50	6.25	1.4
Mesh 2	50	12.5	1.4
Mesh 3	100	6.25	1.4

Table 4.1: Mesh sizes for the BLWT validation.

The first mesh is shown in figure 4.4 with a cut through the center plane. The time step size is $\Delta t = 0.003\,\mathrm{s}$ for all simulations and satisfies $U_{ref}\Delta t/h \approx 0.6$ based on the mesh size $h = 0.16W$.

4.3 Wind Simulation

4.3.1 Generation of Inlet Data

The time-varying inlet data was generated by fitting the model parameters to the conditions measured in the wind tunnel. The log roughness z_0 was chosen to minimize the difference between the measured mean velocity profile and the log mean profile in the Euclidean norm, and the height parameter z (table 2.1) was chosen based on the turbulence length scale of approximately 1 m calculated from the autocorrelation of the velocity signal measured at the reference height. The generated velocity fluctuations were calculated based on the roughness $z_0 = 0.0008\,\text{m}$ (0.02 m at full-scale) rather than the roughness obtained from fitting of the mean velocity profile because this resulted in a better approximation of the turbulence intensity profile at the position of the collector in an empty channel simulation (section 4.3.2). A summary of the wind generation parameters is given in table 4.2.

Parameter	Value
U_B	7.44 m/s
$L_x \times L_y \times L_z$	896 m × 3.5 m × 3.5 m
$N_x \times N_y \times N_z$	32768 × 128 × 128
$\Delta x \times \Delta y \times \Delta z$	0.0273 m × 0.0273 m × 0.0273 m
z	0.25 m
$\bar{u}(z)$	5.8 m/s
z_0	0.00076 m

Table 4.2: Wind simulation parameters for 1:25 scale model.

The velocity fluctuations are generated using the Kaimal spectrum [56]. Estimated spectra of the generated fluctuations for each velocity component are plotted in figure 4.5.

4.3.2 Empty Channel Simulation

The purpose of the empty channel simulation is to verify the statistics of the simulated ABL in the LES domain. The statistics are presented here for

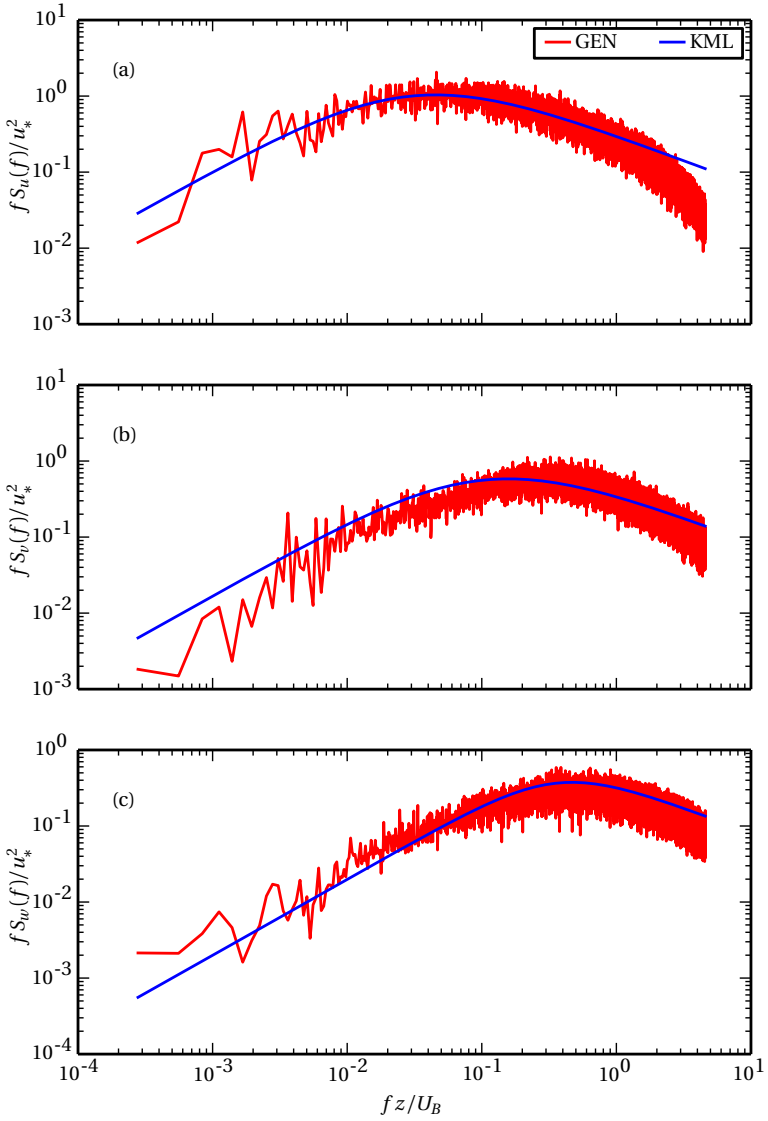

Figure 4.5: Spectra of generated wind (GEN) and Kaimal spectra (KML) for simulation of BLWT experiment.

mesh 1 of table 4.1.

The spectrum of the velocity signal measured at the reference height is compared with the spectrum of the BLWT at the position of the collector in figure 4.6. The numerical and experimental spectra are in close agreement for $Wf/U_{ref} < 0.4$. At higher frequencies the spectrum of the numerical simulation decays rapidly. This is caused by a filtering effect of the finite element mesh on the small scale fluctuations. This filtering effect is unavoidable in numerical simulations and may be shifted to higher frequencies either by choosing a numerical scheme with improved resolution characteristics or refining the mesh.

Also shown in figure 4.6 is the autocorrelation. The autocorrelation is useful for quantifying the characteristic time scale of wind gusts. Using Taylor's frozen turbulence hypothesis [109], this may also be interpreted as the spatial extent in the streamwise direction. The gust sizes in the transverse and vertical directions of the experiment cannot be estimated from the available data and are unknown.

Mean velocity and turbulence intensity profiles are calculated at 7 equidistant positions from the inlet until $x/z_{ref} = 3.9$ and plotted in figures 4.7 and 4.8. Profiles from the wind tunnel experiment are plotted for comparison at the position of the collector (i.e., $x/z_{ref} = 3.25$).

The first profile at $x/z_{ref} = 0$ lies on the inlet boundary and has a steep gradient of velocity next to the ground which is approximated in the figure by a linear interpolation to the first interior measurement point. This corresponds approximately with the first element height. At the ground, the mean inlet velocity is zero and results in infinite turbulence intensity. For this reason, the turbulence intensity profile is only plotted over the interior points. The mean velocity increases with increasing distance from the inlet as it adjusts to the wall condition. This results in the decreasing values of turbulence intensity observed adjacent to the ground.

Farther from the ground, the turbulence intensity initially increases after the inlet. The model of [71] generates turbulent fluctuations in a periodic domain under the assumption of homogeneity. Therefore, the inlet fluctuations are not consistent with the zero penetration condition on the ground of the LES domain. As a result, fluctuations with a vertical velocity component close to the ground are forced to redirect in the horizontal direction as they react to the ground, contributing to higher velocity fluctuations in the streamwise direction.

Closer to the position of the collector, the profiles change more gradually and are in good agreement with the experimental profiles.

4.4 Wind Load Simulation

The instantaneous flow field for the pitch angle 30° is visualized in figure 4.9. Upstream from the collector, velocity fluctuations are seen with scales on the same order as the collector dimension. These large-scale fluctuations or gusts are a consequence of the time-varying inlet boundary condition and largely affect the peak and RMS wind loads. As demonstrated above, their statistics are in close agreement with the experimental data and they are expected to be a realistic representation of the turbulent conditions in the BLWT experiment. The influence of the collector on the flow field is seen in the wake region downstream of the collector with regions of high and low velocity separated by the thin shear layer originating from the separation point at the edge of the collector.

Drag statistics computed from the meshes in table 4.1 are compared with experimental results in figure 4.10. Mean and RMS drag are in close agreement for all three meshes, indicating that the results are nearly independent of mesh size. The largest differences in mean drag occur for 30°. For this pitch angle, the drag from mesh 1 differs from the experiment by 13%. Meshes 2 and 3 differ from the experiment by 9% and 10%, respectively. Based on these results, the mesh uncertainty is estimated to be on the order of a few percent. For RMS drag, the relative differences between numerical and experimental results are slightly larger and are in the range 15-17% for 0° and 180°. Larger variations in numerical results occur for peak values which are generally more difficult to estimate. Nevertheless, the peaks show good overall agreement with the largest difference between meshes 1 and 2 at 0° on the order of 18%. Additionally, the tendency of numerical results to overpredict RMS drag is not observed in the peak values.

Lift statistics are plotted in figure 4.11. The largest differences occur for the pitch angle 60°. This corresponds to the most severe loading in the vertical direction. At this pitch angle, the relatively sharp peaks in the mean and RMS are underpredicted by the numerical results of mesh 1 by 21% and 15%, respectively. The results of mesh 3 are in better agreement with a 12% underprediction in the mean and 3% in the RMS. At the remaining

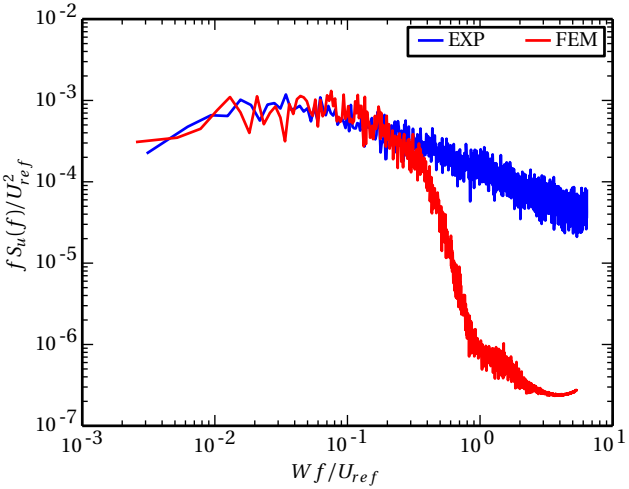

(a) Spectral density

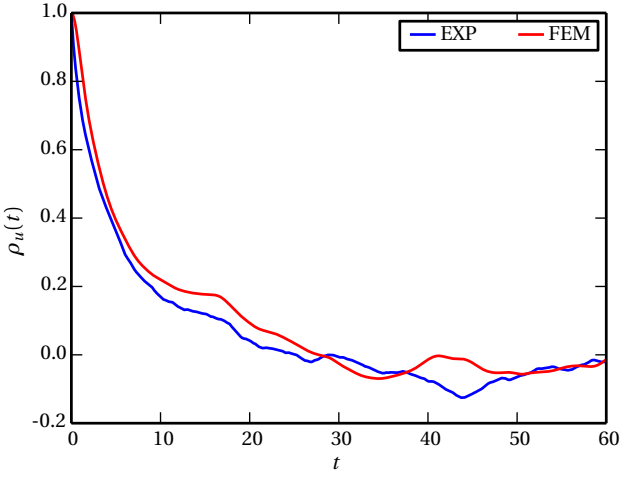

(b) Autocorrelation

Figure 4.6: Statistics measured at reference height z_{ref} in the empty channel for BLWT experiment (EXP) and finite element method (FEM).

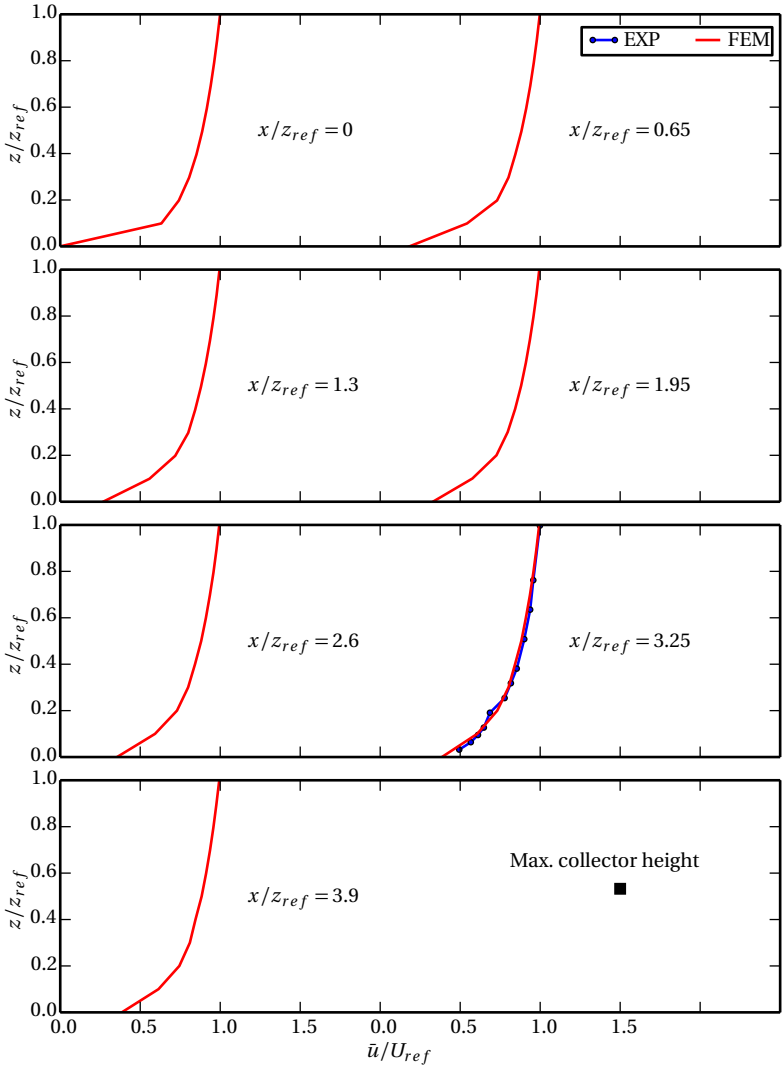

Figure 4.7: Mean velocity profiles for empty channel simulation. The measured profile from the BLWT experiment is plotted at the position of the collector.

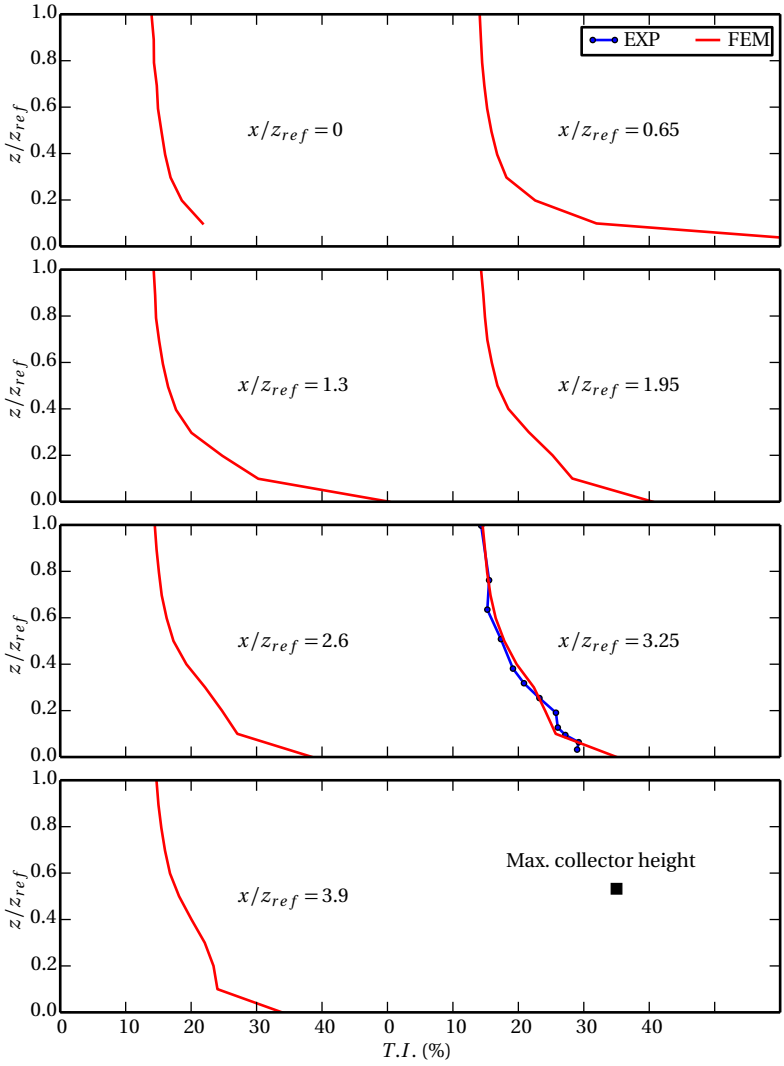

Figure 4.8: Turbulence intensity profiles for empty channel simulation. The measured profile from the BLWT experiment is plotted at the position of the collector.

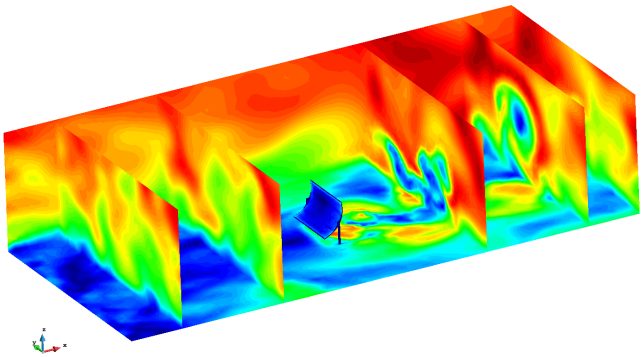

Figure 4.9: Instantaneous velocity contours for pitch angle 30°.

pitch angles the lift statistics are relatively insensitive to the variation in mesh size and are in close agreement with the experimental values.

The base moment statistics are plotted in figure 4.12 and follow a similar trend to the drag.

4.5 Summary

Overall, the mean, RMS and peak values of aerodynamics loads obtained from the numerical results are in good agreement with the values from the BLWT experiment. This confirms that the essential physics affecting wind loads on the collector are correctly modeled. A mesh study revealed that the largest mesh dependence for drag occurred close to the pitch angle 30° with uncertainty estimated to be on the order of a few percent. Slightly larger mesh dependence was observed for lift at the pitch angle 60°. For this pitch angle, the lift forces appeared especially sensitive to the mesh size close to the surface of the collector. Better agreement with the experimental results was observed with mesh refinement.

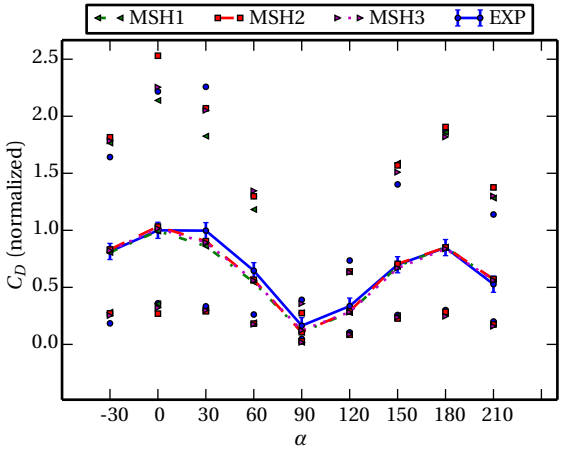

(a) Mean, maximum and minimum of drag coefficient

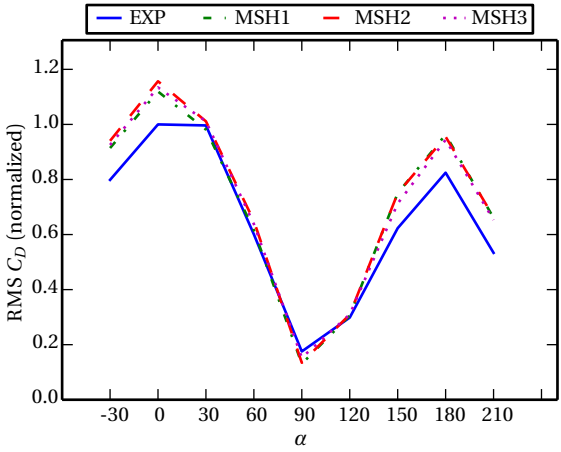

(b) Root mean square of drag coefficient

Figure 4.10: Statistics of drag coefficient: BLWT experiment (EXP) is compared with simulations from meshes 1-3. Error bars indicate the uncertainty due to the force-torque sensor.

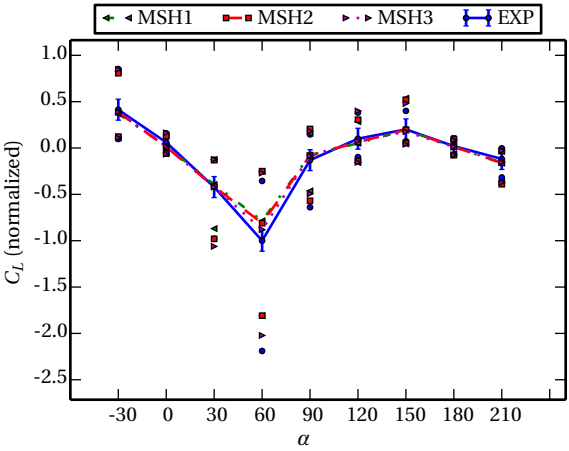

(a) Mean, maximum and minimum of lift coefficient

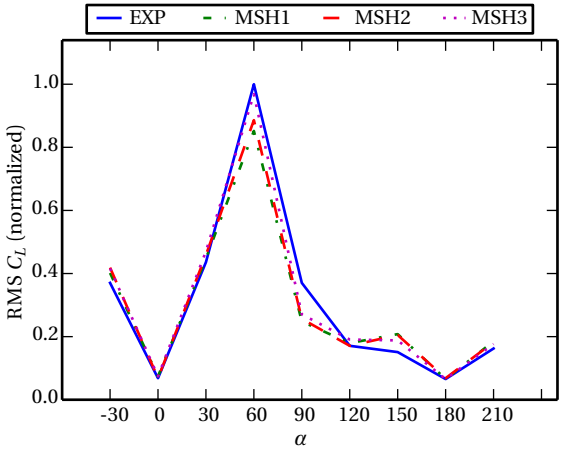

(b) Root mean square of lift coefficient

Figure 4.11: Statistics of lift coefficient: BLWT experiment (EXP) is compared with simulations from meshes 1-3. Error bars indicate the uncertainty due to the force-torque sensor.

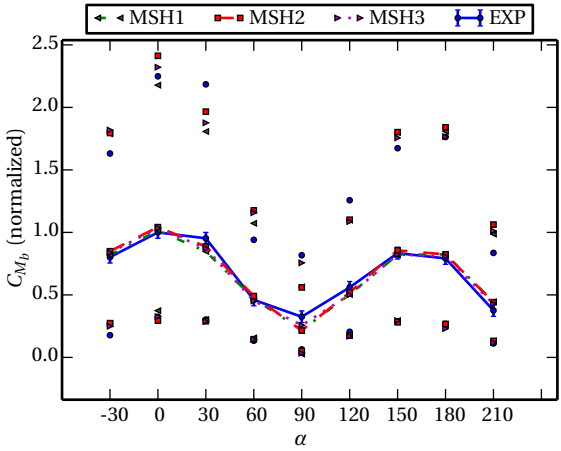

(a) Mean, maximum and minimum of moment coefficient

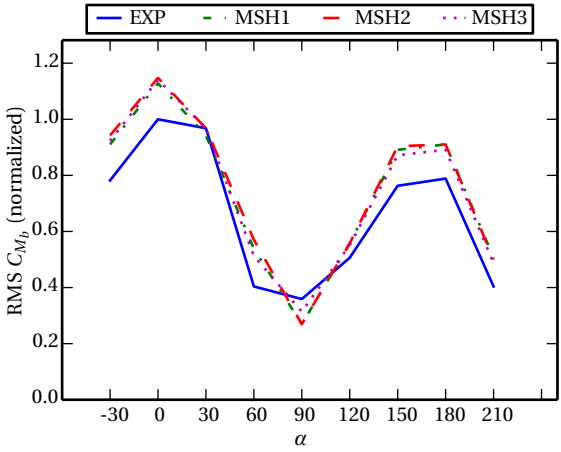

(b) Root mean square of moment coefficient

Figure 4.12: Statistics of moment coefficient: BLWT experiment (EXP) is compared with simulations from meshes 1-3. Error bars indicate the uncertainty due to the force-torque sensor.

Chapter 5

Fluid-Structure Interaction

The subject of FSI is generally concerned with the interdependence of motions of a fluid and a structure in contact with each other. The extent to which the motions of either fluid or structure subsystem depends on the other is problem dependent.

For example, the difference between the period of a gravity pendulum in a vacuum and in air is relatively small. As a result, Earth's gravity can be estimated to within reasonable accuracy from a simple pendulum experiment. Increases in measurement precision of early gravity experiments led to additional terms to correct for the effects of air. In 1828, Bessel [13] observed that the force due to gravity acts not only on the body but also on the mass of fluid accelerated by the body. Today this is known as the added-mass effect. Bessel's work resulted in a new correction for high precision pendulum experiments accounting for the increase in the moment of inertia in addition to the correction for buoyancy. It was later found that experiments on the added mass of a pendulum had been reported 50 years earlier by Du Buat [11].

While the added-mass effect is relatively small for the pendulum oscillating in air, it can be quite significant in other problems. As an example, Lamb [66] conducted a theoretical study based on the problem of subma-

rine signaling. He considered a circular plate of radius R and thickness h_s clamped at its edge and in contact with water. An expression for the eigenfrequency of the first symmetric mode of vibration was determined to have the form

$$f_n = \frac{f_{n0}}{\sqrt{1+\alpha_{fs}}} \tag{5.1}$$

with f_{n0} the eigenfrequency of the plate in a vacuum and

$$\alpha_{fs} = 0.6689 \frac{\rho_f R}{\rho_s h_s}. \tag{5.2}$$

For a 1/8-inch thick iron plate with a diameter of 7 inches, the eigenfrequency was found to be lowered by a factor of 0.542 due to the increase in inertia caused by the water. The increase in inertia by the water is equivalent to the addition of a second mass equal to the structural mass scaled by α_{fs}. As a result, the factor α_{fs} is sometimes referred to as the added-mass ratio. Lamb further noted that for "a plate vibrating in segments separated by nodal lines, the effect of the inertia of the water will be less, owing to the freedom of lateral motion near the surface, between adjacent segments in opposite phases" [66]. Thus, the largest added-mass effects occur for the lowest structural eigenfrequencies.

A more destructive form of FSI, which would later become known as flutter, was discovered after repeated instances of violent oscillations and catastrophic failures occurred in flight around the time of the First World War. The problem is characterized by [42]:

> Because it must be light, an airplane necessarily deforms appreciably under load. Such deformations change the distribution of the aerodynamic load, which in turn changes the deformations; the interacting feedback process may lead to *flutter*, a self-excited oscillation, often destructive, wherein energy is absorbed from the airstream.

The term flutter is also used in civil engineering to describe self-excited vibrations which depend on torsional motions or on the combination of torsional and translational motions. One of the most famous examples of this is the collapse of the Tacoma Narrows Bridge in 1940. The cause of the collapse was initially unknown but was later found to be due to torsional

flutter [75]. Unlike classical flutter, the mechanism driving the transfer of energy from the fluid to the structure depends on flow separation and vortex shedding. For this reason, it is sometimes referred to as stall flutter. In the case of stall flutter, airfoil theory based on potential flow equations is no longer valid and generally leads to erroneous results [96]. Instead, flutter derivatives must be estimated using wind tunnel experiments or numerical simulation.

Other classical examples of self-excited vibrations, otherwise referred to as aeroelastic instabilities, include galloping and the lock-in effect. Galloping occurs if the mean lift coefficient changes with angle of attack such that the aerodynamic follower force associated with small-amplitude transverse vibrations performs positive net work on the structure over each cycle of oscillation. It is known to cause large-amplitude vertical vibrations of frost-covered power lines and can also arise in slender, cable-like structures such as conveyor suspension bridges [33]. In contrast, self-excited vibrations due to the lock-in effect occur as a result of a synchronization between the transverse vibrations and vortex shedding process of prismatic bodies such as tall, cylindrical chimney stacks [121]. Synchronization of vortex shedding with transverse vibrations may occur when the ratio between the two frequencies is close to 1 and can result in significantly larger amplitudes than would otherwise be observed solely on the basis of mechanical resonance. According to the Eurocode [35], cross-wind forces due to vortex shedding should be considered for structures with slenderness ratios greater than 6. For smaller ratios, the transverse force coefficient of circular cylinders is close to zero [91]. Similar effects occur for rectangular cylinders [94]. Recently, the cause of the unexpected destruction of two non-prismatic roadside signboards has been identified as the lock-in effect [92].

In order to correctly capture these phenomena, FSI effects must be properly modeled. Otherwise, the model may significantly underestimate the response of the real structure. The primary aim of this chapter is to investigate numerical methods for the study of FSI problems encountered in civil engineering. We begin by studying an analytical model problem in section 5.1. The analytical model is then used to investigate the accuracy, stability and efficiency of several coupling algorithms in sections 5.2 and 5.3. A staggered coupling algorithm is studied in section 5.4. Finally, the performance of a mesh motion scheme is tested on a nonlinear benchmark problem in section 5.5.

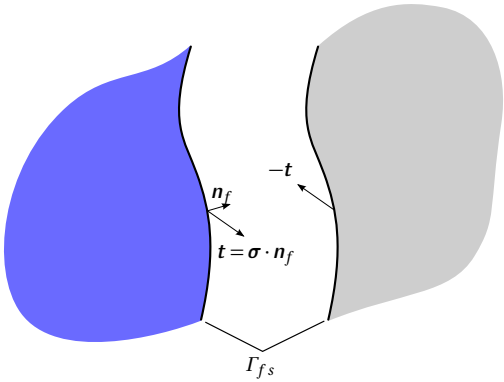

Figure 5.1: Fluid-structure interface.

The analysis of inviscid and viscous model problems presented in this chapter is based on [5] where the analytical model problem was originally proposed for analyzing FSI algorithms.

5.1 Analytical Model Problem

The problem of FSI is generally formulated using a continuum mechanics description. For a viscous fluid, the conservation of momentum on the fluid-structure interface Γ_{fs} is enforced by the constraint

$$\boldsymbol{\sigma}_f \cdot \boldsymbol{n}_f = \boldsymbol{\sigma}_s \cdot \boldsymbol{n}_f \quad \text{on } \Gamma_{fs}(t),\ 0 < t, \tag{5.3}$$

with $\boldsymbol{\sigma}_f, \boldsymbol{\sigma}_s$ the Cauchy stress tensor of the fluid and structure and $\boldsymbol{n}_f$ the outward pointing normal of the fluid domain (figure 5.1). Additionally, the conservation of mass is enforced by the constraint

$$\boldsymbol{u}_f \cdot \boldsymbol{n}_f = \frac{\partial \boldsymbol{d}_s}{\partial t} \cdot \boldsymbol{n}_f \quad \text{on } \Gamma_{fs}(t),\ 0 < t. \tag{5.4}$$

Finally, for a viscous fluid, the physical requirement of finite shear stress on the interface requires that the difference between the tangential components of velocity in the fluid and structure vanishes at the interface Γ_{fs}. The final set of constraints for the continuous problem is

$$\begin{aligned} \boldsymbol{u}_f &= \frac{\partial \boldsymbol{d}_s}{\partial t}, \\ \boldsymbol{\sigma}_f \cdot \boldsymbol{n}_f &= \boldsymbol{\sigma}_s \cdot \boldsymbol{n}_f \quad \text{on } \Gamma_{fs}(t),\ 0 < t. \end{aligned} \tag{5.5}$$

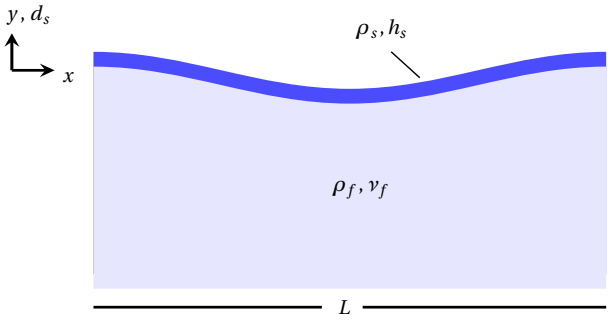

Figure 5.2: Fluid-structure model problem [5].

The two-dimensional model problem considered in this section (figure 5.2) is a modification of the standing wave problem for an incompressible fluid driven by surface tension [65]. The fluid domain consists of the half-plane $y < 0$. An infinite elastic beam or membrane structure is in contact with the fluid along the boundary $y = 0$. A single mode of vibration of the elastic structure is considered with the form

$$d_s(x,t) = \hat{d}_s(t)\cos\left(\frac{2\pi}{L}x\right). \tag{5.6}$$

5.1.1 Inviscid Fluid Problem

The inviscid solution of the standing wave problem is given in [65]. A derivation of the fluid solution based on a Fourier series representation is included here for completeness of the solution to the FSI problem and because it was not found in the literature. The fluid subproblem for a prescribed interface velocity $a_{,t}$ is

$$\begin{cases} \rho_f \frac{\partial \boldsymbol{u}_f}{\partial t} + \nabla p_f = 0 & \text{in } \Omega_f \times (0,T), \\ \nabla \cdot \boldsymbol{u}_f = 0 & \text{in } \Omega_f \times (0,T), \\ \boldsymbol{u}_f \cdot \boldsymbol{n}_f = a_{,t}\cos\left(\frac{2\pi}{L}x\right) & \text{on } \Gamma_{fs}. \end{cases} \tag{5.7}$$

Only small perturbations are considered here such that the interface condition may be replaced by

$$v_f = a_{,t}\cos\left(\frac{2\pi}{L}x\right) \quad \text{on } y = 0. \tag{5.8}$$

Additionally, the fluid velocity is assumed to be small such that the nonlinear convection term is negligible.

The inviscid flow is irrotational and may be expressed by a potential ϕ as $\boldsymbol{u}_f = \nabla\phi$. Substituting the Fourier series expansion

$$\phi = \sum_{m\geq 1}\left[\hat{\phi}_c(m,y,t)\cos\left(\frac{2\pi m}{L}x\right) + \hat{\phi}_s(m,y,t)\sin\left(\frac{2\pi m}{L}x\right)\right] \tag{5.9}$$

into the divergence free condition results in

$$\begin{aligned}\sum_{m\geq 1}\Bigg[&\left(\frac{\partial^2\hat{\phi}_c}{\partial y^2}(m,y,t) - \left(\frac{2\pi m}{L}\right)^2\hat{\phi}_c(m,y,t)\right)\cos\left(\frac{2\pi m}{L}x\right)\\ &+\left(\frac{\partial^2\hat{\phi}_s}{\partial y^2}(m,y,t) - \left(\frac{2\pi m}{L}\right)^2\hat{\phi}_s(m,y,t)\right)\sin\left(\frac{2\pi m}{L}x\right)\Bigg] = 0.\end{aligned} \tag{5.10}$$

This leads to a set of second-order linear homogeneous differential equations for $\hat{\phi}_c(m,y,t)$ and $\hat{\phi}_s(m,y,t)$. The general solution is

$$\hat{\phi}_c(m,y,t) = \tilde{g}_c(m,t)\exp\left(\frac{2\pi m}{L}y\right) + \tilde{h}_c(m,t)\exp\left(-\frac{2\pi m}{L}y\right), \tag{5.11}$$

$$\hat{\phi}_s(m,y,t) = \tilde{g}_s(m,t)\exp\left(\frac{2\pi m}{L}y\right) + \tilde{h}_s(m,t)\exp\left(-\frac{2\pi m}{L}y\right). \tag{5.12}$$

The requirement that the solution remains bounded as $y \to -\infty$ implies $\tilde{h}_s = \tilde{h}_c = 0$. The remaining boundary condition at $y = 0$ is

$$\begin{aligned}\frac{\partial\phi}{\partial y} &= \sum_{m\geq 1}\left[\tilde{g}_c(m,t)\left(\frac{2\pi m}{L}\right)\cos\left(\frac{2\pi m}{L}x\right) + \tilde{g}_s(m,t)\left(\frac{2\pi m}{L}\right)\sin\left(\frac{2\pi m}{L}x\right)\right]\\ &= a_{,t}\cos\left(\frac{2\pi}{L}x\right),\end{aligned} \tag{5.13}$$

which is satisfied for $\tilde{g}_s = 0$ and

$$\tilde{g}_c(m,t) = \begin{cases} \frac{L}{2\pi}a_{,t}(t) & \text{if } m = 1,\\ 0 & \text{else.}\end{cases} \tag{5.14}$$

Substituting into equations (5.11), (5.12) and (5.9), the final form of the velocity potential is

$$\phi(x,y,t)=\frac{L}{2\pi}a_{,t}(t)\exp\left(\frac{2\pi}{L}y\right)\cos\left(\frac{2\pi}{L}x\right). \tag{5.15}$$

The pressure is obtained from the conditions

$$\frac{\partial p_f}{\partial x}=-\rho_f\frac{\partial u_f}{\partial t}=\rho_f a_{,tt}(t)\exp\left(\frac{2\pi}{L}y\right)\sin\left(\frac{2\pi}{L}x\right), \tag{5.16}$$

$$\frac{\partial p_f}{\partial y}=-\rho_f\frac{\partial v_f}{\partial t}=-\rho_f a_{,tt}(t)\exp\left(\frac{2\pi}{L}y\right)\cos\left(\frac{2\pi}{L}x\right). \tag{5.17}$$

The additional condition $\lim_{y\to-\infty}p_f=0$ implies

$$p_f(x,y,t)=-\frac{\rho_f L}{2\pi}a_{,tt}(t)\exp\left(\frac{2\pi}{L}y\right)\cos\left(\frac{2\pi}{L}x\right). \tag{5.18}$$

Finally, the complete potential solution is

$$\begin{cases} u_f(x,y,t)=-a_{,t}(t)\exp\left(\frac{2\pi}{L}y\right)\sin\left(\frac{2\pi}{L}x\right),\\ v_f(x,y,t)=a_{,t}(t)\exp\left(\frac{2\pi}{L}y\right)\cos\left(\frac{2\pi}{L}x\right),\\ p_f(x,y,t)=-\frac{\rho_f L}{2\pi}a_{,tt}(t)\exp\left(\frac{2\pi}{L}y\right)\cos\left(\frac{2\pi}{L}x\right). \end{cases} \tag{5.19}$$

5.1.2 Membrane Problem

The initial value problem for the case of a membrane is

$$\begin{cases} \rho_s h_s\frac{\partial^2 d_s}{\partial t^2}-\sigma_s h_s\frac{\partial^2 d_s}{\partial x^2}=p_s & \text{in } (0,L)\times(0,T),\\ \frac{\partial d_s}{\partial x}=0 & \text{on } x=0,\ x=L,\\ d_s(x,0)=\hat{d}_{s0}\cos\left(\frac{2\pi}{L}x\right),\\ \frac{\partial d_s}{\partial t}(x,0)=\hat{v}_{s0}\cos\left(\frac{2\pi}{L}x\right), \end{cases} \tag{5.20}$$

with surface load p_s and tension σ_s. From (5.19), the pressure at the fluid-structure interface has the form

$$p_s(x,t)=p_f(x,0,t)=-\frac{\rho_f L}{2\pi}a_{,tt}(t)\cos\left(\frac{2\pi}{L}x\right). \tag{5.21}$$

Therefore, the membrane problem admits a solution of the form

$$d_s(x,t) = \hat{d}_s(t)\cos\left(\frac{2\pi}{L}x\right). \tag{5.22}$$

The solution to the coupled FSI problem is obtained by solving

$$\begin{cases} \left(\rho_s h_s + \frac{\rho_f L}{2\pi}\right)\hat{d}_{s,tt} + \frac{4\pi^2\sigma_s h_s}{L^2}\hat{d}_s = 0, \\ \hat{d}_s(0) = \hat{d}_{s0}, \\ \hat{d}_{s,t}(0) = \hat{v}_{s0}. \end{cases} \tag{5.23}$$

The solution,

$$\hat{d}_s(t) = \sqrt{\hat{d}_{s0}^2 + \frac{\hat{v}_{s0}^2}{\omega_n^2}}\,\sin\left(\omega_n t + \tan^{-1}\left[\frac{\omega_n \hat{d}_{s0}}{\hat{v}_{s0}}\right]\right), \tag{5.24}$$

has the same form as a membrane vibrating in a vacuum. The added-mass of the fluid results in a modified frequency of oscillation ω_n, which is related to the frequency in a vacuum $\omega_{n0} = \sqrt{4\pi^2\sigma_s/\rho_s L^2}$ by

$$\omega_n = \frac{\omega_{n0}}{\sqrt{1+\alpha_{fs}}} \tag{5.25}$$

with the added-mass ratio

$$\alpha_{fs} = \frac{\rho_f L}{2\pi\rho_s h_s}. \tag{5.26}$$

Here, the added-mass ratio is equivalent to the ratio between the fluid mass in a semicircle with an arc length of L and the mass of a membrane segment of length L.

5.1.3 Beam Problem

The initial value problem for the case of a thin beam is

$$\begin{cases} \rho_s h_s \frac{\partial^2 d_s}{\partial t^2} + \frac{E h_s^3}{12}\frac{\partial^4 d_s}{\partial x^4} = p_s & \text{in } (0,L)\times(0,T), \\ \frac{\partial d_s}{\partial x} = 0 & \text{on } x=0,\ x=L, \\ \frac{\partial^3 d_s}{\partial x^3} = 0 & \text{on } x=0,\ x=L, \\ d_s(x,0) = \hat{d}_{s0}\cos\left(\frac{2\pi}{L}x\right), & \\ \frac{\partial d_s}{\partial t}(x,0) = \hat{v}_{s0}\cos\left(\frac{2\pi}{L}x\right), & \end{cases} \tag{5.27}$$

which admits a solution of the form given by (5.22). The analog of (5.23) for the beam problem is

$$\begin{cases} \left(\rho_s h_s + \frac{\rho_f L}{2\pi}\right)\hat{d}_{s,tt} + \frac{4\pi^4 E h_s^3}{3L^4}\hat{d}_s = 0, \\ \hat{d}_s(0) = \hat{d}_{s0}, \\ \hat{d}_{s,t}(0) = \hat{v}_{s0}. \end{cases} \tag{5.28}$$

Thus, the solution to the beam FSI problem has the form of (5.24), (5.25) and (5.26) with $\omega_{n0} = \sqrt{4\pi^4 E h_s^2/3\rho_s L^4}$.

5.1.4 Viscous Fluid Problem

The above inviscid fluid problem is useful for numerical analysis of FSI algorithms and verification of software implementations. In order to also test numerical solutions for viscous fluid problems, the FSI problem described above is extended to include viscous effects in this section.

In order to simplify the solution, only the normal component of the traction is considered. The traction boundary conditions applied on the fluid-structure interface are

$$-p_f + 2\mu_f \frac{\partial v_f}{\partial y} = -p_s \tag{5.29}$$

and

$$\mu_f\left(\frac{\partial v_f}{\partial x} + \frac{\partial u_f}{\partial y}\right) = 0 \tag{5.30}$$

with μ_f the dynamic viscosity. The fluid problem is

$$\begin{cases} \rho_f \frac{\partial \boldsymbol{u}_f}{\partial t} + \nabla p_f - \mu_f \nabla^2 \boldsymbol{u}_f = 0 & \text{in } \Omega_f \times (0,T), \\ \nabla \cdot \boldsymbol{u}_f = 0 & \text{in } \Omega_f \times (0,T), \\ \boldsymbol{u}_f \cdot \boldsymbol{n}_f = a_{,t} \cos\left(\frac{2\pi}{L}x\right) & \text{on } \Gamma_{fs}. \end{cases} \tag{5.31}$$

The solution to the viscous FSI problem is based on the work of [84] for the viscous standing wave problem. The interface motion has the form of (5.6) where $\hat{d}_s(t)$ satisfies

$$\begin{cases} \hat{d}_{s,\tau\tau} + 4\epsilon^* \hat{d}_{s,\tau} + \hat{d}_s \\ -4\epsilon\epsilon^* \int_0^\tau \left[\frac{\exp(-\epsilon(\tau-s))}{\sqrt{\pi\epsilon(\tau-s)}} - \operatorname{erfc}\sqrt{\epsilon(\tau-s)}\right]\hat{d}_{s,\tau}(s)ds = 0, \\ \hat{d}_s(0) = \hat{d}_{s0}, \\ \hat{d}_{s,\tau}(0) = \hat{v}_{s0}/\omega_n, \end{cases} \tag{5.32}$$

with

$$\tau = \omega_n t, \quad \epsilon = \frac{\mu_f}{\rho_f}\frac{4\pi^2}{L^2\omega_n}, \quad \epsilon^* = \left(\frac{\mu_f}{\rho_f + 2\pi\rho_s h_s/L}\right)\frac{4\pi^2}{L^2\omega_n}. \tag{5.33}$$

A derivation of the initial value problem is given in appendix B. It's solution is

$$\begin{aligned} &\hat{d}_s(\tau) = \tfrac{4\epsilon\epsilon^*\hat{d}_{s0}}{8\epsilon\epsilon^*+1}\operatorname{erfc}\sqrt{\epsilon\tau} \\ &+\textstyle\sum_{j=1}^{4}\frac{z_j}{\sigma_j}\left(\frac{\hat{d}_{s0}}{z_j^2-\epsilon} - \frac{\hat{v}_{s0}}{\omega_n}\right)\exp((z_j^2-\epsilon)\tau)\operatorname{erfc}(z_j\sqrt{\tau}), \end{aligned} \tag{5.34}$$

with $-z_j$ the roots of the polynomial

$$z^4 + (4\epsilon^* - 2\epsilon)z^2 - 4\sqrt{\epsilon}\epsilon^* z + 1 + \epsilon^2 \tag{5.35}$$

and $\sigma_j = \prod_{l\neq j}(z_l - z_j)$.

5.2 Time-Discrete Problem

The inviscid FSI problem in section 5.1 reduces to

$$\begin{cases} \left(1+\alpha_{fs}\right)\hat{d}_{s,tt} + \omega_{n0}^2\hat{d}_s = 0, \\ \hat{d}_s(0) = \hat{d}_{s0}, \\ \hat{d}_{s,t}(0) = \hat{v}_{s0}. \end{cases} \tag{5.36}$$

Numerical methods for FSI are generally formulated using separate variables for the fluid and structure and adding the coupling conditions on the interface. Therefore, a more useful form of (5.36) for numerical analysis is

$$\begin{cases} \hat{v}_{f,t} = -\frac{1}{\alpha_{fs}}\hat{f}_f, \\ \hat{v}_f = \hat{d}_{s,t}, \\ \hat{d}_{s,tt} + \omega_{n0}^2\hat{d}_s = \hat{f}_s, \\ \hat{f}_s = \hat{f}_f, \\ \hat{d}_s(0) = \hat{d}_{s0}, \\ \hat{d}_{s,t}(0) = \hat{v}_{s0}. \end{cases} \tag{5.37}$$

Problem (5.37) provides a useful basis for the numerical analysis of time discretizations and partitioning algorithms for FSI problems involving incompressible fluids. It is the analog of the SDOF problem used to study the numerical properties of time discretization schemes in structural dynamics (see, e.g., [50]). Causin et al. [18] derived the SDOF system for a similar problem by analyzing the spectrum of the added-mass operator. The SDOF system was subsequently used in [9] to analyze Robin transmission conditions of partitioned FSI problems. Similarly, an abstract SDOF model problem has been used in the works of [31, 53] to analyze the stability and accuracy of partitioned FSI algorithms.

In this work, the fluid is discretized using the BDF2 scheme:

$$\frac{3\hat{v}_f^n - 4\hat{v}_f^{n-1} + \hat{v}_f^{n-2}}{2\Delta t} = -\frac{1}{\alpha_{fs}}\hat{f}_f^n, \tag{5.38}$$

$$\hat{v}_f^n = \frac{3\hat{d}_s^n - 4\hat{d}_s^{n-1} + \hat{d}_s^{n-2}}{2\Delta t}. \tag{5.39}$$

The structural problem is discretized using the generalized-α method [21]:

$$\delta_{tt}\hat{d}_s^{n-\alpha_m} + \omega_{n0}^2\hat{d}_s^{n-\alpha_f} = \hat{f}_s^{n-\alpha_f}, \tag{5.40}$$

$$\delta_{tt}\hat{d}_s^{n-\alpha_m} = \alpha_m\delta_{tt}\hat{d}_s^{n-1} + (1-\alpha_m)\delta_{tt}\hat{d}_s^n, \tag{5.41}$$

$$\hat{d}_s^{n-\alpha_f} = \alpha_f\hat{d}_s^{n-1} + (1-\alpha_f)\hat{d}_s^n, \tag{5.42}$$

$$\hat{f}_s^{n-\alpha_f} = \alpha_f\hat{f}_s^{n-1} + (1-\alpha_f)\hat{f}_s^n. \tag{5.43}$$

The update equations, relating velocity and acceleration to displacement, are given by the Newmark method [79]:

$$\delta_t\hat{d}_s^n = \delta_t\hat{d}_s^{n-1} + (1-\gamma)\Delta t\,\delta_{tt}\hat{d}_s^{n-1} + \gamma\Delta t\,\delta_{tt}\hat{d}_s^n, \tag{5.44}$$

$$\hat{d}_s^n = \hat{d}_s^{n-1} + \Delta t\,\delta_t\hat{d}_s^n + (\frac{1}{2}-\beta)\Delta t^2\delta_{tt}\hat{d}_s^{n-1} + \beta\Delta t^2\delta_{tt}\hat{d}_s^n. \tag{5.45}$$

The generalized-α method defines the algorithm's 4 parameters as functions of a single user-defined parameter ρ_∞:

$$\alpha_m = \frac{2\rho_\infty - 1}{\rho_\infty + 1}, \qquad \alpha_f = \frac{\rho_\infty}{\rho_\infty + 1}, \tag{5.46}$$

$$\beta = \frac{1}{4}(1-\alpha_m+\alpha_f)^2, \qquad \gamma = \frac{1}{2} - \alpha_m + \alpha_f. \tag{5.47}$$

The parameter ρ_∞ determines the spectral radius of the amplification matrix in the high-frequency limit. For values less than one, it adds numerical dissipation at frequencies that are not accurately resolved by the time step size. The solution of the discrete problem for one time step can be obtained by solving

$$\boldsymbol{A}_1 \mathbf{y}^n = \boldsymbol{A}_2 \mathbf{y}^{n-1} \tag{5.48}$$

with

$$\mathbf{y}^n = \left[\hat{d}_s^{n-1} \;\; \hat{d}_s^n \;\; \Delta t \delta_t \hat{d}_s^n \;\; \Delta t^2 \delta_{tt} \hat{d}_s^n \;\; \Delta t \hat{v}_f^{n-1} \;\; \Delta t \hat{v}_f^n \;\; \Delta t^2 \hat{f}_f^n \right]^T, \tag{5.49}$$

$$\boldsymbol{A}_1 = \begin{bmatrix} 0 & (1-\alpha_f)(\omega_{n0}\Delta t)^2 & 0 & 1-\alpha_m & 0 & 0 & -(1-\alpha_f) \\ 0 & 0 & 1 & -\gamma & 0 & 0 & 0 \\ 0 & 1 & 0 & -\beta & 0 & 0 & 0 \\ 1 & 0 & 0 & 0 & 0 & 0 & 0 \\ 0 & 0 & 0 & 0 & 0 & 1.5 & \frac{1}{\alpha_{fs}} \\ 0 & -1.5 & 0 & 0 & 0 & 1 & 0 \\ 0 & 0 & 0 & 0 & 1 & 0 & 0 \end{bmatrix}, \tag{5.50}$$

and

$$\boldsymbol{A}_2 = \begin{bmatrix} 0 & -\alpha_f(\omega_{n0}\Delta t)^2 & 0 & -\alpha_m & 0 & 0 & \alpha_f \\ 0 & 0 & 1 & 1-\gamma & 0 & 0 & 0 \\ 0 & 1 & 1 & 0.5-\beta & 0 & 0 & 0 \\ 0 & 1 & 0 & 0 & 0 & 0 & 0 \\ 0 & 0 & 0 & 0 & -0.5 & 2 & 0 \\ 0.5 & -2 & 0 & 0 & 0 & 0 & 0 \\ 0 & 0 & 0 & 0 & 0 & 1 & 0 \end{bmatrix}. \tag{5.51}$$

For the linear problem, the solution at every time step can be expressed as

$$\boldsymbol{y}^n = (\boldsymbol{A}_1^{-1}\boldsymbol{A}_2)\boldsymbol{y}^{n-1} = \boldsymbol{A}\boldsymbol{y}^{n-1}. \tag{5.52}$$

The matrix $\boldsymbol{A}$ is called the amplification matrix. Its usefulness comes from the fact that the solution at any time step $\boldsymbol{y}^n$ can be expressed as

$$\boldsymbol{y}^n = \boldsymbol{A}\boldsymbol{y}^{n-1} = \boldsymbol{A}^2\boldsymbol{y}^{n-2} = \cdots = \boldsymbol{A}^n\boldsymbol{y}^0. \tag{5.53}$$

Let the characteristic polynomial of $\boldsymbol{A}$ be denoted by

$$p_{\boldsymbol{A}}(s) = s^p - \sum_{k=1}^{p} c_{p-k}\, s^{p-k} = 0. \tag{5.54}$$

Then applying the Cayley-Hamilton theorem $p_{\boldsymbol{A}}(\boldsymbol{A}) = \boldsymbol{0}$ and

$$\begin{aligned} \boldsymbol{y}^n &= \boldsymbol{A}^p \boldsymbol{A}^{n-p} \boldsymbol{y}^0 \\ &= \left(\sum_{k=1}^{p} c_{p-k} \boldsymbol{A}^{p-k} \right) \boldsymbol{A}^{n-p} \boldsymbol{y}^0 \\ &= \sum_{k=1}^{p} c_{p-k} \boldsymbol{y}^{n-k}. \end{aligned} \tag{5.55}$$

Equation (5.55) is a homogeneous linear difference equation, which may be used to solve for the value of any variable y_i^n in (5.49) provided the variable's last p values are known. At this point, the stability and accuracy of the mixed time discretization of the monolithic FSI problem can be analyzed using established techniques for linear multistep methods (see, e.g., [104]).

The solution to (5.55) is stable if the following root condition is satisfied[1]:

1. all roots of the characteristic polynomial $p_{\boldsymbol{A}}(\lambda_k) = 0$ satisfy $|\lambda_k| \leq 1$,
2. any roots on the unit circle have multiplicity of one.

Here the roots are the eigenvalues of the amplification matrix $\boldsymbol{A}$. Thus, the root condition is equivalent to stating that the spectral radius of the amplification matrix, defined by $\rho(\boldsymbol{A}) = \max_{p_{\boldsymbol{A}}(\lambda_k)=0} |\lambda_k|$, is less than or equal to one with all eigenvalues of multiplicity greater than one being strictly less than one. An alternative development leading to the same stability condition is outlined in [50].

[1] This is sometimes referred to as zero-stability, spectral stability or Dahlquist stability.

The amplification matrix is a function of three parameters: $\omega_{n0}\Delta t$, ρ_∞ and α_{fs}. Verification of the stability for all possible combinations of these parameters is difficult due to the complicated symbolic expressions involved. Therefore, following the approach of [31], the stability has been verified for several combinations of numerical parameters in figure 5.3. From figure 5.3, it is concluded that the coupling of the fluid problem (BDF2 scheme) and the structure problem (generalized-α scheme) satisfies the root condition for all time step sizes. Therefore, the algorithm is expected to behave unconditionally stable in time.

After verifying stability, the solution accuracy is checked by calculating the local truncation error of the update equation (5.55). The local truncation error is defined as the error caused by a single update step computed from the exact solution. For example, let $\hat{d}_s(t^n)$ denote the exact displacement of the structure at time t^n as obtained from the solution of (5.36). Then a single update step gives

$$\hat{d}_s^n = \sum_{k=1}^{p} c_{p-k}\hat{d}_s(t^{n-k}). \tag{5.56}$$

The local truncation error is then

$$\hat{d}_s(t^n) - \hat{d}_s^n = \hat{d}_s(t^n) - \sum_{k=1}^{p} c_{p-k}\hat{d}_s(t^{n-k}) = \mathcal{O}(\Delta t^{r+2}). \tag{5.57}$$

The order $\mathcal{O}(\Delta t^{r+2})$ can be found by replacing the exact solution at each time instant by a Taylor series expansion around a single time instant. Repeating the same procedure for $\Delta t\delta_t\hat{d}_s$ and $\Delta t^2\delta_{tt}\hat{d}_s$ results in local truncation errors for the velocity and acceleration of $\mathcal{O}(\Delta t^{r+1})$ and $\mathcal{O}(\Delta t^r)$, respectively. Here r denotes the order of the method. For all numerical parameters tested for the monolithic problem, it is found that $r = 2$ and thus the second-order accuracy of the BDF2 and generalized-α methods is preserved for the coupled FSI problem.

5.3 Iterative Coupling

The concurrent solution of fluid and structure subproblems combined with the interface transmission conditions for FSI simulations requires the tight integration of numerical algorithms from both disciplines. The

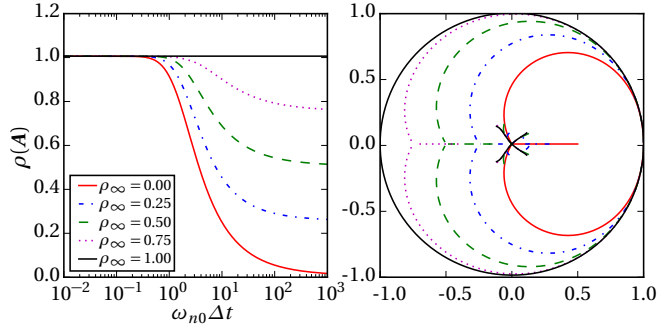

(a) $\alpha_{fs} = 0.01$

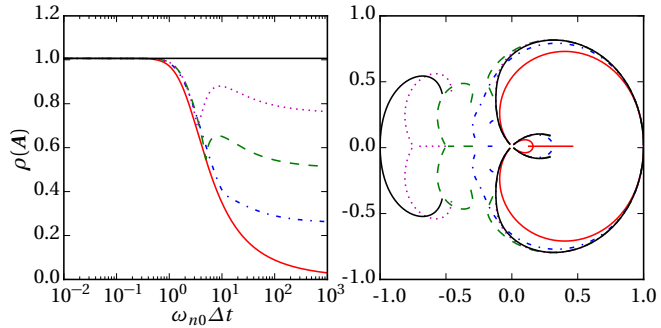

(b) $\alpha_{fs} = 1$

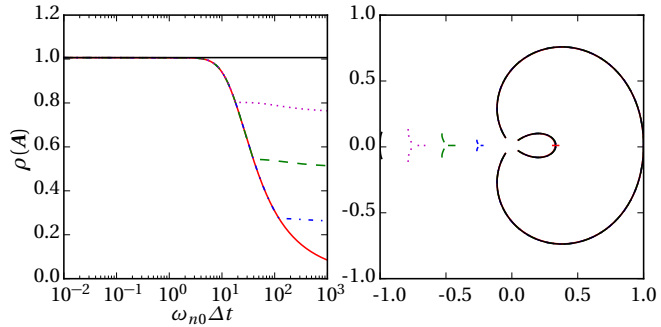

(c) $\alpha_{fs} = 100$

Figure 5.3: Spectral radius (left) and corresponding root diagram in the complex plane (right) for mixed BDF2 and generalized-α time discretizations.

development of coupling algorithms for FSI problems originated more than 40 years ago [81]. Since that time, FSI simulation has been applied to various problems ranging from biomechanics to bridge aerodynamics. This has led to a broad range of coupling techniques with various properties. When choosing a suitable coupling algorithm for a specific problem, it is important to consider these properties in relation to the problem under consideration in order to achieve a sensible tradeoff between simulation cost and modularity on the one hand and robustness and stability on the other.

Coupling techniques are normally classified as partitioned or monolithic. Monolithic approaches solve the coupled fluid and structure subproblems as a single system of equations. This approach is known to be robust with respect to the choice of system parameters, but it is generally known to suffer from ill-conditioned system matrices. As a result, specially designed preconditioners [46] and modified forms of the incompressible Navier-Stokes equations [93] may be required to improve the efficiency and make the simulation of large problems feasible. Alternatively, partitioned solvers split the coupled problem by solving the fluid and structure subproblems separately and updating the interface values between solution steps. For incompressible fluids, this procedure is normally performed iteratively until a desired level of convergence is achieved. By solving the fluid and structure subproblems separately, the efficiency and modularity of existing fluid and structure solvers is preserved. For this reason, partitioned solvers are commonly used.

Arguably, the most decisive factor affecting the choice of solver type is the added-mass ratio introduced at the beginning of this chapter and included in the analytical model problem described above. For low added-mass ratios, the dominant part of the inertia of the coupled system resides in the subdomain of the structure. As a result, structural deformations are tightly coupled to the inertial terms through the structural equations of motion. With increasing added-mass ratio, the dominant part of the inertia shifts to the fluid domain and the coupling of structural deformations with inertial terms occurs across the FSI interface. This has significant implications for partitioned solution procedures which solve the fluid and structure subproblems separately, updating the interface deformations and forces between solutions. For large added-mass ratios, small interface motions result in large forces, which are necessary in order to accelerate the relatively large fluid mass. This leads to well-known added-mass

instabilities [18].

In order to extend the range of applications for partitioned solvers and improve their efficiency, numerous partitioned algorithms have been proposed. Among the simplest algorithms are those employing block Gauss-Seidel iterations based on Dirichlet-Neumann partitioning with relaxation [63]. These methods are commonly used with black box solvers since the only requirement is the ability to update displacements on the fluid boundary and tractions on the structure boundary between solution steps. Such methods are often sufficient to solve FSI problems with moderate to low added-mass ratios, but they can fail at higher added-mass ratios. One strategy to improve the stability and convergence of the coupling iterations is to use quasi-Newton iterative schemes [30]. The main idea behind such schemes is to build an approximation of the Jacobian for the interface residual using information from previous iterations and use this to update the interface variables between iterations.

Depending on the accessibility of the internals of the flow solver, slightly more intrusive methods may also be applied. Such methods include the use of Robin boundary conditions on the FSI interface instead of the usual Dirichlet boundary condition [9] and the closely related method of artificial interface compressibility [85].

In this section, three iterative techniques based on Dirichlet-Neumann partitioning are reviewed and numerical experiments are performed to compare their performance and stability. It is noted that while we restrict the discussion of coupling techniques to a linear problem, general FSI problems are highly nonlinear. This does not pose a significant problem since the partitioned algorithm is applied to solve the linear system of equations arising at each nonlinear iteration. In practice however, the system of equations is often updated with the latest solution values in each coupling iteration. Nevertheless, the changes in the system matrix due to the nonlinear convective term and mesh motion within a time step are expected to be small, and the conclusions drawn from the linear problem are normally considered to hold for the nonlinear problem as well.

Before proceeding with the discussion of the coupling algorithms, Dirichlet-Neumann partitioning is demonstrated for the example of equations (5.38) through (5.47) or, equivalently, system (5.48). Here we omit the superscript n for all variables at the current time step to simplify the notation. The fluid partition is solved at each iteration, denoted by the superscript m, by applying a Dirichlet boundary condition on the interface

using the most recent estimate for the interface position $\hat{d}_s^{m-1}$:

$$\begin{cases} \text{Given } (\hat{d}_s^{m-1}, \hat{d}_s^{n-2}, \hat{d}_s^{n-1}, \hat{v}_f^{n-2}, \hat{v}_f^{n-1}), \text{ solve} \\ \delta_t \hat{d}_s^{m-1} = (3\hat{d}_s^{m-1} - 4\hat{d}_s^{n-1} + \hat{d}_s^{n-2})/2\Delta t, \\ \hat{v}_f^n = \delta_t \hat{d}_s^{m-1}, \\ \delta_t \hat{v}_f^m = (3\hat{v}_f^m - 4\hat{v}_f^{n-1} + \hat{v}_f^{n-2})/2\Delta t, \\ \delta_t \hat{v}_f^m = -\frac{1}{\alpha_{fs}} \hat{f}_f^m. \end{cases} \tag{5.58}$$

In a similar manner, the structure partition is solved using a Neumann boundary condition based on the force obtained from the solution of the fluid partition:

$$\begin{cases} \text{Given } (\hat{d}_s^{n-1}, \delta_t \hat{d}_s^{n-1}, \delta_{tt} \hat{d}_s^{n-1}, \hat{f}_s^m, \hat{f}_s^{n-1}), \text{ solve} \\ \hat{f}_s^{n-\alpha_f,m} = \alpha_f \hat{f}_s^{n-1} + (1-\alpha_f)\hat{f}_s^m, \\ \delta_{tt} \tilde{d}_s^{n-\alpha_m,m} + \omega_{n0}^2 \tilde{d}_s^{n-\alpha_f,m} = \hat{f}_s^{n-\alpha_f,m}, \\ \delta_{tt} \tilde{d}_s^{n-\alpha_m,m} = \alpha_m \delta_{tt} \hat{d}_s^{n-1} + (1-\alpha_m)\delta_{tt} \tilde{d}_s^m \\ \tilde{d}_s^{n-\alpha_f,m} = \alpha_f \hat{d}_s^{n-1} + (1-\alpha_f)\tilde{d}_s^m, \\ \tilde{d}_s^m = \hat{d}_s^{n-1} + \Delta t \delta_t \tilde{d}_s^m + (\frac{1}{2} - \beta)\Delta t^2 \delta_{tt} \hat{d}_s^{n-1} + \beta \Delta t^2 \delta_{tt} \tilde{d}_s^m, \\ \delta_t \tilde{d}_s^m = \delta_t \hat{d}_s^{n-1} + (1-\gamma)\Delta t \delta_{tt} \hat{d}_s^{n-1} + \gamma \Delta t \delta_{tt} \tilde{d}_s^m. \end{cases} \tag{5.59}$$

5.3.1 Relaxation

Relaxation schemes calculate a new estimate for the interface position as a weighted combination of $\hat{d}_s^{m-1}$ and $\tilde{d}_s^m$ as follows:

$$\hat{d}_s^m = \eta^{m-1} \tilde{d}_s^m + (1-\eta^{m-1})\hat{d}_s^{m-1}. \tag{5.60}$$

Constant under-relaxation uses a fixed value $\eta^m = \eta$. By choosing the relaxation factor to be sufficiently small, convergence of the coupling iterations can be realized. This can be seen by formulating the coupling iteration as the fixed point problem

$$\hat{d}_s^m = \mathcal{R} \circ \mathcal{S} \circ \mathcal{F}(\hat{d}_s^{m-1}; \alpha_{fs}, \omega_{n0}\Delta t, \eta) \tag{5.61}$$

where $\mathcal{S} \circ \mathcal{F}$ denotes the composition of the fluid (5.58) and structure (5.59) subproblems and $\mathcal{R}$ denotes the relaxation (5.60). For the BDF2 and

generalized-α schemes, the fluid and structure subsystems are

$$\hat{f}_f^m = -\frac{9\alpha_{fs}}{4\Delta t^2}\hat{d}_s^{m-1} + C_1 \tag{5.62}$$

and

$$\tilde{d}_s^m = \frac{(1-\alpha_f)\beta\Delta t^2}{(1-\alpha_m)+(1-\alpha_f)\beta(\omega_{n0}\Delta t)^2}\hat{f}_s^m + C_2. \tag{5.63}$$

An expression for (5.61) is obtained by substituting (5.62) into (5.63) and applying (5.60) to obtain

$$\hat{d}_s^m = \left[1-\eta\left(\frac{1-\alpha_m+(1-\alpha_f)\beta(9\alpha_{fs}/4+(\omega_{n0}\Delta t)^2)}{1-\alpha_m+(1-\alpha_f)\beta(\omega_{n0}\Delta t)^2}\right)\right]\hat{d}_s^{m-1} + C_3. \tag{5.64}$$

Here C_i, $i = 1,2,3$, describe all terms which depend on historical values and remain constant during the coupling iterations. Neither these terms nor the starting value $\hat{d}_s^{n,0}$ are relevant to the convergence of the coupling iterations[2]. By observing that for $0 \le \rho_\infty \le 1$, $0.5 \le 1-\alpha_m \le 2$ and $0.5 \le 1-\alpha_f \le 1$, it can be verified that the condition

$$0 < \eta < \frac{2(1-\alpha_m)+2(1-\alpha_f)\beta(\omega_{n0}\Delta t)^2}{1-\alpha_m+(1-\alpha_f)\beta(9\alpha_{fs}/4+(\omega_{n0}\Delta t)^2)} \tag{5.65}$$

makes the fixed point iteration (5.64) a contraction. Under this condition, the contraction mapping theorem (see, e.g., [78]) ensures that the iterations converge. For the single mode, the choice

$$\eta_{opt} = \frac{1-\alpha_m+(1-\alpha_f)\beta(\omega_{n0}\Delta t)^2}{1-\alpha_m+(1-\alpha_f)\beta(9\alpha_{fs}/4+(\omega_{n0}\Delta t)^2)} \tag{5.66}$$

results in a convergent solution in one iteration. This optimal convergence property is not realizable for general FSI problems because these usually

[2] In real FSI applications, the starting value must provide a reasonable approximation for the interface position so that the nonlinear fluid and structure subproblems converge.

consist of many modes, which cannot be efficiently decoupled. Nevertheless, the stability condition provides a useful way to choose the relaxation parameter after estimating the largest modal added-mass ratio.

The Aitken method [52] is sometimes used to accelerate coupling iterations by computing a dynamic relaxation factor based on two prior iterations. It has been used extensively for FSI problems and is reviewed in [63] where it is explained in terms of the secant method. Applied to the root finding problem

$$r^m = \mathcal{S} \circ \mathcal{F}(\hat{d}_s^{m-1}) - \hat{d}_s^{m-1} = \tilde{d}_s^m - \hat{d}_s^{m-1}, \tag{5.67}$$

the secant method estimates the updated position as

$$\hat{d}_s^m = \frac{\tilde{d}_s^m \hat{d}_s^{m-2} - \tilde{d}_s^{m-1} \hat{d}_s^{m-1}}{\hat{d}_s^{m-2} - \tilde{d}_s^{m-1} - \hat{d}_s^{m-1} + \tilde{d}_s^m}. \tag{5.68}$$

This can be written as

$$\hat{d}_s^m = \hat{d}_s^{m-1} + \eta^{m-1} r^m \tag{5.69}$$

with

$$\eta^{m-1} = -\frac{\hat{d}_s^{m-1} - \hat{d}_s^{m-2}}{r^m - r^{m-1}}. \tag{5.70}$$

This leads to its interpretation as a finite difference approximation of Newton's method where the dynamic relaxation factor η^m may be interpreted as an approximation relating variations in the residual to variations in the input variable. The Aitken method provides a way to compute η^m for vector quantities. In such cases, the problem is overdetermined and the scalar η^m must be estimated from a least-squares approximation:

$$\begin{aligned} \eta^{m-1} &= -\frac{(\boldsymbol{d}_s^{m-1} - \boldsymbol{d}_s^{m-2}) \cdot (\boldsymbol{r}^m - \boldsymbol{r}^{m-1})}{|\boldsymbol{r}^m - \boldsymbol{r}^{m-1}|^2} \\ &= -\eta^{m-2} \frac{\boldsymbol{r}^{m-1} \cdot (\boldsymbol{r}^m - \boldsymbol{r}^{m-1})}{|\boldsymbol{r}^m - \boldsymbol{r}^{m-1}|^2}. \end{aligned} \tag{5.71}$$

A comparison of the Aitken algorithm with other quasi-Newton methods is discussed in [30].

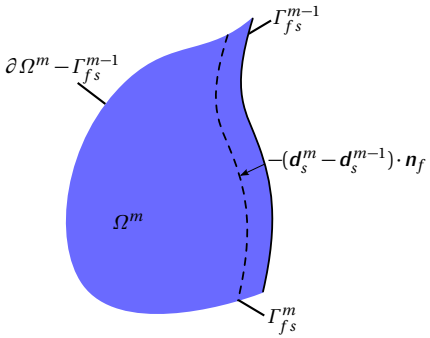

Figure 5.4: Fluid interface deformation for the m^{th} coupling iteration.

5.3.2 Interface Compressibility

A modification to the divergence free condition at the fluid-structure interface was presented by [85]. The method attempts to model the incompressibility constraint by approximating the interface motion between coupling iterations in order to improve stability and convergence of the coupling. Due to its similarity to artifical compressibility techniques used in CFD (see, e.g., §4.4.3, [36]), the method is sometimes referred to as artificial compressibility or interface (artificial) compressibility.

To illustrate the method, an arbitrary control volume is depicted adjacent to the fluid side of the fluid-structure interface in figure 5.4 at the m^{th} iteration. In Dirichlet-Neumann partitioning, the fluid problem is solved using the interface displacement $\boldsymbol{d}_s^{m-1}$ calculated in the previous iteration. This leads to added-mass instabilities when the fluid mass displaced by the interface is large relative to the structural mass. The displacement of the fluid occurs through the pressure, which is determined by the incompressibility constraint. Thus, it is preferable to apply the divergence free condition based on the interface motion of the current iteration $\boldsymbol{d}_s^m$. Since this is not known at the time the fluid problem is solved, it must be approximated. The divergence free condition is decomposed into a part that is known and a part that must be approximated:

$$\int_{\Omega^m} \nabla\cdot\boldsymbol{u}_f^m\, d\Omega = \int_{\partial\Omega^m - \Gamma_{fs}^{m-1}} \boldsymbol{u}_f^m\cdot\boldsymbol{n}_f\, d\Gamma + \int_{\Gamma_{fs}^{m-1}} \delta_t \boldsymbol{d}_s^{m-1}\cdot\boldsymbol{n}_f\, d\Gamma$$

$$+\int_{\Gamma_{fs}^{m}} \delta_t \boldsymbol{d}_s^m \cdot \boldsymbol{n}_f \, d\Gamma - \int_{\Gamma_{fs}^{m-1}} \delta_t \boldsymbol{d}_s^{m-1} \cdot \boldsymbol{n}_f \, d\Gamma. \tag{5.72}$$

The second part of (5.72) is approximated by

$$\begin{aligned}
&\int_{\Gamma_{fs}^{m}} \delta_t \boldsymbol{d}_s^m \cdot \boldsymbol{n}_f \, d\Gamma - \int_{\Gamma_{fs}^{m-1}} \delta_t \boldsymbol{d}_s^{m-1} \cdot \boldsymbol{n}_f \, d\Gamma \\
&\qquad \approx \int_{\Gamma_{fs}^{m-1}} (\delta_t \boldsymbol{d}_s^m - \delta_t \boldsymbol{d}_s^{m-1}) \cdot \boldsymbol{n}_f \, d\Gamma \\
&\qquad \approx \int_{\Gamma_{fs}^{m-1}} \frac{1}{\gamma_{IC}} (p_f^m - p_f^{m-1}) d\Gamma.
\end{aligned} \tag{5.73}$$

The parameter γ_{IC} relates variations in the normal component of the interface velocity to variations in the fluid pressure. One way to estimate this parameter is by building a reduced-order model based on the values of interface pressure and velocity from previous iterations in a similar approach as is done with quasi-Newton methods for approximating the interface Jacobian. Another is to use a model problem similar to the one presented in section 5.1. This approach was used by [9] who investigated the use of a Robin boundary condition. The similarity between the Robin fluid boundary condition and interface compressibility can be seen by expressing the latter as

$$\gamma_{IC} \delta_t \boldsymbol{d}_s^m \cdot \boldsymbol{n}_f - p_f^m = \gamma_{IC} \delta_t \boldsymbol{d}_s^{m-1} \cdot \boldsymbol{n}_f - p_f^{m-1} \tag{5.74}$$

and was discussed in the context of the finite volume method by [29].

For the numerical studies conducted in this work, the simplified model problem is used to estimate γ_{IC}. Using the linear structural model (5.59), a change in pressure is related to a change in interface motion by

$$\begin{aligned}
\hat{p}_s^m - \hat{p}_s^{m-1} &= \rho_s h_s (\hat{f}_s^m - \hat{f}_s^{m-1}) \\
&= \frac{\rho_s h_s (1-\alpha_m)}{(1-\alpha_f)} (\delta_{tt} \hat{d}_s^m - \delta_{tt} \hat{d}_s^{m-1}) + \rho_s h_s \omega_{n0}^2 (\hat{d}_s^m - \hat{d}_s^{m-1}) \\
&= \rho_s h_s \left[\frac{(1-\alpha_m)}{\gamma \Delta t (1-\alpha_f)} + \left(1 + \frac{\beta}{\gamma}\right) \Delta t \, \omega_{n0}^2 \right] (\delta_t \hat{d}_s^m - \delta_t \hat{d}_s^{m-1}).
\end{aligned} \tag{5.75}$$

L	$\hat{d}_{s0}$	$\hat{v}_{s0}$	σ_s	h_s	ρ_s	ρ_f	α_{fs}
2π	$2\pi \times 10^{-4}$	0	$12\pi^2 \times 10^3$	0.001	2000	1	0.5

Table 5.1: FSI membrane benchmark parameters.

Because artifical added-mass instabilities are caused by the structural modes with the lowest eigenfrequencies, $\omega_{n0}\Delta t$ is expected to be small and γ_{IC} can be simplified as

$$\gamma_{IC} = \frac{\rho_s h_s (1-\alpha_m)}{\gamma \Delta t (1-\alpha_f)}. \tag{5.76}$$

Equation (5.76) is used for the comparison of the interface compressibility method with the other coupling approaches discussed in this chapter.

5.3.3 Variation of Mesh Resolution

The aims of this section are the assessment of mesh resolution requirements for tracking the interface motion and the verification of the solution accuracy of the coupled FSI solver. The membrane version of the analytical model problem is used to create a benchmark problem with the parameters given in table 5.1.

The chosen parameters result in an inviscid period of $T = 1$. Three uniform meshes are considered with the mesh sizes h=$L/8$, $L/16$ and $L/32$. A time step size of $\Delta t = 0.005$ corresponding to 200 steps per inviscid period is used for each mesh. This time step size was found to be sufficiently small such that the errors in the numerical solution are primarily due to the mesh resolution. For the generalized-α method, a spectral radius of $\rho_\infty = 0.8$ is used. The Euclidean norm of the nodal interface displacements is used to determine the convergence of the coupling iterations with an absolute convergence tolerance of 1×10^{-11}. A symmetry boundary condition is applied on the left and right boundaries, and a zero pressure boundary condition is applied on the lower boundary, which has a distance of L to the interface. At this distance, disturbances to the fluid have decayed to less than 0.2% of their values at the interface.

The initial pressure distribution and interface deformation are depicted in figure 5.5 for a single mode of wavelength L. The interface displacements

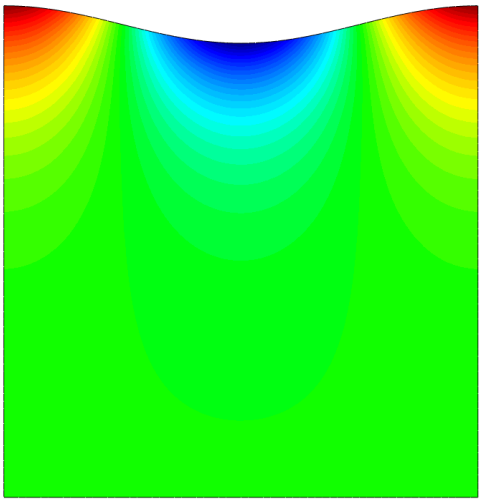

Figure 5.5: Initial pressure distribution and interface deformation (x400) for a single mode.

of inviscid ($\nu_f = 0$) and viscous ($\nu_f = 1$) simulations are computed over 4 periods of oscillation and plotted in figures 5.6 and 5.7. The interface error is quantified using the norms

$$||d_{sh} - d_s||_0 = \left[\int_0^T ||d_{sh}(t) - d_s(t)||^2_{L^2(0,L)} dt \right]^{1/2} \tag{5.77}$$

and

$$||d_{sh} - d_s||_1 = \left(||d_{sh} - d_s||_0^2 + ||\tfrac{\partial d_{sh}}{\partial x} - \tfrac{\partial d_s}{\partial x}||_0^2 \right)^{1/2} \tag{5.78}$$

with $||\cdot||_{L^2(0,L)}$ defined as the usual L^2 norm over the interface (see [36] for a detailed description). Table 5.2 shows the normalized interface errors for the inviscid and viscous simulations.

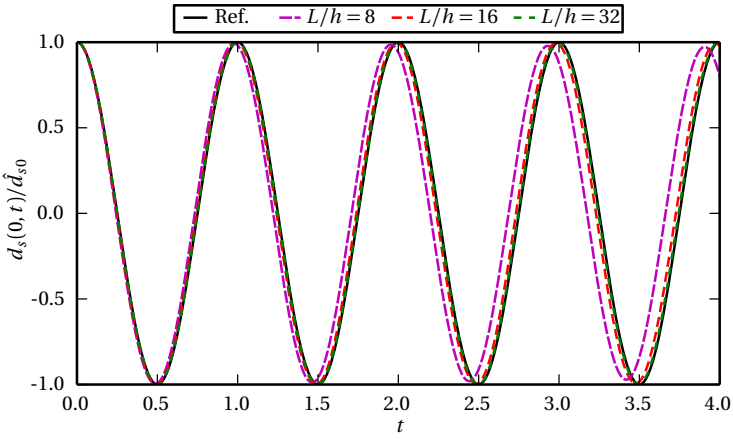

Figure 5.6: Interface displacement for a single mode with $\nu_f = 0$.

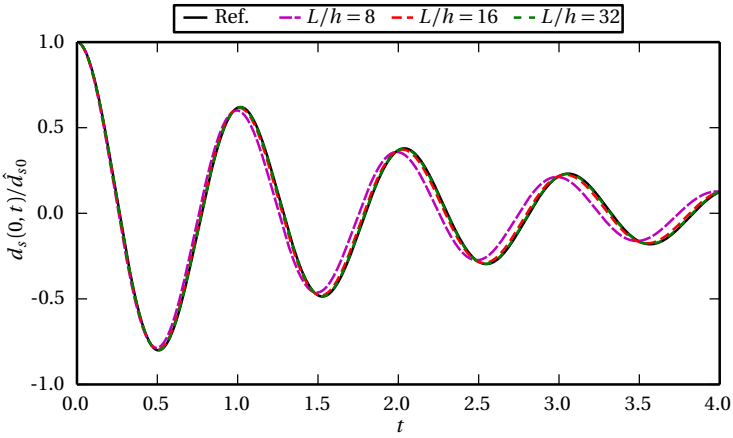

Figure 5.7: Interface displacement for a single mode with $\nu_f = 1$.

Mesh Size	$\|d_{sh}-d_s\|_0/\hat{d}_{s0}\sqrt{LT}$		$\|d_{sh}-d_s\|_1/\hat{d}_{s0}\sqrt{LT}$	
(L/h)	$\nu_f=0$	$\nu_f=1$	$\nu_f=0$	$\nu_f=1$
8	0.1661	0.0499	0.2576	0.0878
16	0.0462	0.0133	0.0846	0.0333
32	0.0125	0.0038	0.0284	0.0126

Table 5.2: Interface error for FSI membrane benchmark.

L	$\hat{d}_{s0,k}$	$\hat{v}_{s0,k}$	E	h_s	ρ_s	ν_f
2π	$0.5\pi\times10^{-4}$	0	$144\pi^2\times10^9$	0.001	2000	0.1

Table 5.3: Parameters for 4 mode FSI beam benchmark.

5.3.4 Performance of Coupling Algorithms

Next the performance of the different iterative algorithms is compared using the model problem. A beam is considered with 4 superimposed modes such that the resulting displacement has the form

$$d_s(x,t)=\sum_{k=0}^{4}\hat{d}_{s,k}(t)\cos\left(\frac{2\pi k}{L}x\right) \tag{5.79}$$

with the model parameters given in table 5.3. The fluid density is varied in order to control the added-mass ratio. The FSI problem is solved for each coupling algorithm for a time interval equal to the inviscid period of the first mode. The time step size and mesh size are chosen such that the highest mode is resolved with 16 elements per wavelength and 40 time steps per inviscid period of oscillation. The absolute convergence tolerance of the interface displacements is set to 1×10^{-7}.

Figure 5.8 shows the interface displacement for the above settings with an added-mass ratio of $\alpha_{fs}=8$. Constant relaxation, interface compressibility and the Aitken method are combined with the first-order predictor (P1)

$$\boldsymbol{d}_s^{n,0}=\boldsymbol{d}_s^{n-1} \tag{5.80}$$

and the second-order predictor (P2)

$$\boldsymbol{d}_s^{n,0}=\boldsymbol{d}_s^{n-1}+\Delta t\,\delta_t\boldsymbol{d}_s^{n-1}. \tag{5.81}$$

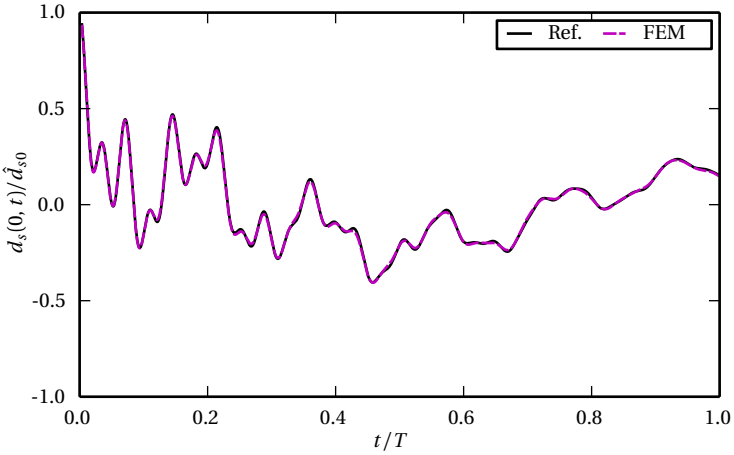

Figure 5.8: Interface displacement for 4 modes with $\alpha_{fs} = 8$.

For constant relaxation and for the initial Aitken iteration, the relaxation factor is given by (5.66).

The number of coupling iterations required for each algorithm is plotted against the added-mass ratio in figure 5.9. The least stable algorithm for the solvers used was the Aitken algorithm which failed to converge for $\alpha_{fs} = 1$ and above. The best performance was obtained for the interface compressibility algorithm with the number of coupling iterations remaining nearly constant across the range of added-mass ratios considered. In contrast, the number of iterations increases steadily for constant relaxation. A significant reduction in coupling iterations was realized for all algorithms by using a the second-order predictor (5.81). Simulations using a higher order predictor did not result in a significant improvement over the second-order predictor and are therefore omitted from figure 5.9 for the sake of clarity.

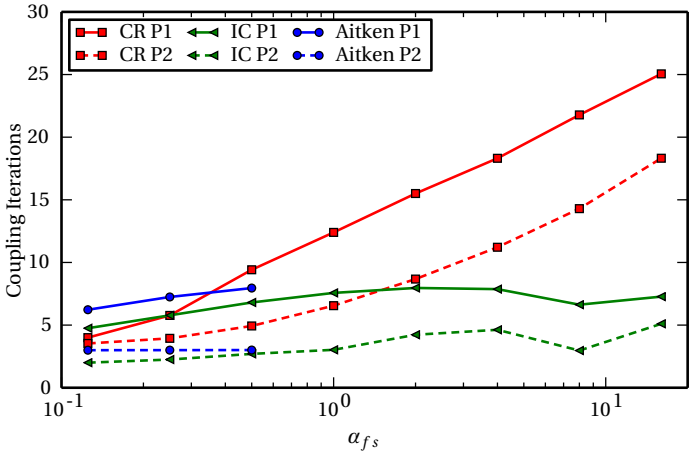

Figure 5.9: Comparison of the number of coupling iterations for constant relaxation (CR), interface compressibility (IC) and Aitken algorithms with first (P1) and second (P2) order predictors.

5.4 Staggered Coupling

Presently, the majority of coupling algorithms used in the context of partitioned FSI procedures for incompressible fluid models are iterative. Three techniques from within this class were compared in the previous section. Another class of partitioned procedures is known as staggered or explicit algorithms. In contrast to iterative algorithms, staggered algorithms only solve the fluid and structure subproblems once at each time step as illustrated in figure 5.10. Due to the fact that most currently available staggered algorithms become unstable even at relatively low added-mass ratios [38], these algorithms are less commonly applied to problems with incompressible fluid models. A noteworthy exception to this general rule is the stabilized algorithm based on a Robin boundary condition for the structure and Nitsche's method for imposing the Dirichlet boundary condition on the fluid as proposed by [16]. This algorithm is however not considered for the current work due to the complexity of the choice of parameters and their effects on the solution accuracy as well as the need for additional

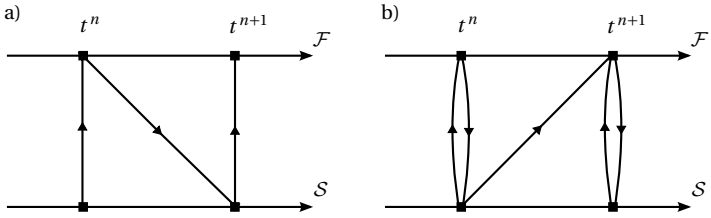

Figure 5.10: (a) Staggered coupling and (b) iterative coupling patterns for partitioned FSI simulations [8].

defect-correction iterations to recover optimal accuracy in time.

The staggered algorithm presented by [31] was shown to be stable up to moderate added-mass ratios while retaining second-order accuracy in time. The algorithm consists of a force predictor

$$\boldsymbol{f}_p^n = 2\boldsymbol{f}^{n-1} - \boldsymbol{f}^{n-2}, \tag{5.82}$$

which is applied to the structural problem at the new time step to obtain the updated displacements

$$\boldsymbol{d}_s^n = \mathcal{S}(\boldsymbol{f}_p^n). \tag{5.83}$$

The fluid problem is then solved using the updated displacements

$$\tilde{\boldsymbol{f}}^n = \mathcal{F}(\boldsymbol{d}_s^n), \tag{5.84}$$

and the interface forces are computed as a weighted combination of the force predictor and the forces from the fluid solver

$$\boldsymbol{f}^n = \beta_{SC}\tilde{\boldsymbol{f}}^n + (1-\beta_{SC})\boldsymbol{f}_p^n \tag{5.85}$$

with $0 < \beta_{SC} \leq 1$. The algorithm is summarized below.

The stability and accuracy of the staggered algorithm was analyzed by [31] for the case that the generalized-α method is used for both fluid and structure subproblems. The analysis procedure uses the same techniques as described in section 5.2 where the amplification matrix of the monolithic

Staggered Coupling Procedure (from [31]).

For each time step n:

1. Predict the interface force: $\boldsymbol{f}_p^n = 2\boldsymbol{f}^{n-1} - \boldsymbol{f}^{n-2}$.
2. Solve structure: $\boldsymbol{d}_s^n = \mathcal{S}(\boldsymbol{f}_p^n)$.
3. Solve fluid: $\tilde{\boldsymbol{f}}^n = \mathcal{F}(\boldsymbol{d}_s^n)$.
4. Update interface force $\boldsymbol{f}^n = \beta_{SC}\tilde{\boldsymbol{f}}^n + (1-\beta_{SC})\boldsymbol{f}_p^n$.

system is replaced by that of the staggered system. By applying the same analysis to the case where the generalized-α method is applied to the structure and the BDF2 discretization is applied to the fluid, the same conclusion of second-order accuracy in time is found to hold and is not discussed further here.

The amplification matrix of the staggered problem depends on the parameters $\omega_{n0}\Delta t, \alpha_{fs}, \beta_{SC}$ and ρ_∞. For a fixed set of parameters α_{fs}, β_{SC} and ρ_∞, the staggered algorithm is unconditionally stable if the root condition discussed in section 5.2 is satisfied for all $\omega_{n0}\Delta t > 0$. In order to investigate the unconditional stability as a function of the remaining parameters, an upper bound of the added-mass ratio denoted by $\bar{\alpha}_{fs}(\beta_{SC}, \rho_\infty)$ is defined as the largest added-mass ratio for which the algorithm remains unconditionally stable. The upper bound is evaluated numerically for several combinations of β_{SC} and ρ_∞ and plotted in figure 5.11. Based on this, the spectral radius of the generalized-α method for the structure is chosen to be $\rho_\infty = 0.16$ in the remainder of this work.

Next, the stability of the staggered algorithm is investigated on the fully discretized model for different combinations of coupling parameter β_{SC} and added-mass ratio α_{fs}. The discrete model introduces additional effects due to the spatial discretization and the segregated solution of the velocity and pressure which influence the stability. The focus here is on the effect due to the segregated or fractional-step solver. The segregated solution may be interpreted as the solution to a modified monolithic fluid problem [22]. By omitting convection and stabilization terms for simplicity,

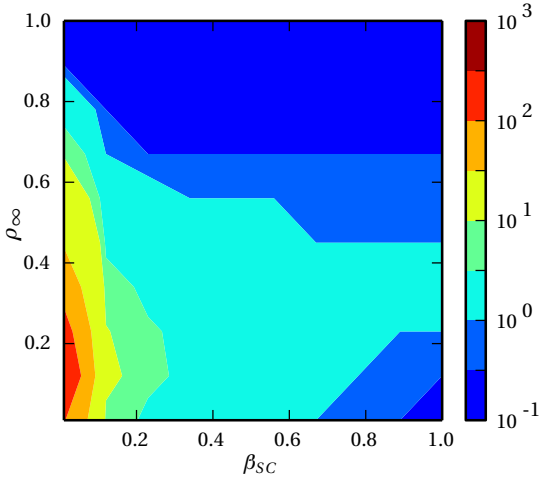

Figure 5.11: Contours of the largest stable added-mass ratio $\bar{\alpha}_{fs}(\beta_{SC},\rho_\infty)$.

the modified form of the Stokes problem can be expressed as[3]

$$\boldsymbol{M}\delta_t \boldsymbol{u}^n + \boldsymbol{G}\boldsymbol{p}^n = \boldsymbol{f}^n \tag{5.86}$$

$$\boldsymbol{D}\boldsymbol{u}^n = -\frac{2\Delta t}{3}\left(\boldsymbol{D}\boldsymbol{M}^{-1}\boldsymbol{G} - \boldsymbol{L}\right)\left(\boldsymbol{p}^n - \boldsymbol{p}^{n-1}\right) \tag{5.87}$$

where $-\boldsymbol{L}$ is the positive semi-definite Laplacian matrix, $\boldsymbol{G}$ is the gradient matrix and $\boldsymbol{D} = -\boldsymbol{G}^T$ is the divergence matrix. Thus, the velocity of the uncorrected fractional-step algorithm is not weakly divergence free in the sense that the right-hand side of (5.87) is no longer zero. It is shown in [22] that the operator $\boldsymbol{D}\boldsymbol{M}^{-1}\boldsymbol{G} - \boldsymbol{L}$ is positive semi-definite. The effect of this additional term is demonstrated using the inviscid membrane FSI model problem with parameters given in table 5.4 with the fluid density ρ_f used to adjust the added-mass ratio and a fixed time step size corresponding to 200 time steps per period.

By iteratively performing pressure corrections on the segregated solver, the pertubation to the monolithic system goes to zero and the segregated solution converges to the monolithic solution. To assess the stability behavior between the two limiting cases of fractional-step and monolithic

[3]The derivation of (5.86) and (5.87) follows readily from equations (73)-(75) of [24].

L	$\hat{d}_{s0}$	$\hat{v}_{s0}$	σ_s	h_s	ρ_s
2π	$2\pi \times 10^{-4}$	0	$8\pi^2 \times 10^3$	0.003	2000

Table 5.4: FSI membrane parameters for varying β_{SC} and α_{fs}.

solvers, simulations are carried out for a fixed number of pressure corrections per time step. Here we denote the number of pressure corrections per time step by N_{corr}. Moreover, the fluid-structure interface is not updated between pressure corrections and thus no FSI coupling iterations are performed. The model problem is solved over 4 periods of oscillation for $0 < \beta_{SC} \leq 0.3$ with $\Delta\beta_{SC} = 0.05$ and $0 < \alpha_{fs} \leq 1$ with $\Delta\alpha_{fs} = 0.1$. If the displacement exceeds $1.1\hat{d}_{s0}$ at any point in the simulation, the solution is considered unstable and no error measure is reported. Otherwise the interface error is computed according to (5.77). The stability regions and errors for $N_{corr} = 1, 2, 3$ and 4 are plotted in figure 5.12. The results show that the staggered algorithm becomes more stable as the fractional-step solution converges to the monolithic solution. It can also be seen that for a fixed time step size, the interface error tends to increase with increasing added-mass and decreasing β_{SC}.

The effect of changing the time step size is considered in figure 5.13. The simulations are carried out with pressure corrections with a pressure convergence tolerance of 1×10^{-3} and are thus comparable to the monolithic solution. For the two time step sizes shown, the stability region does not change as is expected for the case that the staggered algorithm is unconditionally stable. Further, the decrease in the maximum error from 0.105 to 0.024 when the time step size is reduced by half is consistent with the second-order accuracy determined from the analysis of the amplification matrix.

5.5 Verification of Mesh Motion Solver

5.5.1 Description of Mesh Motion Solver

In this work, the motion of the fluid boundary is tracked using an arbitrary Lagrangian-Eulerian (ALE) description. This description retains the accuracy of the body fitted mesh near the boundary since it allows the

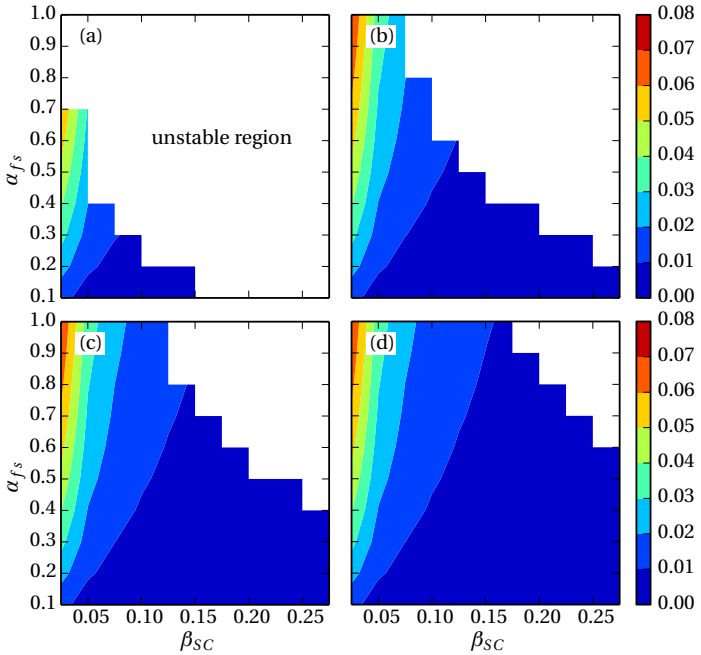

Figure 5.12: Interface error norm $||d_{sh} - d_s||_0$ of the staggered FSI simulation for fractional-step fluid solver with (a) $N_{corr} = 1$, (b) $N_{corr} = 2$, (c) $N_{corr} = 3$ and (d) $N_{corr} = 4$ pressure corrections.

interface motion to be tracked by updating the position of the fluid boundary according to the displacements of the structure. Additionally, using the BDF2 scheme to compute the mesh velocity $\delta_t \boldsymbol{\psi}_h^n$ preserves second-order accuracy in time [37]. The main drawback is that the mesh topology becomes distorted for large interface motions, causing the solver to fail unless remeshing is performed. This is not a problem for the current study since the structural deformations considered are relatively small. Nevertheless, the choice of mesh motion algorithm is critical for ensuring robust and accurate solutions in the wind engineering context. Specifically, the mesh quality must be preserved over long time intervals on the order of one hour and involving thousands of oscillations. Any deterioration with time may result in a loss of accuracy in the statistics or cause the simulation to be-

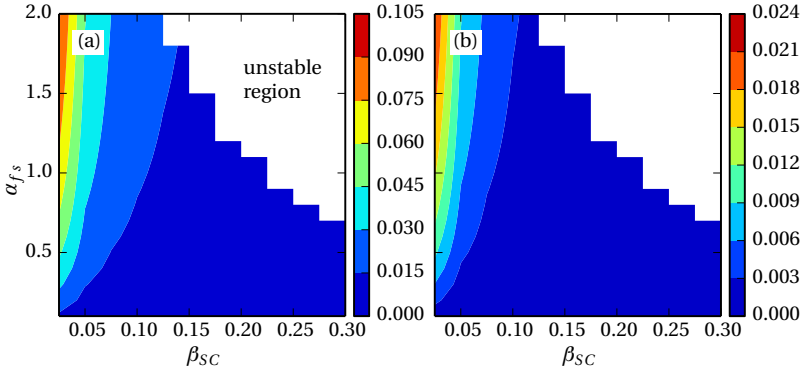

Figure 5.13: Interface error norm $||d_{sh}-d_s||_0$ of the staggered FSI simulation with pressure correction for time step sizes (a) $\Delta t = T/200$ [6] and (b) $\Delta t = T/400$.

come unstable and fail. The algorithm used in this work was implemented by [120] and is based on the method presented in [103]. An extension of the technique based on a predictor-corrector scheme was recently proposed by [48].

The model is based on the equations of linear elasticity where the elements are stiffened by the inverse of $\det(\boldsymbol{J}_K)$ raised to some power. Here $\det(\boldsymbol{J}_K)$ is the determinant of the element Jacobian matrix. From numerical tests (not shown here) $\det(\boldsymbol{J}_K)^{-1}$ was found to perform well over a range of structural motions and is used in this study. The mesh motion, denoted by $\boldsymbol{\psi}_h^n$, is computed from a prescribed structural displacement $\boldsymbol{d}_{sh}^n|_{\Gamma_{fs}}$ using the algorithm below.

The choice of mesh motion has a strong impact on the robustness of the coupled solution. By solving for the mesh displacement on the undeformed mesh, the mesh motion at the current time step does not depend on its displacement history and returns to the initial configuration upon setting the interface displacement to zero. Therefore, the mesh quality depends only on the range of structural motions and not on the number of time steps to be solved. As a result, long-time simulations may be computed to obtain nearly converged statistics without degrading the quality of the mesh or remeshing. Moreover, the Jacobian-based stiffening helps

Mesh Displacement

Given $\boldsymbol{d}_{sh}^n|_{\Gamma_{fs}}$, seek $\boldsymbol{\psi}_h^n \in \tilde{V}_h$, $\boldsymbol{\psi}_h^n = 0$ on $\partial\Omega_h - \Gamma_{fs}$, $\boldsymbol{\psi}_h^n = \boldsymbol{d}_{sh}^n$ on Γ_{fs} such that[4]:

$$\sum_{K\in\mathcal{T}_h}\int_K \det(\boldsymbol{J}_K)^{-1}\boldsymbol{\sigma}(\boldsymbol{\psi}_h^n):\boldsymbol{\epsilon}(\boldsymbol{v}_h)dK = 0 \tag{5.88}$$

for all $\boldsymbol{v}_h \in \tilde{V}_h$, $\boldsymbol{v}_h = 0$ on $\partial\Omega_h$.

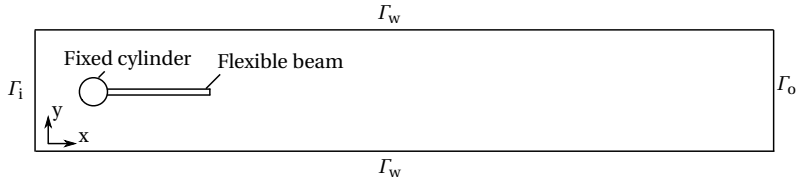

Figure 5.14: Domain for cylinder and flag FSI problem [113].

to preserve the mesh quality in the vicinity of the structure where elements are typically much smaller by transferring the mesh deformation to the regions consisting of larger elements which are of less interest.

5.5.2 Flow-Induced Vibration of a Flexible Beam

The analytical benchmark tests of sections 5.3 and 5.4 are useful for evaluating the performance and accuracy of FSI coupling algorithms, but they are restricted to small deformations. In order to test the mesh motion solver, the nonlinear benchmark problem of a flexible beam undergoing large displacements while interacting with a laminar flow as proposed in [113] is solved using the partitioned solver with interface compressibility for stabilization of the coupling iterations. The problem consists of a flexible beam mounted to a fixed cylinder in a laminar channel flow (Fig. 5.14) with inlet Γ_i, outlet Γ_o and wall Γ_w boundaries. The benchmark includes test

[4] Equation (5.88) is computed on the undeformed mesh using the equations of linear elasticity as described in [103].

cases for the structural solver, the fluid solver and the coupled FSI solver. We refer to [113] for a complete description of the test cases.

The reference quantities for comparison include the total drag and lift acting on the cylinder and flag as well as the vertical and horizontal tip displacement of the flag. Close to steady state, the forces and displacements vary periodically. In this regime, the range of force and displacement values are reported as

$$\text{mean} \pm \text{amplitude [frequency]}, \tag{5.89}$$

with

$$\text{mean} = \frac{1}{2}(\max + \min), \tag{5.90}$$

$$\text{amplitude} = \frac{1}{2}(\max - \min), \tag{5.91}$$

and

$$\text{frequency} = \frac{1}{\mathrm{T}}. \tag{5.92}$$

An extensive mesh refinement study was performed independently for both the fluid and structure. The results of three representative meshes of decreasing mesh size are presented for each subproblem below.

CSM3 Test Case

The structural model for the flag is discretized using solid hexahedral elements and the generalized-α time discretization. A single element is used in the z-dimension with plane strain condition applied to model the two-dimensional problem, resulting in twice the number of degrees of freedom compared with a two-dimensional quadrilateral element. Three structured meshes of decreasing mesh size are defined in table 5.5.

The tip displacement is computed for the beam in a vacuum under gravity load corresponding to the settings of the CSM3 benchmark. The time evolution is plotted for mesh 2 in figure 5.15 and the results from the three meshes are compared with the reference values in table 5.6.

The tip displacements, computed over three meshes and two time step sizes, have a maximum difference of 3.1% ± 3.1% [0.5%] for the x-displacement and 1.9% ± 1.0% [0.5%] for the y-displacement. The relative differences between the reference and mesh 3 ($\Delta t = 0.005$) are 0.3%

Mesh	Δx	Δy	N_{el}	N_{dof}
1	0.00319	0.00200	1100 (110×10)	4884
2	0.00234	0.00143	2100 (150×14)	9060
3	0.00201	0.00125	2800 (175×16)	11968

Table 5.5: Structure mesh sizes for FSI cylinder and flag benchmark.

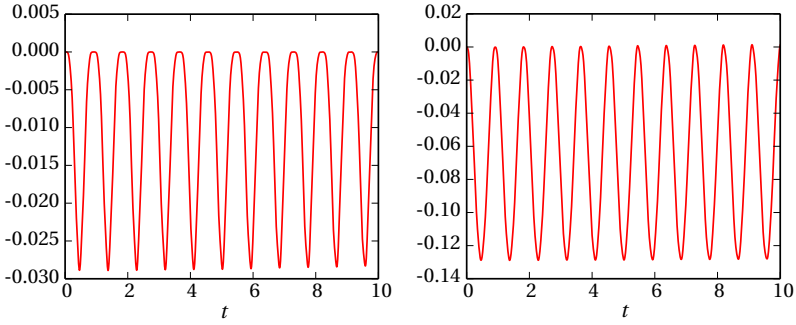

(a) d_{sx} (b) d_{sy}

Figure 5.15: CSM3 tip displacement for mesh 2.

Mesh (Δt)	d_{sx} [x 10^{-3}]	d_{sy} [x 10^{-3}]
1 (0.005)	-14.030 ± 14.031 [1.0989]	-63.064 ± 64.327 [1.0989]
2 (0.005)	-14.212 ± 14.212 [1.0929]	-63.416 ± 64.824 [1.0929]
3 (0.005)	-14.263 ± 14.264 [1.0929]	-63.520 ± 64.964 [1.0929]
3 (0.0025)	-14.469 ± 14.470 [1.0929]	-64.251 ± 64.780 [1.0959]
Ref. [113]	-14.305 ± 14.305 [1.0995]	-63.607 ± 65.160 [1.0995]

Table 5.6: CSM3 tip displacement.

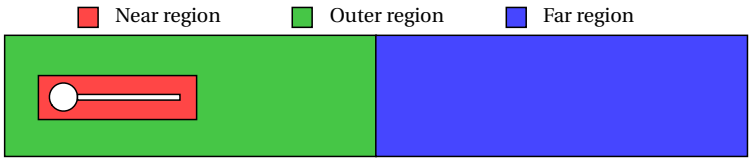

Figure 5.16: Mesh refinement regions for CFD of cylinder and flag.

Mesh	Mesh Size				N_{el}	N_{dof}
	Cylinder front	Near	Outer	Far		
1	0.0009	0.003	0.01	0.015	45479	70290
2	0.0006	0.002	0.01	0.015	78229	120162
3	0.0003	0.001	0.005	0.0075	264369	402180

Table 5.7: Fluid mesh sizes for FSI cylinder and flag benchmark.

± 0.3% [0.6%] for the x-displacement and 0.1% ± 0.3% [0.6%] for the y-displacement.

CFD3 Test Case

The CFD3 benchmark is used to test the fluid model and consists of a parabolic inlet profile of velocity with a bulk velocity equal to 2 and a Reynolds number of 200. A manual mesh generation procedure was used with mesh refinement regions shown in figure 5.16. The height of the near region was chosen to enclose the upper and lower shear layers originating from the cylinder. Additionally, a finer surface mesh size was applied to the front half of the cylinder. The three fluid mesh sizes are given in table 5.7.

The total lift and drag force on the cylinder and flag are plotted in figure 5.17. The forces are compared with the reference in table 5.8. The drag and lift forces, computed over three meshes and two time step sizes, have a maximum difference of 0.3% ± 4.6% [0.4%] and 19.4% ± 3.1% [1.3%], respectively. The relative differences between the reference and mesh 3 ($\Delta t = 0.002$) are 0.04% ± 0.7% [0.7%] and 9.6% ± 0.3% [0.7%].

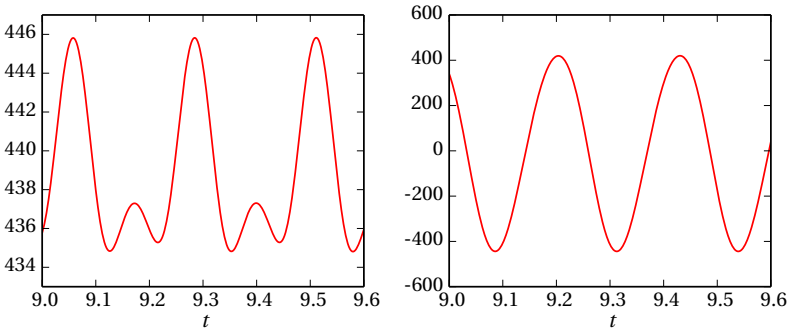

(a) Drag

(b) Lift

Figure 5.17: CFD3 forces for mesh 2.

Mesh (Δt)	Drag	Lift
1 (0.002)	440.83 ± 5.4185 [4.4248]	-14.735 ± 425.66 [4.3860]
2 (0.002)	440.32 ± 5.5153 [4.4248]	-12.344 ± 431.91 [4.4248]
3 (0.002)	439.63 ± 5.6584 [4.4248]	-13.038 ± 439.04 [4.4248]
3 (0.001)	439.60 ± 5.6658 [4.4444]	-13.374 ± 438.01 [4.4444]
Ref. [113]	439.45 ± 5.6183 [4.3956]	-11.893 ± 437.81 [4.3956]

Table 5.8: Forces on cylinder and flag for CFD3.

FSI3 Test Case

The FSI3 benchmark is simulated for meshes 1 and 2. In both cases, the FSI mesh is constructed from the meshes of the CSM3 and CFD3 test cases with the same index. The iterative partitioned algorithm with interface compressibility is applied using a second-order predictor. This choice of partitioned algorithm is due to the relatively high added mass of the benchmark problem. In all cases, the relative and absolute convergence tolerance for the FSI coupling iterations are 1×10^{-3} and 1×10^{-9}, respectively. Pressure contours are plotted over approximately one period in figure 5.18. The deformation of mesh 2 is shown in figure 5.19.

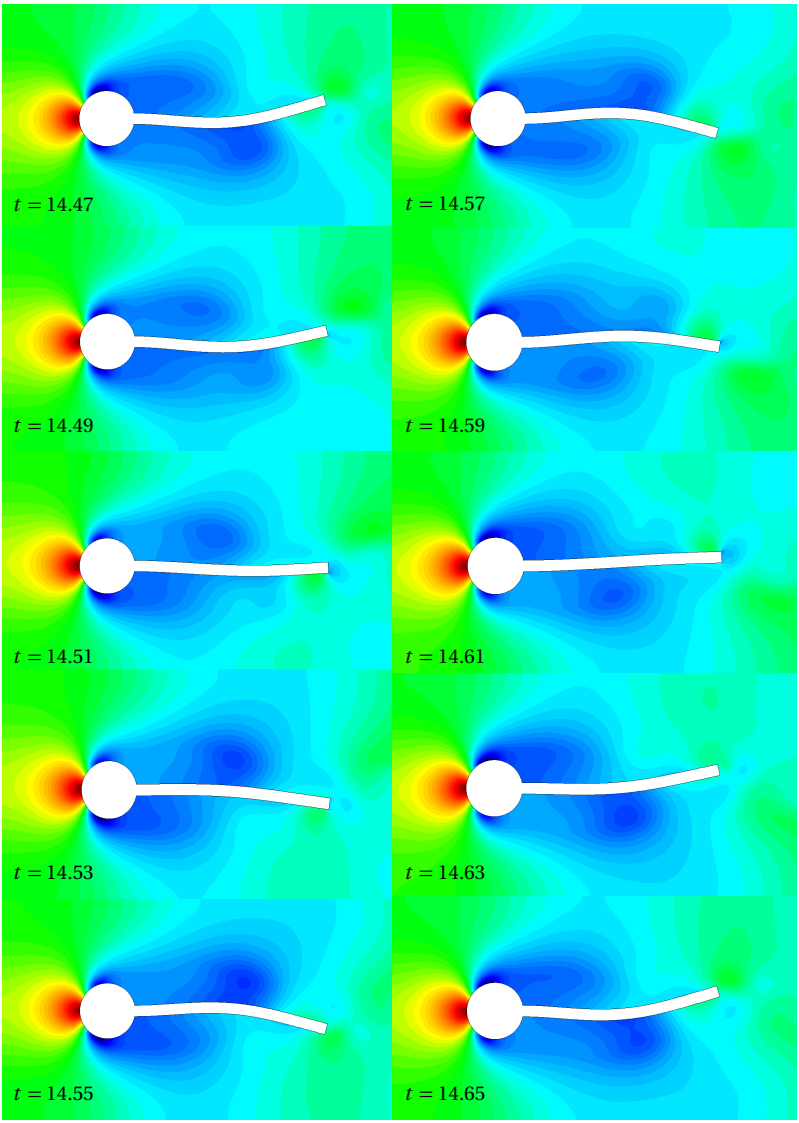

Figure 5.18: FSI3 pressure contours over one period of oscillation.

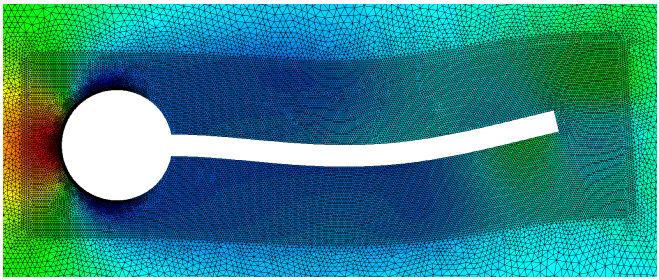

Figure 5.19: FSI3 mesh deformation at $t = 14.67$.

Mesh (Δt)	d_{sx} [x 10^{-3}]	d_{sy} [x 10^{-3}]
1 (0.001)	-2.67 ± 2.51 [11.0]	1.41 ± 34.26 [5.5]
2 (0.001)	-2.67 ± 2.51 [11.0]	1.41 ± 34.30 [5.5]
2 (0.0005)	-2.67 ± 2.51 [11.0]	1.41 ± 34.29 [5.5]
Ref. [113]	-2.69 ± 2.53 [10.9]	1.48 ± 34.38 [5.3]

Table 5.9: Tip displacement for FSI3.

Mesh (Δt)	Drag	Lift
1 (0.001)	465.7 ± 24.17 [11.1]	2.08 ± 157.74 [5.3]
2 (0.001)	465.7 ± 24.00 [11.1]	2.68 ± 155.47 [5.5]
2 (0.0005)	465.7 ± 23.97 [11.2]	2.20 ± 155.26 [5.5]
Ref. [113]	457.3 ± 22.66 [10.9]	2.22 ± 149.78 [5.3]

Table 5.10: Forces on cylinder and flag for FSI3.

Tip displacement of the flexible flag and the lift and drag forces acting on the cylinder and flag are shown in figure 5.20. A quantitative comparison of the results is made with the reference values in tables 5.9 and 5.10. The relative differences between the reference and mesh 2 ($\Delta t = 0.001$) are 0.7% ± 0.8% [0.9%] for the x-displacement, 5.0% ± 0.2% [3.8%] for the y-displacement, 1.8% ± 5.9% [1.8%] for the drag and 20.7% ± 3.8% [3.6%] for the lift.

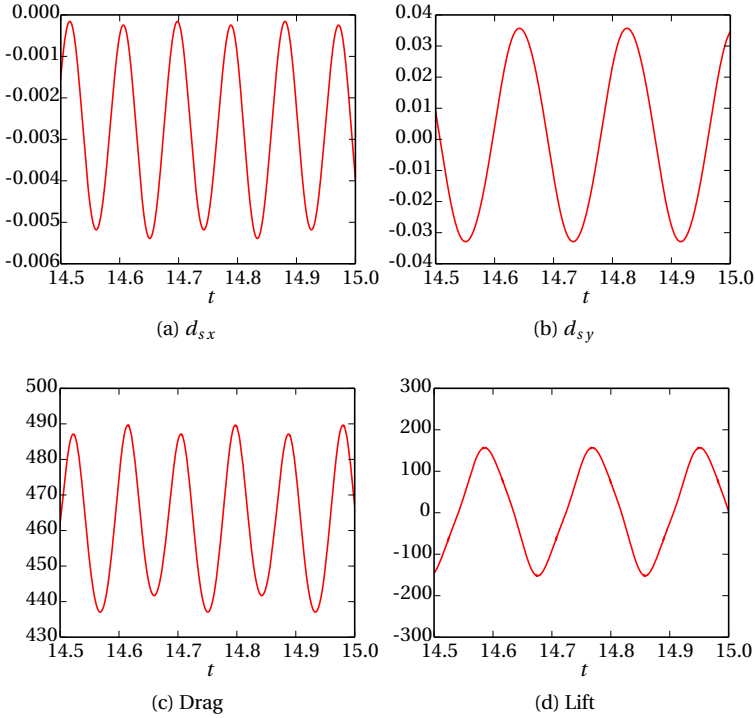

(a) d_{sx} (b) d_{sy}

(c) Drag (d) Lift

Figure 5.20: FSI3 tip displacement and forces acting on the cylinder and flag for mesh 2.

The average number of coupling iterations required at each time step for the interface compressibility algorithm is given in table 5.11.

5.6 Summary

The coupled FSI solver was verified using a combination of analytical and fully nonlinear benchmark problems. Numerical analysis and experiments based on a linear model problem both confirm the second-order accuracy of the interface motion in time for the mixed time discretization based on

Mesh (Δt)	FSI Iterations
1 (0.001)	7.6
2 (0.001)	7.6
2 (0.0005)	7.5

Table 5.11: Average number of FSI coupling iterations for FSI3.

the BDF2 and generalized-α schemes for the fluid and structure, respectively.

For the fractional-step algorithm, the stable range of added-mass ratios of the staggered algorithm in [31] may be increased by performing a small number of pressure corrections (figure 5.12). In the numerical experiments of this chapter, $N_{corr} = 4$ was sufficient to recover the stability of the monolithic solver. The accuracy of the interface motion appeared relatively insensitive to the number of pressure corrections.

For large added-mass ratios, small values of the coupling parameter β_{SC} are required to ensure the stability of the staggered algorithm. This leads to larger errors in the interface motion, which are reduced by decreasing the time step size (figure 5.13). Within this range, it may be more efficient to switch to the iterative coupling technique with interface compressibility and a second-order predictor for which the number of coupling iterations remains relatively constant over a range of moderate to high added-mass ratios (figure 5.9).

Chapter 6

Aeroelastic Simulation

PTSCs are long slender structures, which rotate about their pitching axis in order to capture the direct radiation from the sun over the course of a day. Any deviation from the tracking position due to wind-induced vibrations can lead to a loss of efficiency. Therefore, it is important to obtain an accurate assessment of the wind-induced response for regular operating conditions as well as for ultimate design wind loads. The assessment of wind effects during regular operating conditions requires an analysis of the response for various pitch angles and wind speeds as well as a clear understanding of the various excitation mechanisms involved.

When determining whether aeroelastic effects should be considered, it is useful to review other works involving geometrically similar structures. Specifically, dish-shaped structures such as radio telescopes and paraboloidal solar collectors are mentioned in the literature [64, 77, 89]. These structures may be prone to stall flutter, an aeroelastic instability caused by the synchronization of large-scale vortex shedding from the leading edge with the rotational vibration of the structure. Therefore, the conditions under which stall flutter of a PTSC may occur should be determined.

In this chapter, computational FSI is used to study the wind-excited aeroelastic response of a PTSC. At the time this study was performed, the literature on wind loads for PTSCs was limited to wind tunnel and CFD studies of rigid models[1]. Therefore, this chapter aims at identifying aeroelastic effects, which were not considered in previous studies, by combining the wind load simulation model validated in chapter 4 with the staggered FSI algorithm of [31] discussed in chapter 5. By modeling FSI, the additional physics due to feedback effects of the structural vibration on the wind loads, which the rigid models neglect, are included.

In section 6.1, we discuss the section model used to investigate the aeroelastic response. A dimensional analysis is performed in section 6.2, and the significance of several dimensionless groups is reviewed. The equation of motion for the section model is given in section 6.3, and the one-way and two-way simulations, used to distinguish between self-excited vibrations and the dynamic response due purely to wind buffeting, are explained in section 6.4. Section 6.5 discusses the choice of problem parameters used for this study. Statistics of the simulated full-scale ABL are given in section 6.6, and the effect of varying the pitch angle is investigated in section 6.7. The pitch angles showing significant self-excited vibrations are studied in detail in sections 6.8 and 6.9, and the underlying excitation mechanisms are identified. For comparison, the results of a purely resonant response are provided in section 6.10. Finally, the effect of varying the reduced velocity is investigated in section 6.11. This includes a comparison of the onset of self-excited vibrations detected from the FSI simulations with a study of the aerodynamic damping obtained from controlled oscillation simulations.

Part of the work presented in this chapter has been published in [8]. It is included here with permission from the publisher.

6.1 Section Model

Before selecting a model, it is important to clearly define the purpose of the study. A detailed structural model of a specific collector design at a particular location in an array may be expected to provide the most realistic estimate of the response for that particular configuration. This choice leads

[1] In the case of the wind tunnel, rigid refers to the fact that the model is sufficiently stiff so that the measured loads are not affected by structural vibration.

to a large number of design parameters whose influences on the quantity of interest may be indistinguishable from one another. Moreover, it results in relatively expensive computational models and generally makes a systematic variation of different design parameters infeasible. Without any further understanding of the underlying excitation mechanisms, such studies may be inconclusive as to whether or not motion-induced excitations are relevant in the design of PTSCs or how the response may change with changes in design variables. If, on the other hand, the aim of the study is to identify the underlying excitation mechanisms that are relevant to the response of PTSCs and which design variables affect their behavior, then studying a baseline model corresponding to a specific excitation mechanism may provide more insight. The latter approach is taken in this study.

PTSCs are constructed as a sequence of modules connected in series along a common pitching axis. The pitch angle of the collector is controlled by a mechanical drive with the applied torque transmitted from one module to the next through connector plates. The torsional eigenfrequencies depend on both the module design and the number of modules connected in series. Torsional stall flutter is characterized as the mutual interaction of a single torsional degree of freedom with vortex shedding from the leading edge of the bluff body. For elastic structures, the lowest torsional eigenfrequency is most critical. Therefore, it is desirable to characterize the structural behavior in terms of a single mass and stiffness parameter corresponding to the first torsional eigenfrequency and investigate the aeroelastic behavior in terms of these parameters.

One possibility is to choose an existing collector design and perform model order reduction based on the first torsional eigenmode. This has the advantage that the mode of vibration is more accurately modeled over the length of the chosen collector. The drawbacks are that the computational cost of LES increases significantly when the entire collector is modeled and the accuracy gained may only be valid for the chosen design. Hence, such a reduced order model may be better suited for a subsequent investigation of a design specific case.

Another possibility is to model a section of the collector that includes the properties most critical to torsional stall flutter: the geometric cross section and the mass, damping and stiffness parameters of the first torsional eigenfrequency. This is referred to as a section model and has proven to be useful in the established field of long-span bridge aerodynamics [95]. As the length of a single module is typically much smaller than the length

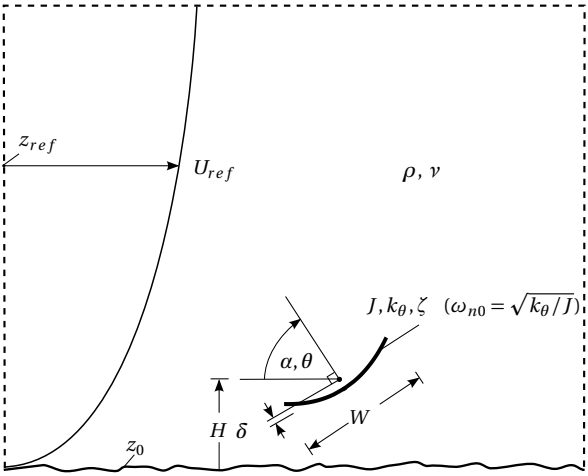

Figure 6.1: Aeroelastic model parameters.

of the collector, the single module is chosen as a representative section model for the entire collector.

6.2 Dimensional Analysis

The parameters of the section model are depicted in figure 6.1. An ABL flow based on the Kaimal spectra is chosen as the approach flow with mean velocity U_{ref} at the reference height z_{ref} and the roughness height z_0. The description of the trough geometry and orientation includes the aperture W, the length of the module L, the height of the pitching axis H, the offset from the pitching axis to the mirror's vertex δ and the pitch angle α. The mirror geometry is the full-scale equivalent of the model in figure 4.1. The elastic center is located at the center of gravity, which coincides with the pitching axis. The angle of deformation around the pitching axis is denoted by θ, and the moment of inertia, mechanical damping ratio and torsional stiffness are denoted by J, ζ and k_θ, respectively.

Assuming geometric similarity and omitting discretization parameters, the response is a function of the variables U_{ref}, z_{ref}, z_0, α, W, ρ, ν, J, ζ,

k_θ. The dimensional matrix is written as

$$\begin{array}{c} \\ M \\ L \\ T \end{array} \begin{array}{c} \begin{array}{cccccccccc} U_{ref} & z_{ref} & z_0 & W & L & \delta & \rho & \nu & J & k_\theta \end{array} \\ \begin{bmatrix} 0 & 0 & 0 & 0 & 0 & 0 & 1 & 0 & 1 & 1 \\ 1 & 1 & 1 & 1 & 1 & 1 & -3 & 2 & 2 & 2 \\ -1 & 0 & 0 & 0 & 0 & 0 & 0 & -1 & 0 & -2 \end{bmatrix} \end{array} \tag{6.1}$$

with α and ζ omitted since they are already in dimensionless form. A reduced set of dimensionless variables of the form

$$\pi_i = U_{ref}^{\alpha_{i1}} z_{ref}^{\alpha_{i2}} z_0^{\alpha_{i3}} W^{\alpha_{i4}} L^{\alpha_{i5}} \delta^{\alpha_{i6}} \rho^{\alpha_{i7}} \nu^{\alpha_{i8}} J^{\alpha_{i9}} k_\theta^{\alpha_{i10}} \tag{6.2}$$

is constructed according to the Buckingham-π theorem by constructing a basis for the null space of matrix (6.1):

$$\begin{aligned}
\boldsymbol{\alpha}_1 &= [\ 1,\ 0,\ 0,\ 1,\ 0,\ 0,\ 0, -1,\ 0,\ 0]^T, \\
\boldsymbol{\alpha}_2 &= [\ 0,\ 0,\ 0,\ 4,\ 1,\ 0,\ 1,\ 0, -1,\ 0]^T, \\
\boldsymbol{\alpha}_3 &= [\ 1,\ 0,\ 0, -1,\ 0,\ 0,\ 0,\ 0,\ 0.5, -0.5]^T, \\
\boldsymbol{\alpha}_4 &= [\ 0,\ 1,\ 0, -1,\ 0,\ 0,\ 0,\ 0,\ 0,\ 0]^T, \\
\boldsymbol{\alpha}_5 &= [\ 0,\ 0,\ 1, -1,\ 0,\ 0,\ 0,\ 0,\ 0,\ 0]^T, \\
\boldsymbol{\alpha}_6 &= [\ 0,\ 0,\ 0, -1,\ 1,\ 0,\ 0,\ 0,\ 0,\ 0]^T, \\
\boldsymbol{\alpha}_7 &= [\ 0,\ 0,\ 0, -1,\ 0,\ 1,\ 0,\ 0,\ 0,\ 0]^T.
\end{aligned}$$

The final set of dimensionless parameters is

$$\begin{aligned}
&\pi_1 = U_{ref} W/\nu, && \pi_2 = \rho L W^4/J, && \pi_3 = U_{ref}/\omega_{n0} W, \\
&\pi_4 = z_{ref}/W, && \pi_5 = z_0/W, && \pi_6 = L/W, \\
&\pi_7 = \delta/W, && \pi_8 = \zeta, && \pi_9 = \alpha.
\end{aligned}$$

Here π_1 is the usual Reynolds number $Re = U_{ref} W/\nu$. π_2 is a form of added-mass ratio and is denoted by[2] $m_r = \rho L W^4/J$. π_3 is often referred to as the reduced velocity. It describes the ratio between fluid and structure frequencies. The definition of reduced velocity used in this work is $U_r = U_{ref}/W f_{n0}$ with f_{n0} the natural frequency of the structure in cycles

[2]Here m_r is used instead of α_{fs}, since m_r does not necessarily satisfy the relation (5.25).

per second ($\omega_{n0} = 2\pi f_{n0}$). The simulated ABL is described by π_4 and π_5. π_4 relates the length scales in the ABL to the model size, and π_5 describes the turbulence intensity. π_6 and π_7 are geometric parameters. Their values are fixed based on the chosen geometry and are not considered further in this study. Finally, π_8 and π_9 are used to denote the two initially dimensionless parameters ζ and α, respectively. For aeroelastic studies, it is common to present the mechanical damping ratio in combination with the mass ratio in the form of a Scruton number, which is defined here as $Sc = 4\pi J\zeta/\rho LW^4 = 4\pi\zeta/m_r$. This eliminates one of the dimensionless parameters, but it is less general than the above presentation. Therefore, we discuss ζ and m_r separately.

6.3 Equation of Motion

The equation of motion for the section model is given by

$$\theta_{,tt} + 2\zeta\omega_{n0}\theta_{,t} + \omega_{n0}^2\theta = \frac{1}{J}M \tag{6.3}$$

and can be transformed into the dimensionless form

$$\theta'' + \frac{4\pi\zeta}{U_r}\theta' + \frac{4\pi^2}{U_r^2}\theta = \frac{1}{2}m_r C_M \tag{6.4}$$

with moment coefficient

$$C_M(t) = \frac{M(t)}{\frac{1}{2}\rho U_{ref}^2 LW^2} \tag{6.5}$$

and non-dimensional form of derivative $(\cdot)' = W(\cdot)_{,t}/U_{ref}$.

6.4 One-Way and Two-Way Coupling

For the solution of the FSI problem, equation (6.3) must be coupled with the solution of the fluid problem. The coupled FSI simulation is computed using the staggered algorithm discussed in chapter 5 and is referred to as a two-way coupled simulation due to the coupling of both moment and rotation.

As the primary aim of this study is to determine the extent to which feedback effects of the collector motion affect the wind loads, it is useful to compare the two-way coupled simulation with a simulation in which the moment computed from a CFD simulation with a fixed domain boundary is applied to the structure (i.e., the boundary of the fluid domain is not updated with the rotation of the collector). We refer to this approach as one-way coupling since it only implies coupling of the moment.

The one-way coupled solution is obtained by performing an additional CFD simulation with a fixed boundary. The computed time-series of the moment acting on the collector is then explicitly applied to the right-hand side of equation (6.3). One-way coupling is sufficient for simulating mechanical resonance, but it is not capable of capturing aeroelastic effects such as torsional stall flutter. Therefore, by performing an additional one-way coupled simulation, one can determine the extent to which the motion of the boundary affects the response.

One-way and two-way coupled approaches are depicted in figure 6.2.

6.5 Design of Experiment

By considering an appropriate section model and performing dimensional analysis in section 6.2, the number of variables is reduced to a set of 9 dimensionless parameters. Since evaluating the response at each combination of these parameters requires a separate time-resolved simulation, it is not feasible to explore the entire space of dimensionless parameters. Therefore, the purpose of this section is to discuss the choice of parameters used in this study.

The Reynolds number is an important parameter for aerodynamic loads of some bluff bodies with moving separation points. A classical example is the aerodynamic loading on a circular cylinder [2, 121]. Bluff bodies with fixed separation points such as rectangular cylinders are normally less sensitive at high Reynolds numbers. The effect of changes in Reynolds number on the aerodynamic load coefficients of PTSCs has been assessed in wind tunnel studies (see, e.g., [47, 86]) and is not expected to be significant. Based on this conclusion, the Reynolds number is fixed in this study with a value of $Re = 3.3 \times 10^6$.

The added-mass parameter m_r is similar to the added mass discussed in chapter 5. Because of the low density of air, the shift in eigenfrequency

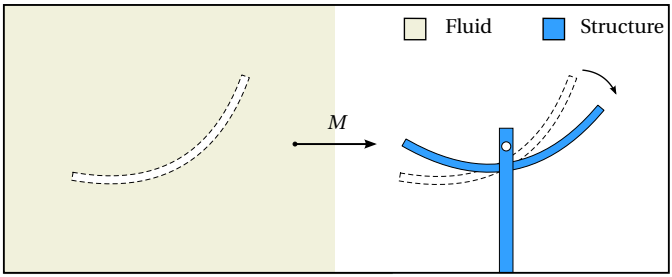

(a) One-way coupling

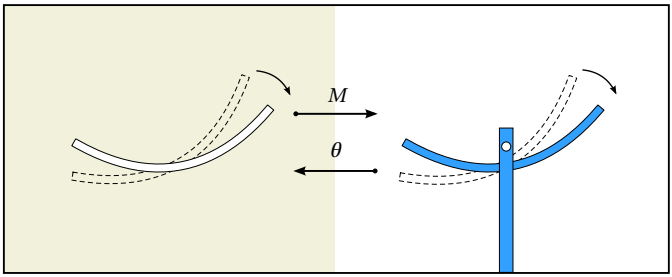

(b) Two-way coupling

Figure 6.2: One-way and two-way simulations.

due to added mass is expected to be small. This was confirmed by a numerical simulation. The collector was allowed to oscillate in quiescent air with a maximum tip displacement of 1 mm, and the period of oscillation was compared with that of the collector in a vacuum. The added mass of air resulted in a decrease in the eigenfrequency by approximately 5%. Therefore, m_r is fixed throughout this study. Its value is chosen based on the EuroTrough design [69].

The ABL parameters π_4 and π_5 affect the length scale of the turbulent eddies and the turbulence intensity according to the synthetic wind field simulation model discussed in chapter 2. The correlation length of pressure over the surface of the structure increases with the turbulence length scale. This follows from the observation that a gust with a spatial extent much smaller than the size of the structure results in smaller aerodynamic loads than a gust that is much larger than the structure. In the frequency domain,

the dependence of aerodynamic loads on the size of turbulent eddies relative to the characteristic dimension of the structure is often expressed in terms of an aerodynamic admittance function, which has a value of 1 at low frequencies and decreases to 0 at high frequencies. Due to the truncated length of the section model, the size of wind gusts relative to the length of the collector cannot be modeled. This is expected to lead to a conservative estimate of the response since the surface pressures are more correlated on the shorter model. In this study, the length scale of the simulated ABL is fixed and is of a similar magnitude to the length scales found in natural wind. The turbulence intensity affects the relative magnitude of the velocity fluctuations. Larger turbulence intensities result in larger peak velocities, which may influence the onset of self-excited vibrations. This effect is discussed in section 6.11. The turbulence intensity is fixed in this study and is chosen based on homogeneous, grass-covered, open country terrain [119]. The turbulence statistics of the simulated ABL are presented in the following section.

The mechanical damping parameter represents the contributions to damping from the material of the structure, the joints and the foundation. The total damping is a combination of the mechanical damping and the aerodynamic damping, which results from the transfer of energy between the fluid and the structure by work. A positive aerodynamic damping indicates a net transfer of energy from the structure to the fluid while a negative aerodynamic damping indicates the transfer from the fluid to the structure. The onset of self-excited vibrations may be considered as the point where the negative aerodynamic damping balances the positive mechanical damping such that any further decrease in aerodynamic damping results in a growing amplitude of vibration. For a linear problem, oscillations grow unbounded when the total damping is negative. Due to the nonlinear nature of stall flutter, the aerodynamic damping depends on the amplitude. Therefore, the oscillations grow until a new equilibrium of finite amplitude is reached for which the net damping is again zero. For structures susceptible to stall flutter, the aerodynamic damping is positive for low reduced velocities and transitions to negative values at higher reduced velocities. The aerodynamic damping of the section model is estimated in section 6.11.1 and transitions from 0 to -10% over a relatively small range of reduced velocities. Because mechanical damping is typically within the range of 2-5%, its value is not expected to have a significant effect on the onset of stall flutter. Therefore, its value is fixed at

Roughness height	z_0	0.02 m
Mirror aperture	W	5 m
Mirror length	L	7.92 m
Pitching axis height	H	2.84 m
Pitching axis offset	δ	0.2 m
Reference height	z_{ref}	10 m
Damping ratio	ζ	0.05
Reynolds number	Re	3.3×10^6
Mass ratio	m_r	1.1

Table 6.1: Constant model parameters.

5% throughout this study.

The reduced velocity and pitch angle have a strong influence on the aeroelastic response. On the one hand, the pitch angle determines the position of the separation point with respect to the bluff body. Stall flutter depends on the interaction of the vortex shedding process, which originates at the separation point, and the portion of the bluff body located downstream from the separation point. Moreover, the onset of self-excited vibrations coincides with a critical reduced velocity, denoted by $U_{r,cr}$. Above $U_{r,cr}$, the amplitude of oscillation grows as the aerodynamic damping decreases with increasing reduced velocity. Both variations in reduced velocity and pitch angle are investigated in this study. First, the reduced velocity is fixed to $U_r = 3.5$ and the pitch angles $\alpha = -30^o, 0^o, 30^o, 60^o, 90^o, 120^o, 150^o, 180^o$ and 210^o are investigated. For a maximum operating wind speed of 22 m/s [105] and aperture of 5 m, a reduced velocity of 3.5 corresponds to a torsional eigenfrequency of 1.26 Hz. Upon identifying the pitch angles for which self-excited vibrations are observed, the effect of varying reduced velocity for the unstable pitch angle configurations is considered.

The remaining geometric parameters π_6 and π_7 are fixed throughout the study.

The set of fixed parameters used in this study is summarized in table 6.1. The reduced velocity is varied by fixing the reference wind speed to $U_{ref} = 9.7$ m/s and varying the torsional eigenfrequency in the range $0.5 \leq f_{n0} \leq 1$ by controlling the stiffness. The wind speed 9.7 m/s was determined

from a preliminary study such that the maximum rotation does not exceed 15^o.

The statistics reported in this study are computed over a time interval of approximately $5000W/U_{ref}$. The time step size chosen for the study resulted in a temporal resolution of $U_{ref}\Delta t/h \approx 0.3$ for the fluid problem with h the mesh size in the volume around the collector and $f_{n0}\Delta t \approx 0.015$ for the structure problem (approximately 67 time steps per period of oscillation).

6.6 Full-Scale Wind Simulation

In order to measure the statistics of the simulated ABL, a full-scale empty channel simulation is performed with the settings in the previous section. Velocity time series are measured at the position of the structure at 21 points evenly distributed from the ground until the reference height. The resulting mean velocity and turbulence intensity profiles are shown together with the one-sided power spectrum and autocorrelation at the reference height in figure 6.3. Above the frequency $f \approx 0.6U_{ref}/W$, the power spectrum begins to decay rapidly due to the dissipation of turbulent eddies with length scales close to the mesh size. The largest structural eigenfrequency considered in this study is $f_{n0} \approx 0.51U_{ref}/W$. Therefore, the artificial decay in spectral density at higher frequencies is not expected to have a significant impact on the analysis.

6.7 Effect of Varying Pitch Angle

One-way and two-way simulations are performed for 9 pitch angle configurations at the reduced velocity $U_r = 3.5$. Mean, maximum, minimum and RMS statistics of the moment coefficient and rotation are plotted in figures 6.4 and 6.5. The mean results are unaffected by the choice of one-way or two-way simulation. This confirms past wind tunnel studies since the mean aerodynamic coefficients reported in those studies are based on rigid models. In both one-way and two-way simulations, the most significant vibrations occur for pitch angles 60^o, 90^o and 120^o. Unlike the mean statistics, the maximum, minimum and RMS results are considerably different for the pitch angles 60^o and 90^o. At these pitch angles, the results of the two-way simulation are larger in magnitude than the one-way results.

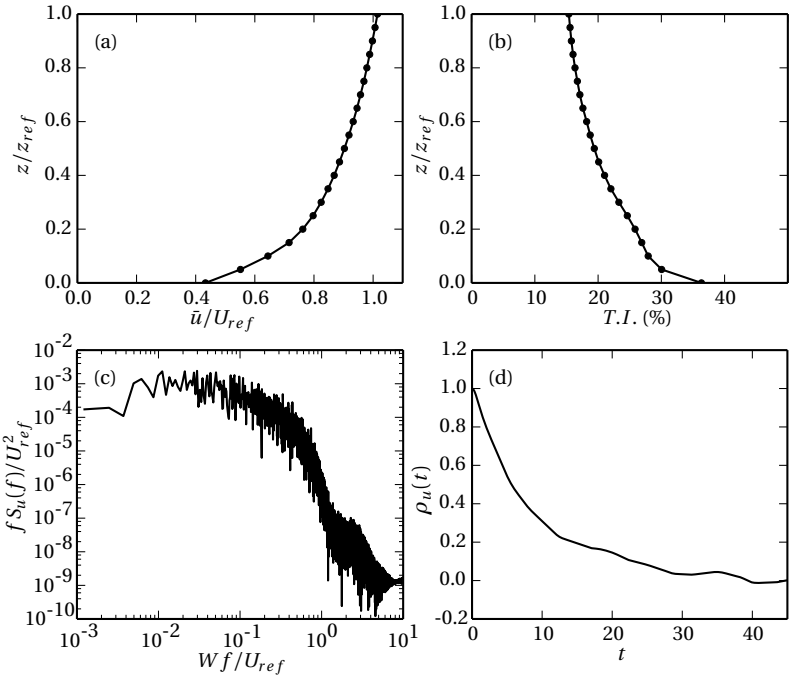

Figure 6.3: (a) Mean velocity, (b) turbulence intensity, (c) power spectrum and (d) autocorrelation of the simulated wind.

The differences are largest for 90° with the RMS rotation of the two-way simulation approximately double the value of the one-way simulation. In contrast, the results at 120° are nearly identical.

For the one-way simulation, the RMS rotation for 90° is similar to the value at 120° despite the RMS moment coefficient being smaller by a factor of approximately one half. This suggests considerably greater resonance at 90° compared to 120°. A similar argument may be made for 60°. Given that the same wind is used for all simulations, the excitation frequencies contained in the wind fluctuations are the same for all simulations. Thus, the results suggest that an additional excitation due to bluff-body aerodynamics contributes to the resonant response at 60° and 90°. The larger

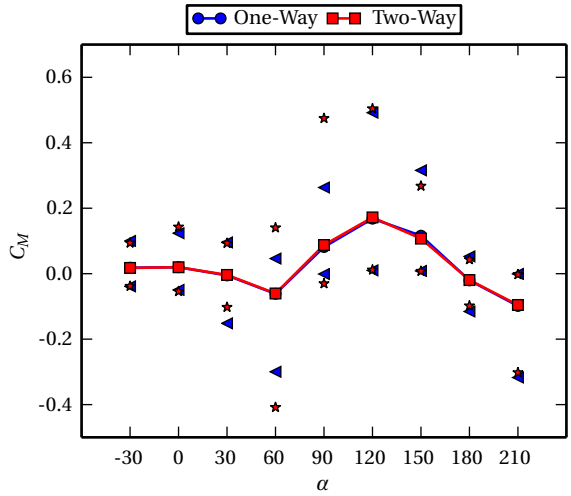

(a) Mean, maximum and miminum

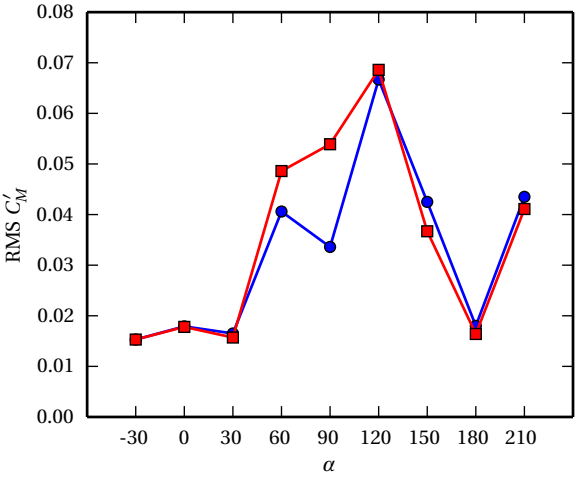

(b) Root mean square

Figure 6.4: Aeroelastic moment coefficient statistics for $U_r = 3.5$.

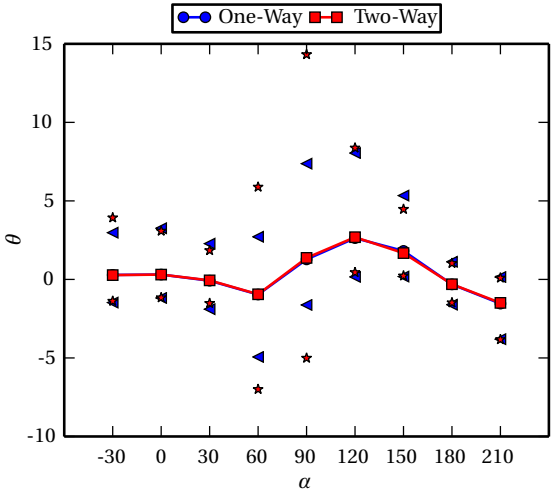

(a) Mean, maximum and miminum

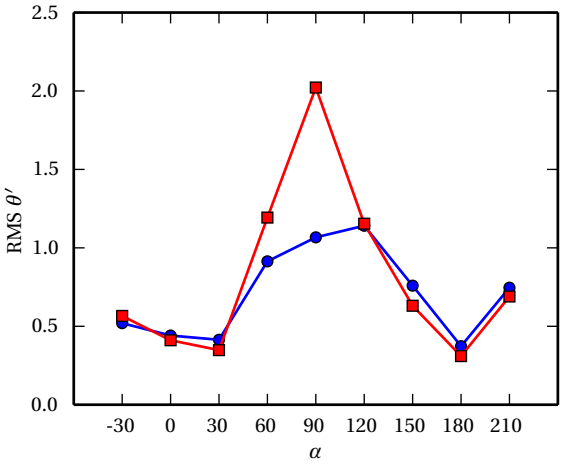

(b) Root mean square

Figure 6.5: Aeroelastic rotation statistics for $U_r = 3.5$.

Figure 6.6: Pitch angles 60°, 90° and 120°.

RMS rotation observed for two-way coupling indicates that the response is not purely a resonant response and that self-excited vibrations due to feedback effects of the structural vibration on the bluff-body aerodynamics also occur.

The additional excitation due to bluff-body aerodynamics may be attributed to flow instabilities such as vortex shedding originating from the separation point. Such instabilities originating from the structure may be sensitive to structural vibrations. Thus, it is not surprising that self-excited vibrations coincide with the pitch angles at which significant resonant excitation due to bluff-body aerodynamics are observed. The extent to which vortex shedding contributes to aerodynamic loading and self-excited vibrations depends on the size and shape of the afterbody[3]. The importance of the size and shape of the afterbody as a precondition for self-excited vibrations is discussed by [82]. The pitch angle configurations for 60°, 90° and 120° are plotted in figure 6.6. The afterbody at 90° is exposed to vortex shedding from the leading edge until near the trailing edge. In contrast, the afterbody at 60° continues downstream nearly horizontally before curving upwards and away from the vortex shedding. At 120° the afterbody moves away from the separation point more rapidly. Thus, both the 60° and 90° cases satisfy the precondition for self-excited vibrations in the sense that their afterbodies may be in close proximity to vortices shed from the leading edge while the 120° case is less likely to fulfill this requirement, resulting in a weaker interaction between the structural vibration and the aerodynamic loading.

[3]Here, afterbody refers to the part of the structure downstream from the leading separation point.

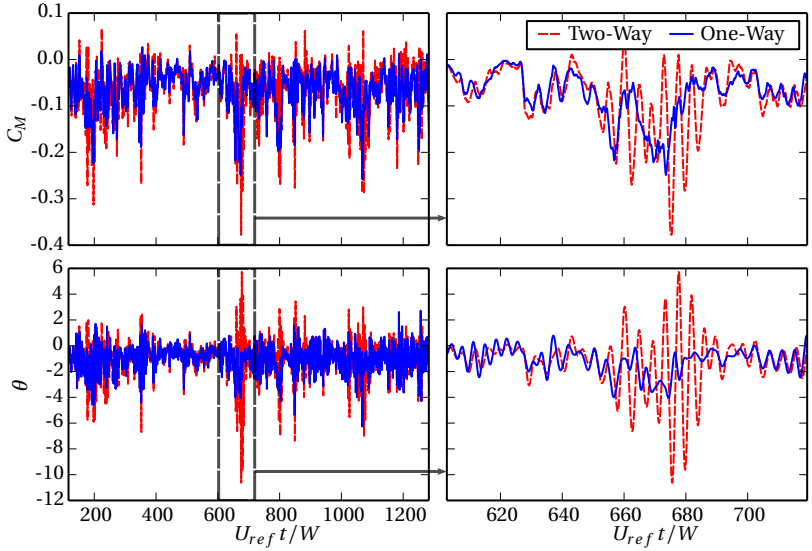

Figure 6.7: Moment coefficient and rotation time series for 60°.

6.8 Wind-Excited Response for Pitch Angle $\alpha = 60^o$

6.8.1 Comparison of One-Way and Two-Way Solutions

The wind-excited response at $\alpha = 60^o$ is investigated for both one-way and two-way coupling in this section. Time series of moment coefficient and rotation are plotted over a time interval of $1250\,W/U_{ref}$ in the left side of figure 6.7. The time interval shown is one quarter of the total time used to compute the statistics in the previous section. Therefore, the peaks may be smaller than the values reported in figures 6.4 and 6.5. Although both one-way and two-way simulations are performed separately, the time-varying inlet boundary condition used to simulate the ABL is identical for both simulations, which allows for a direct comparison of the two time series.

The largest differences between the two simulations appear near the peaks. The right side of figure 6.7 shows the interval around the largest peak. The absence of a dominant high frequency component in the one-way moment coefficient indicates that the fluctuations are primarily caused

by turbulence buffeting. Initially, the two-way moment coefficient closely follows that of the one-way simulation. As the one-way moment coefficient drops, the two-way moment coefficient appears to synchronize with the rotation and oscillates close to the natural frequency of the structure. In this interval, both the moment coefficient and rotation reach amplitudes significantly larger than the one-way results.

The drop in the one-way moment coefficient is attributed to an increase in wind speed around the section model. This can be reasoned by imagining a simplified model of the wind gust whose length scale is much larger than that of the section model. This way the spatial variation of the gust may be neglected and its aerodynamic admittance can be taken as equal to 1. The dependence of the moment on the wind fluctuation is estimated from the linearization

$$\begin{aligned} M(t) &\approx \frac{1}{2}\rho LW^2(U_{ref} + u'(t))^2 \bar{C}_M \\ &\approx \frac{1}{2}\rho LW^2 U_{ref}^2 \bar{C}_M + \rho LW^2 U_{ref}\, u'(t)\bar{C}_M. \end{aligned} \tag{6.6}$$

The corresponding moment coefficient is

$$C_M(t) \approx \bar{C}_M + 2\frac{u'(t)}{U_{ref}}\bar{C}_M. \tag{6.7}$$

For 60^o the mean moment coefficient is $\bar{C}_M = -0.062$. As a result, an increase in the fluctuation u' causes a decrease in the moment coefficient C_M. Thus, the drop in the moment coefficient of the one-way simulation and the appearance of self-excited vibrations in the two-way simulation coincide with an increase in wind speed around the structure.

This is confirmed by plotting velocity contours on isosurfaces of Q-criterion for 4 equally spaced instants in time around the peak in figure 6.8. The wind speed is initially low at $U_{ref}\, t/W = 641.7$. After the onset of the peak, the wind speed has increased noticeably and a regular vortex shedding pattern can be seen at $U_{ref}\, t/W = 659.0$. During synchronization, a vortex appears to shed from the upper edge as the mirror reaches its minimum angle of rotation with the period of vortex shedding coinciding with the period of oscillation. The velocity remains high at $U_{ref}\, t/W = 672.6$ before dropping of at the end ($U_{ref}\, t/W = 690.1$).

The one-sided power spectra of the moment coefficient and rotation are plotted in figure 6.9. The clearly visible peak in spectral density of the two-

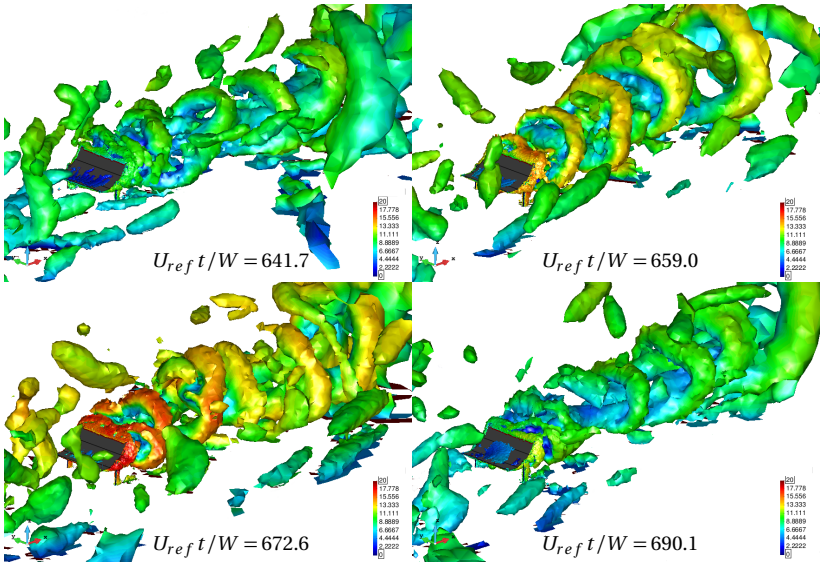

Figure 6.8: Isosurfaces of Q-criterion (Q=0.2) colored by velocity for the two-way simulation at $\alpha = 60^o$.

way moment coefficient, which drops off abruptly at higher frequencies, indicates stronger vortex shedding compared to the one-way simulation. The dominant shedding frequency coincides with the frequency of vibration with $f_{sh} = f_o = 0.21 U_{ref}/W$. This is considerably lower than the frequency of oscillation for the one-way simulation with $f_o \approx f_n = 0.29 U_{ref}/W$.

6.8.2 Synchronization Process

A detailed investigation of the flow field over two cycles of self-excited vibrations is presented in order to better understand the synchronization process at $\alpha = 60^o$. Figure 6.10 shows the pressure distribution around the center section according to the phase of rotation. On the downstroke, the rotation decreases and the leading edge of the collector drops. As this happens, the suction on the back side of the leading edge increases (figure 6.10g), indicating the formation of a vortex. The vortex sheds shortly after the minimum rotation is reached (6.10b), and the region of high suction

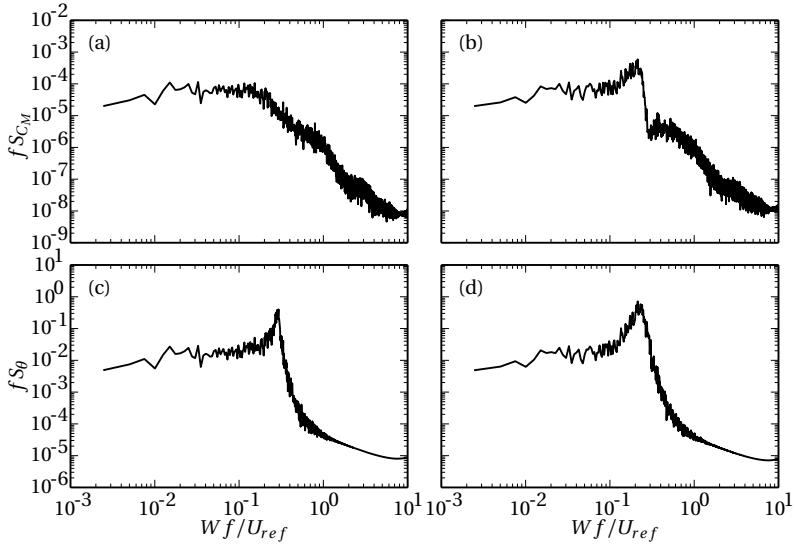

Figure 6.9: Power spectra for (a) one-way moment coefficient, (b) two-way moment coefficient, (c) one-way rotation and (d) two-way rotation for $\alpha = 60^o$.

moves downstream along the back of the mirror. As the vortex continues downstream, the suction on the back of the collector decreases (figure 6.10d) until a new vortex begins to form and the cycle repeats itself.

The sychronization process is visualized for one cycle of vibration beginning with the maximum rotation in figures 6.11 and 6.12. Figure 6.11 shows the vortex shedding from the upper edge of the collector during the downstroke. The vortex core appears as a small circular region of negative pressure behind the upper edge shortly before the collector reaches its minimum rotation in figure 6.12. At the same time, a second vortex core is developing at the lower edge. As the collector begins the upstroke, the vortex sheds from the lower edge and moves along the back of the collector while the vortex shed from the upper edge expands and convects downstream. Midway through the upstroke, the two regions of negative pressure combine as they continue to expand and convect downstream.

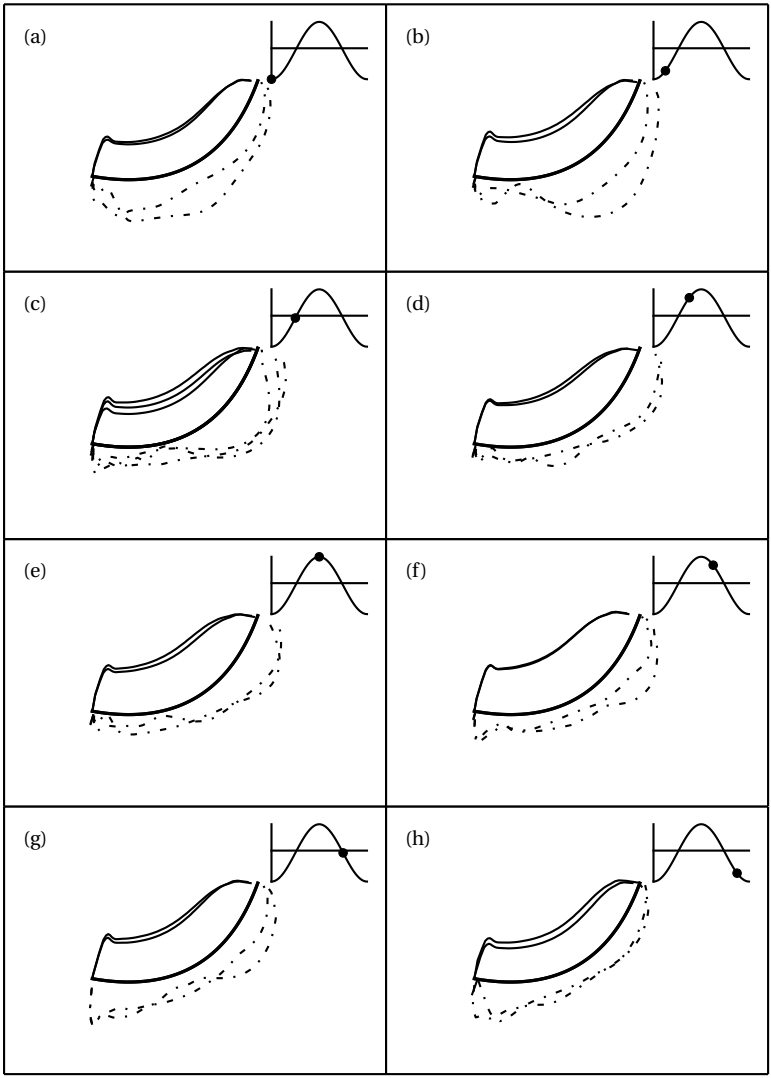

Figure 6.10: Synchronization of pressure with rotation for two-way coupled simulation. Positive pressure (solid) and negative pressure (dash-dot) are plotted for approximately 2 cycles of motion for $\alpha = 60^o$.

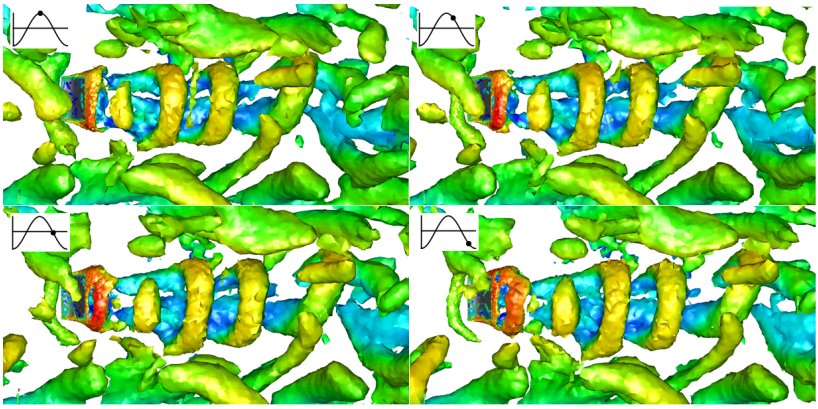

Figure 6.11: Isosurfaces of Q-criterion (Q=0.2) colored by velocity during synchronization of vortex shedding with collector rotation for $\alpha = 60^o$.

6.9 Wind-Excited Response for Pitch Angle $\alpha = 90^o$

6.9.1 Comparison of One-Way and Two-Way Solutions

Time series of moment coefficient and rotation for 90^o are plotted in figure 6.13. In contrast to 60^o, the mean moment coefficient for 90^o is positive. Substituting the mean moment coefficient $\bar{C}_M = 0.082$ in equation (6.7), it is reasoned that an increase in wind speed causes an increase in the moment coefficient. On the right side of figure 6.13, the two moment coefficients are initially similar and diverge as the one-way moment coefficient increases, indicating an increase in wind speed. The oscillations in the one-way moment coefficient have a smaller amplitude and occur over a range of frequencies close to the natural frequency of the structure. These oscillations are attributed to vortex shedding from the leading edge of the collector and explain the large resonant excitation observed for 90^o in section 6.7. The feedback of the collector vibration close to the shedding frequency causes the two-way moment coefficient to synchronize with the rotation and both undergo smooth large-amplitude oscillations at a single frequency. The synchronization ends as the wind speed decreases and the one-way moment coefficient drops.

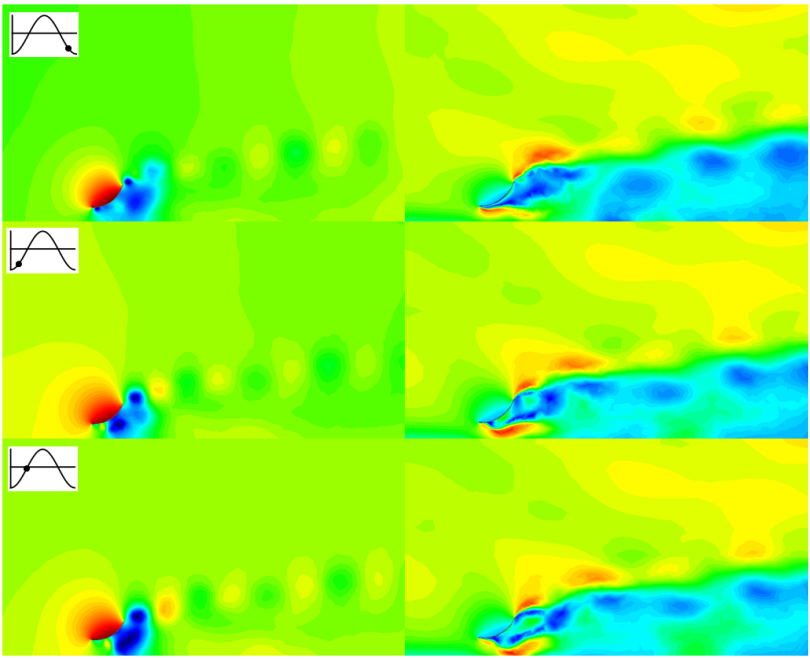

Figure 6.12: Pressure and velocity contours during synchronization of vortex shedding with collector rotation for $\alpha = 60^o$.

Power spectra of the moment coefficient and rotation are shown in figure 6.14. The fluctuations of the one-way moment coefficient appear as a clearly visible broad-banded peak around $Wf_{sh}/U_{ref} = 0.23$ in figure 6.14a. From figure 6.14c, the dominant frequency of oscillation for the one-way simulation occurs at $Wf_o/U_{ref} = 0.29$ and corresponds to the natural frequency of the structure. In the two-way simulation, the peaks in spectral density for moment coefficient and oscillation occur at the same frequency $Wf_{sh}/U_{ref} = Wf_o/U_{ref} = 0.24$. The peak in spectral density is also significantly higher for both moment coefficient and rotation with the spectral density of the moment coefficient dropping off sharply at higher frequencies. The high spectral density of the moment coefficient is also concentrated around a narrow band of frequencies.

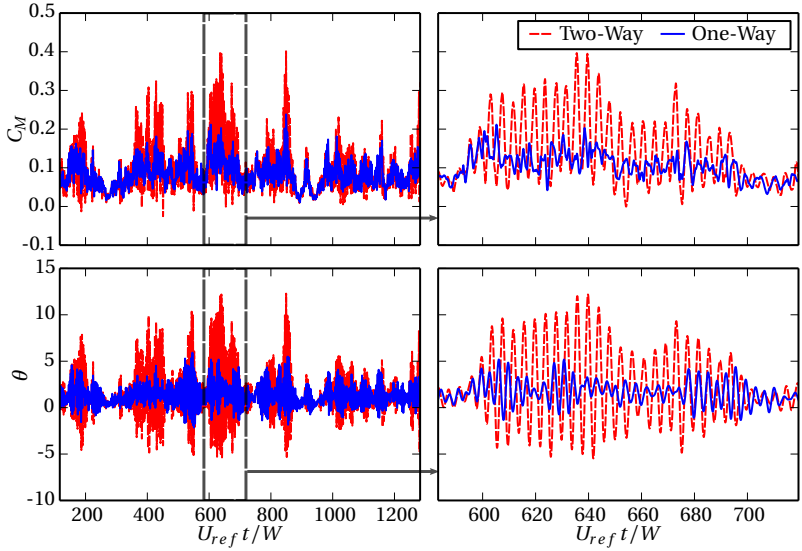

Figure 6.13: Moment coefficient and rotation time series for $\alpha = 90^o$.

6.9.2 Synchronization Process

The synchronization of the vortex shedding process with the rotation is further investigated by plotting the pressure distributions according to phase of rotation around the center section of the model. Since the self-excited vibrations are sustained over a longer time interval than for $\alpha = 60^o$, the pressure distributions are included over 5 cycles of vibration in figure 6.15. In the case $\alpha = 60^o$, the primary contribution of vortex shedding to the aerodynamic loading occurs as a vortex forms on the lower side of the leading edge during the downstroke (decreasing θ). Figure 6.15, shows a region of high suction developing on the upper side of the leading edge during the upstroke (increasing θ). This is due to the fact that the shear layer originating from the leading edge is located on the lower side for $\alpha = 60^o$ and on the upper side for $\alpha = 90^o$. In both cases, the vortex sheds as the leading edge is close to the maximum deformation. After the vortex sheds, the high suction on the upper side is replaced by a region of small positive pressure. Thus, less energy is transferred back to the fluid

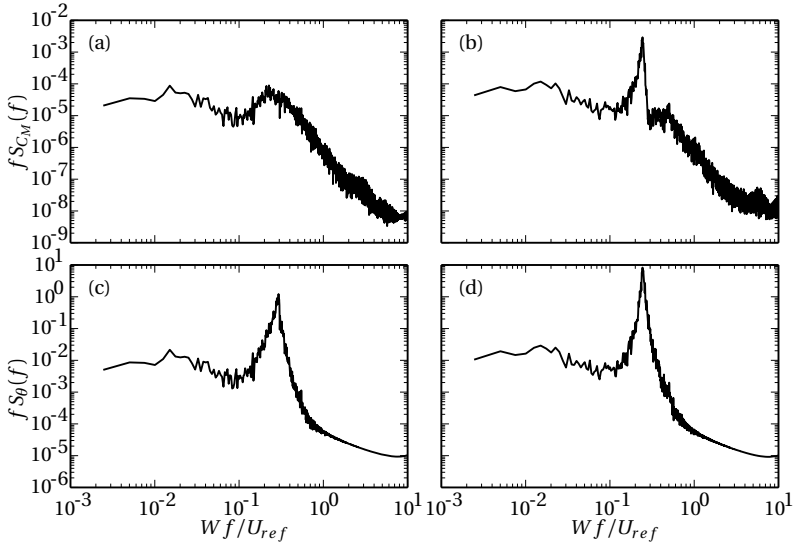

Figure 6.14: Power spectra for (a) one-way moment coefficient, (b) two-way moment coefficient, (c) one-way rotation and (d) two-way rotation for $\alpha = 90^o$.

on the downstroke. In addition to the periodic vortex shedding on the upper side, the stagnation pressure on the lower side of the leading edge increases as the edge tilts upward and the adjacent suction bubble shifts from the mirror's center towards the trailing edge. On the downstroke, the stagnation pressure drops and the suction bubble moves back towards the center of the collector.

6.10 Wind-Excited Response for Pitch Angle $\alpha = 120^o$

As a comparison, the time series of the moment coefficient and rotation are plotted for $\alpha = 120^o$ in figure 6.16. On the right side, the same gust that was observed on the right side of figure 6.13 causes an increase in the moment coefficient. Despite the increase in wind speed, the one-way and two-way results remain in close agreement, and the feedback effects of the collector motion on the aerodynamic loads are negligible.

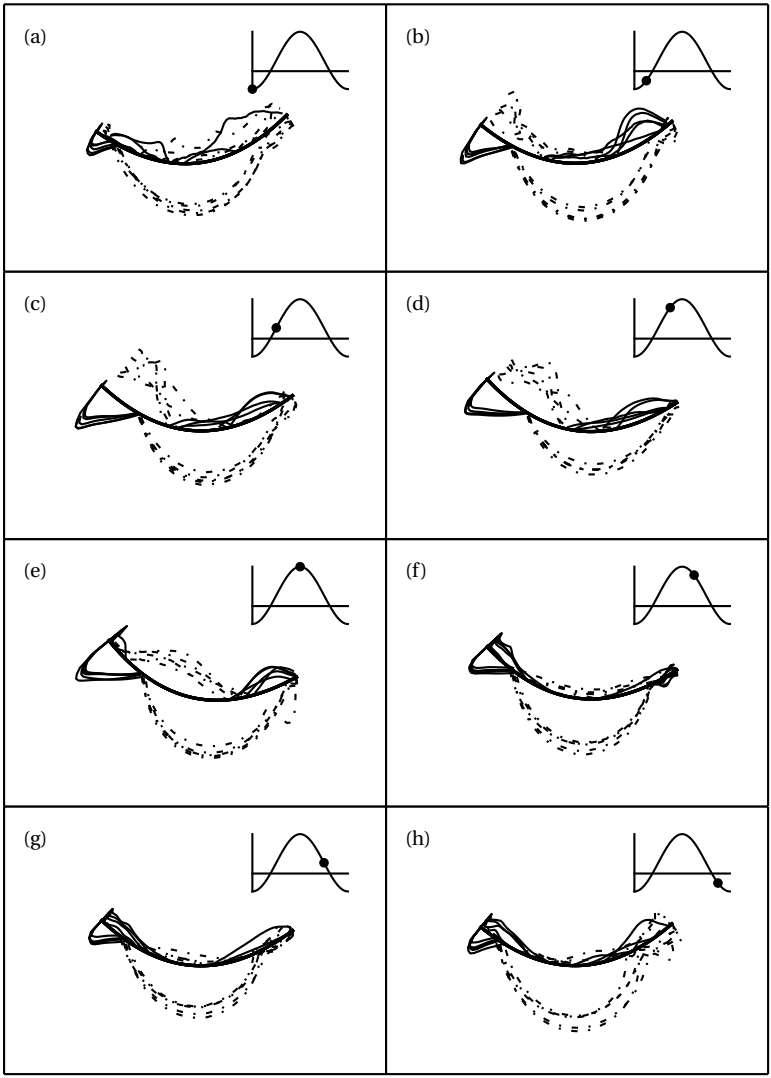

Figure 6.15: Synchronization of pressure with rotation for two-way simulation. Positive pressure (solid) and negative pressure (dash-dot) are plotted for approximately 5 cycles of motion for $\alpha = 90^o$.

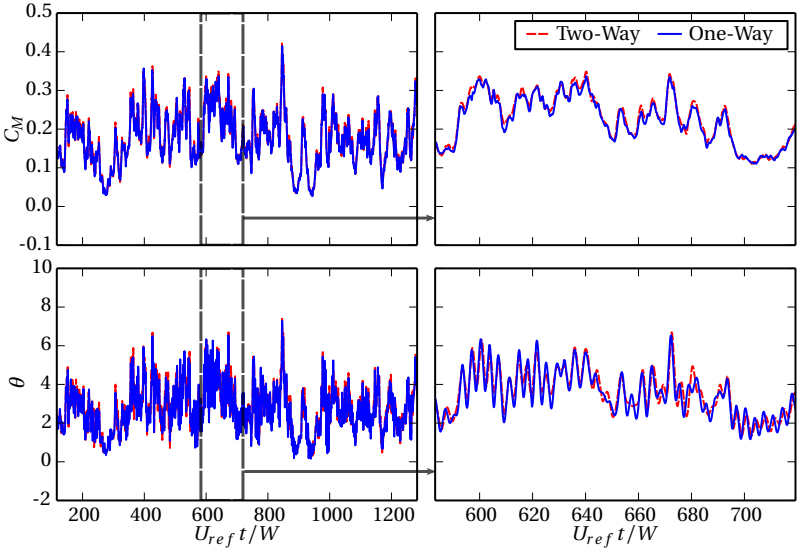

Figure 6.16: Moment coefficient and rotation time series for $\alpha = 120^o$.

6.11 Effect of Varying Reduced Velocity

The effect of varying reduced velocity is investigated for the pitch angle $\alpha = 90^o$. Changes in reduced velocity may reflect changes in the torsional eigenfrequency due to different structural models or changes in wind speed. For fixed structural parameters, the reduced velocity increases with increasing mean wind speed. The shedding frequency scales with the mean wind speed according to the Strouhal number. The Strouhal number used in this study is defined as $St = W f_{sh}/U_{ref}$ and is based on the mean wind speed at a height of 10 m. For low wind speeds, the shedding frequency is much lower than the torsional eigenfrequency and synchronization of the vortex shedding with collector oscillation is not observed. As the wind speed increases and the shedding frequency approaches the frequency of vibration, the vortex shedding may synchronize with the frequency of vibration, resulting in self-excited vibrations. As discussed above, the threshold at which the onset of self-excited vibrations occurs is herein

referred to as the critical reduced velocity and is denoted by $U_{r,cr}$. The goal of this section is to estimate $U_{r,cr}$ for the pitch angle $\alpha = 90^o$ and to investigate the structural response as the reduced velocity transitions from pre-critical to post-critical reduced velocities.

Two approaches exist for investigating self-excited vibrations. The first approach, referred to as controlled-oscillation simulation, forces the structure to oscillate with a prescribed frequency and amplitude[4]. A time series of the moment is measured and is used to calculate the aerodynamic damping corresponding to the prescribed frequency and amplitude. Controlled-oscillation simulations have the advantage that an FSI simulation is not required. However, the aerodynamic damping can only be determined in terms of the frequency of oscillation. As shown above, the frequency of oscillation changes if the coupled FSI simulation is performed. This shift in frequency cannot be directly determined from the controlled-oscillation simulation. Another limitation of controlled oscillation is that a smooth approach flow is generally required in order to calculate the aerodynamic damping. Thus, the dependence of self-excited vibrations on turbulence buffeting cannot be directly studied.

The second approach is referred to as free vibration simulation and corresponds to the two-way coupled simulation described above. Using this approach, the frequency of oscillation can be determined for a given structural eigenfrequency. Free vibration simulations are normally computed for smooth approach flows, but the response can also be computed for realistic turbulent conditions. In the case that the response is simulated in an ABL flow, the computational cost increases due to the need to compute for longer simulation times in order to evaluate statistics. Moreover, the response changes with changes in roughness conditions.

Both approaches are considered in this study. First, a controlled-oscillation simulation is performed for a smooth approach flow to determine the aerodynamic damping ratio. The aerodynamic damping ratio is combined with the distribution of wind velocities computed for the given roughness in order to estimate the onset of self-excited vibrations. The estimated critical reduced velocity is then compared with the two-way coupled simulation of the collector in the simulated ABL, and the variation in moment coefficient and rotation statistics as a function of reduced velocity is determined. Fi-

[4]A more detailed description can be found in [77].

nally, the behavior of the shedding and oscillation frequencies for one-way and two-way coupled simulations are compared.

6.11.1 Controlled-Oscillation Simulation

The rotation of the controlled-oscillation simulation is prescribed as

$$\theta(t) = \theta_0 \sin(2\pi f_o t) \tag{6.8}$$

with amplitude $\theta_0 = 4^o$ and frequency of oscillation $f_o = 0.55\,\text{Hz}$. The inlet boundary condition is prescribed by the roughness in table 6.1 and the velocity at the reference height according to the logarithmic profile. The time-varying fluctuations from the simulated ABL are not included, resulting in a smooth approach flow. The time series of the moment is measured for varying approach velocities and the fitting parameters A, B and $\bar{M}$ are computed for the function

$$M(t) = -A\dot{\theta} - B\theta + \bar{M}. \tag{6.9}$$

The aerodynamic damping ratio is computed as the component of the moment signal in phase with the angular velocity as

$$\zeta_a = \frac{A}{2J\omega_{n0}}. \tag{6.10}$$

Equation (6.10) depends on the natural frequency $\omega_{n0} = 2\pi f_{n0}$. The natural frequency corresponding to the prescribed frequency of oscillation is estimated from the results of the two-way simulation in section 6.9. Its value is fixed to $f_{n0}/f_o = 1.2$ here. Based on this, the aerodynamic damping is plotted as a function of u/Wf_{n0} in figure 6.17. Here, u is the velocity of the approach flow at the reference height. The onset of self-excited vibrations occurs when the total damping drops below zero. The stability threshold of the aerodynamic damping corresponds to the negative value of the structural damping and is included in figure 6.17. The unstable region begins when the velocity of the approach flow exceeds the critical velocity $u_{cr} = 4.1Wf_{n0}$. This estimate is valid for a smooth approach flow but changes when turbulent fluctuations are considered.

In order to estimate the effect of the turbulent fluctuations on the onset of self-excited vibrations, we consider the distribution of instantaneous

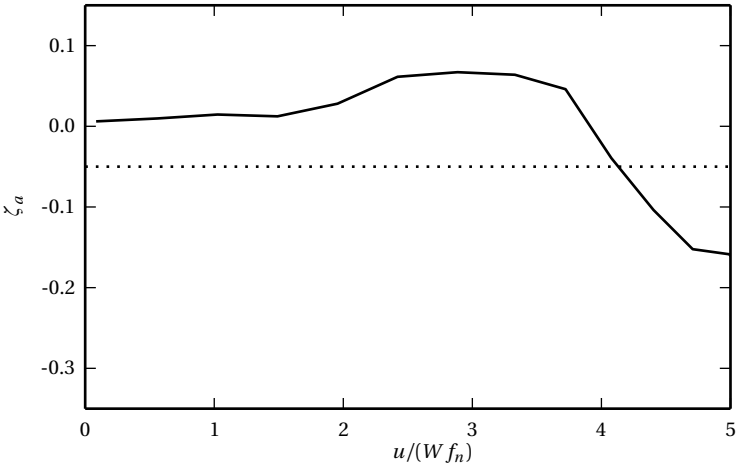

Figure 6.17: Aerodynamic damping ratio (ζ_a) measured from forced vibration simulation with amplitude $\theta_0 = 4^o$ at $\alpha = 90^o$. The stability threshold ($-\zeta$) is plotted as a dotted line.

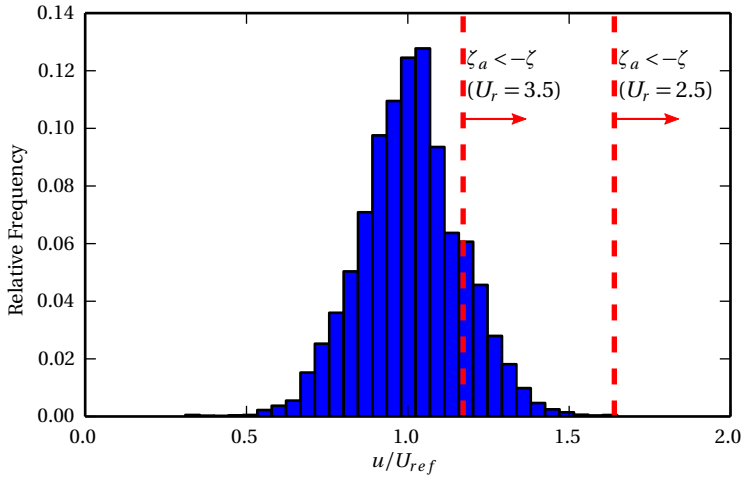

Figure 6.18: Normalized wind distribution.

velocities normalized by the mean velocity at the reference height in figure 6.18. Dividing u_{cr} by U_{ref} results in a normalized critical velocity, which depends on the reduced velocity $u_{cr}/U_{ref} = 4.1/U_r$. Thus, velocities satisfying $u/U_{ref} < 4.1/U_r$ are not expected to cause self-excited vibrations. The maximum normalized velocity in figure 6.18 is $u/U_{ref} \approx 1.64$. From this, the onset of self-excited vibrations in the ABL flow is estimated to be $U_r = 2.5$. As the reduced velocity increases above this threshold, the distribution of velocities crosses into the unstable region and an increase in self-excited vibration is observed. This is the case for the reduced velocity $U_r = 3.5$ of section 6.7. As seen from figure 6.18, the mean wind velocity U_{ref} lies in the stable region, but wind gusts result in instantaneous velocities, which are higher than the stability threshold.

6.11.2 Two-Way Coupled Analysis

The one-way and two-way responses of the collector in the simulated ABL are computed for reduced velocities in the range $2.1 < U_r < 3.5$. The reduced velocity is controlled by using the torsional stiffness to adjust the eigenfrequency. For the one-way simulation, the boundary of the fluid domain does not deform with the collector motion. As a result, the CFD simulation is independent of the structural eigenfrequency and only one simulation is performed. The structural response is then computed from the time series of the moment for 5 equally spaced reduced velocities. In the case of two-way coupling, FSI simulations are performed for each of the 5 reduced velocities.

Maximum and RMS statistics of the moment coefficient and rotation are plotted in figure 6.19. The one-way and two-way statistics are similar for $U_r < 2.4$. At higher reduced velocities, self-excited vibrations become significant and the one-way simulation significantly underestimates the response. The estimate of the critical reduced velocity $U_{r,cr} = 2.5$ from the previous section is in good agreement with the observed response. As the maximum wind speed exceeds the stability threshold, two-way coupled simulations or aeroelastic models are needed to estimate wind loads and the magnitude of the structural response.

Figure 6.20 compares the frequency of oscillation and the shedding frequency of the one-way and two-way simulations for varying reduced velocity. The frequencies are computed from the peaks in spectral densities of the moment coefficient and rotation. For example, the shedding fre-

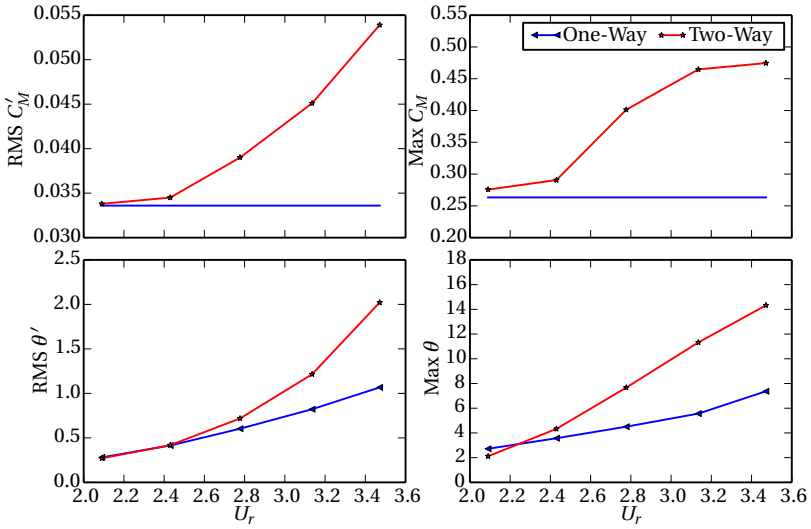

Figure 6.19: Comparison of moment and rotation for varying reduced velocity at $\alpha = 90^o$.

quency of the one-way simulation for $U_r = 3.5$ corresponds to the peak in spectral density in figure 6.14a while the oscillation frequency is obtained from figure 6.14c. The peaks in figures 6.14b and 6.14d give the frequencies for the two-way simulation. The frequency of oscillation for the one-way simulation corresponds to the natural frequency, and hence the corresponding curve in figure 6.20 varies according to $1/U_r$. In contrast, the shedding frequency of the one-way simulation is independent of the natural frequency and remains constant with varying U_r. The frequencies of the two-way simulation lie between these two limits. At low reduced velocities, the shedding frequency and oscillation frequency are different from one another. As the reduced velocity increases, the vortex shedding frequency approaches the eigenfrequency and the two frequencies synchronize in the two-way simulation. At this point self-excited vibrations occur and the response of the two-way simulation becomes larger than that of the one-way simulation. As the eigenfrequency and shedding frequency of the one-way simulation become closer, the frequency of synchronization ap-

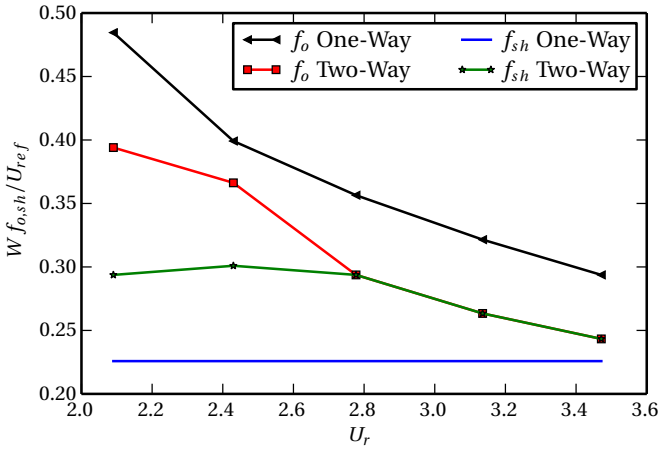

Figure 6.20: Comparison of oscillation and shedding frequencies for varying reduced velocity at $\alpha = 90^o$.

proaches the natural shedding frequency and the amplitude of self-excited vibrations grows.

6.12 Summary

The aeroelastic simulations conducted in this chapter have confirmed that self-excited vibrations may occur at pitch angles for which the collector's afterbody is in close proximity to the vortices shed from the leading edge. At other pitch angles, the response is due to externally-induced excitation and can be simulated without considering FSI effects. The onset of self-excited vibrations in an ABL flow may be estimated from the aerodynamic damping, obtained from a controlled-oscillation simulation, and the largest gust wind speed for the ABL flow considered. An advantage of this approach is that the simulations may be performed independently from the ABL conditions. FSI simulations should be performed if the coupled shedding or oscillation frequency is needed or if the response amplitude should be estimated.

Chapter 7

Conclusions and Outlook

In this thesis work, a modeling and simulation approach for computational wind engineering has been presented and applied for the evaluation of wind loads on a parabolic trough solar collector. It was shown that the numerical approach is capable of producing estimates of mean, RMS and peak wind loads, which are in close agreement with measurements from a boundary layer wind tunnel experiment.

The numerical model was extended to include fluid-structure interaction and several coupling algorithms were evaluated using a recently proposed analytical benchmark problem. It was found that the combination of the generalized-α method for the structural time discretization and the second-order backward difference formula for the fluid time discretization results in a second-order accurate scheme for the coupled fluid-structure problem. The inclusion of FSI effects increases the modeling complexity significantly since the efficiency and stability of the various coupling algorithms are problem dependent. Among the algorithms considered in this work, the staggered algorithm proposed by [31] and the iterative algorithm using artificial compressibility as presented by [85] performed the best. Due to its low added mass, the staggered algorithm was used to study the aeroelastic response of the solar collector in this thesis.

The aeroelastic study was used to investigate possible feedback effects of the structural motion on aerodynamic loads caused by the vortex shedding process. It was shown that significant self-excited vibrations can occur when the afterbody of the collector is exposed to vortex shedding from the leading edge. Self-excitation occurs as a result of increased suction near the leading edge due to the formation of a vortex, which synchronizes with the vibration of the collector about its pitching axis. The synchronization process was found to be consistent with stall flutter as discussed in the context of existing knowledge found in the literature. The prediction of self-excited vibrations using FSI simulations was confirmed by a more classical technique based on controlled-oscillation simulations. The utility of the latter approach was illustrated through a comparison with the current state-of-the-art analysis. Its main advantages are that it does not require the use of FSI algorithms and that the aerodynamic damping, obtained from a simulation in a smooth flow, can be reused with various wind velocity distributions to estimate the onset of self-excited vibrations. Its limitations include the modeling simplifications due to the requirement of a smooth approach flow, which may become more decisive for larger structures, and its inability to predict the response of the collector.

Concerning the parabolic trough solar collector, a number of effects were not considered in this work. These include the influence of fences and surrounding collectors on the response. Such investigations may be part of future studies. It is also recommended to verify the results of the aeroelastic study with wind tunnel tests. Besides reducing the exposure of the collectors to the wind, it is recommended to investigate the use of passive flow control devices around the edges of the collector (see, e.g., [20]) for mitigation of vortex-induced resonance and self-excited vibrations.

Recommendations for research into numerical models for computational wind engineering include the reduction of simulation times and proper validation studies. One topic, which was not covered in this work, is the performance optimization of simulation codes to exploit recent computer architectures for high performance computing. Efforts in this direction are important for improving the efficiency of simulation codes and thus expanding the range of applications for computational wind engineering. Another interesting research topic is the development of effective local mesh error indicators for LES to accelerate mesh refinement studies.

Appendix A

Calculation of Statistics

The definitions of the statistics for a time series of wind velocity $\{u^n\}_{n=0}^{N-1}$ as presented in this work are given below.

A.1 Mean Velocity

Mean velocity is computed as

$$\bar{u} = \sum_{k=0}^{N-1} \frac{u^k}{N}. \tag{A.1}$$

A.2 Standard Deviation

Standard deviation is computed as

$$\sigma_u = \sqrt{\sum_{k=0}^{N-1} \frac{|u'^k|^2}{N}}. \tag{A.2}$$

A.3 Spectral Density

The discrete Fourier transform of the velocity fluctuation is computed as

$$\hat{u}'^m = \frac{\sqrt{2T}}{N} \sum_{k=0}^{N-1} u'^k \exp\left(-\frac{2\pi i m k}{N}\right), \quad m = 0 \ldots N-1. \tag{A.3}$$

The spectral density at the frequency $f = m/T$ is given by

$$S_u^m = \overline{|\hat{u}'^m|^2} \tag{A.4}$$

and is estimated by dividing the total time series into subintervals (usually 8 or 16), computing (A.3) on each subinterval and averaging the results.

A.4 Autocorrelation

The autocorrelation at the time delay $\tau = m\Delta t$ is either computed as

$$\rho_u^m = \frac{1}{\sigma_u^2 N} \sum_{k=0}^{N-1} u'^k u'^{m+k \bmod N} \tag{A.5}$$

or, using the convolution theorem, as

$$\rho_u^m = \frac{1}{2T\sigma_u^2} \sum_{k=0}^{N-1} S_u^k \exp\left(\frac{2\pi i m k}{N}\right). \tag{A.6}$$

Appendix B

Viscous Fluid-Structure Interaction Model Problem

The derivation in this section for the viscous FSI problem (5.32) is based on the solution of the small-amplitude surface wave presented in [84].

The solution is decomposed into an inviscid solution, denoted by $\boldsymbol{u}_p, p_p$, and a viscous correction, denoted by $\boldsymbol{u}_v, p_v$, according to

$$\boldsymbol{u} = \boldsymbol{u}_p + \boldsymbol{u}_v, \tag{B.1}$$

$$p = p_p + p_v. \tag{B.2}$$

The solution of the inviscid part is determined in section 5.1.1. The viscous correction is required to satisfy

$$\frac{\partial \boldsymbol{u}_v}{\partial t} + \frac{1}{\rho_f}\nabla p_v - \nu_f \nabla^2 \boldsymbol{u}_v = 0 \quad \text{in } \Omega_f \times (0,T), \tag{B.3}$$

$$\nabla \cdot \boldsymbol{u}_v = 0 \quad \text{in } \Omega_f \times (0,T), \tag{B.4}$$

$$v_v = 0 \quad \text{on } y = 0. \tag{B.5}$$

Taking the curl of (B.3) results in

$$\frac{\partial \omega_z}{\partial t} = \nu_f \nabla^2 \omega_z \tag{B.6}$$

with $\omega_z = \frac{\partial v_v}{\partial x} - \frac{\partial u_v}{\partial y}$ the vorticity[1]. Moreover, equation (B.4) is satisfied by choosing

$$u_v = -\frac{\partial \psi_z}{\partial y}, \quad v_v = \frac{\partial \psi_z}{\partial x} \tag{B.7}$$

with ψ_z the stream function. At the boundary $y = 0$, the zero shear condition[2] together with (5.8) results in the vorticity boundary condition

$$\omega_z(x,0,t) = 2\frac{\partial v}{\partial x} = -\frac{4\pi}{L} a_{,t}(t) \sin\left(\frac{2\pi}{L} x\right). \tag{B.8}$$

The vorticity is solved by substituting

$$\omega_z(x,y,t) = \Omega_z(y,t) \sin\left(\frac{2\pi}{L} x\right) \tag{B.9}$$

into (B.6) and (B.8) and imposing $\lim_{y\to-\infty} \omega_z = 0$. The resulting problem is

$$\frac{\partial \Omega_z}{\partial t} = \nu_f \frac{\partial^2 \Omega_z}{\partial y^2} - \left(\frac{2\pi}{L}\right)^2 \nu_f \Omega_z, \tag{B.10}$$

$$\Omega_z(0,t) = -\frac{4\pi}{L} a_{,t}(t), \tag{B.11}$$

$$\lim_{y\to-\infty} \Omega_z = 0. \tag{B.12}$$

For the case of zero initial vorticity, the solution in the Laplace domain is

$$\mathcal{L}[\Omega_z](y,s) = -\frac{4\pi}{L} \mathcal{L}[a_{,t}](s) \exp\left(\left[\frac{4\pi^2}{L^2} + \frac{s}{\nu_f}\right]^{1/2} y\right). \tag{B.13}$$

Defining[3]

$$\mathcal{L}[g](y,s) = -\frac{4\pi}{L} \exp\left(-\left[\frac{4\pi^2 y^2}{L^2} + \frac{y^2}{\nu_f} s\right]^{1/2}\right), \tag{B.14}$$

[1] Here we use the fact that $\nabla \times \boldsymbol{u}_p = \mathbf{0}$.

[2] The zero shear condition, (5.30), is used to simplify the derivation leading to an explicit benchmark solution.

[3] The domain of interest is the lower half-plane $y \le 0$ such that $y = -|y|$.

the inverse Laplace transform of (B.13) is

$$\begin{aligned}\Omega_z(y,t) &= \int_0^t g(y,t-s)a_{,t}(s)ds \\ &= \int_0^t \frac{2\sqrt{\pi}y}{L\sqrt{\nu_f(t-s)^3}}\exp\left(-\frac{4\pi^2\nu_f(t-s)}{L^2}\right) \\ &\qquad \exp\left(\frac{-y^2}{4\nu_f(t-s)}\right)a_{,t}(s)ds. \end{aligned} \tag{B.15}$$

It remains to determine the stream function and thus the viscous part of the fluid solution from the vorticity. Equations (B.7) and (5.8) admit a stream function of the form

$$\psi_z(x,y,t) = \Psi_z(y,t)\sin\left(\frac{2\pi}{L}x\right). \tag{B.16}$$

Substituting (B.9) and (B.16) into the identity

$$\omega_z = \nabla^2\psi_z \tag{B.17}$$

and using (B.5) with (B.7) together with the condition of boundedness as $y \to -\infty$ gives

$$\frac{\partial^2\Psi_z}{\partial y^2} - \frac{4\pi^2}{L^2}\Psi_z = \Omega_z, \tag{B.18}$$

$$\Psi_z(0,t) = 0, \tag{B.19}$$

$$\lim_{y\to-\infty}\Psi_z(y,t) = 0. \tag{B.20}$$

Using the method of variation of parameters, the solution is found to be

$$\begin{aligned}\Psi_z(y,t) = \frac{L}{4\pi}\exp\left(\frac{2\pi}{L}y\right)\left[\int_{-\infty}^{0}\exp\left(\frac{2\pi}{L}s\right)\Omega_z(s,t)ds + \int_0^y \exp\left(-\frac{2\pi}{L}s\right)\Omega_z(s,t)ds\right] \\ -\frac{L}{4\pi}\exp\left(-\frac{2\pi}{L}y\right)\int_{-\infty}^{y}\exp\left(\frac{2\pi}{L}s\right)\Omega_z(s,t)ds. \end{aligned} \tag{B.21}$$

By differentiating (B.21) with respect to time, eliminating $\frac{\partial \Omega_z}{\partial t}$ with (B.10) and integrating by parts, one obtains

$$\frac{\partial \Psi_z}{\partial t}(y,t) = \nu_f \left[\Omega_z(y,t) - \Omega_z(0,t) \exp\left(\frac{2\pi}{L} y\right) \right]. \tag{B.22}$$

Substituting (B.7) into (B.3) and using (B.17), (B.9), (B.16) and (B.22), the viscous part of the pressure p_v must satisfy

$$\frac{\partial p_v}{\partial x} = -\left(\frac{2\pi}{L}\right) \mu_f \Omega_z(0,t) \exp\left(\frac{2\pi}{L} y\right) \sin\left(\frac{2\pi}{L} x\right), \tag{B.23}$$

$$\frac{\partial p_v}{\partial y} = \left(\frac{2\pi}{L}\right) \mu_f \Omega_z(0,t) \exp\left(\frac{2\pi}{L} y\right) \cos\left(\frac{2\pi}{L} x\right). \tag{B.24}$$

Upon solving for the pressure with the condition $\lim_{y \to -\infty} p = 0$, the viscous solution of the fluid problem

$$\begin{aligned} v_v(x,y,t) = \frac{1}{2} \Bigg[& \exp\left(\frac{2\pi}{L} y\right) \int_{-\infty}^{0} \exp\left(\frac{2\pi}{L} s\right) \Omega_z \, ds \\ & + \exp\left(\frac{2\pi}{L} y\right) \int_{0}^{y} \exp\left(-\frac{2\pi}{L} s\right) \Omega_z \, ds \\ & - \exp\left(-\frac{2\pi}{L} y\right) \int_{-\infty}^{y} \exp\left(\frac{2\pi}{L} s\right) \Omega_z \, ds \Bigg] \cos\left(\frac{2\pi}{L} x\right), \end{aligned} \tag{B.25}$$

$$p_v(x,y,t) = \mu_f \Omega_z(0,t) \exp\left(\frac{2\pi}{L} y\right) \cos\left(\frac{2\pi}{L} x\right) \tag{B.26}$$

is combined with the potential solution from (5.19)

$$v_p(x,y,t) = a_{,t} \exp\left(\frac{2\pi}{L} y\right) \cos\left(\frac{2\pi}{L} x\right), \tag{B.27}$$

$$p_p(x,y,t) = -\frac{\rho_f L}{2\pi} a_{,tt} \exp\left(\frac{2\pi}{L} y\right) \cos\left(\frac{2\pi}{L} x\right) \tag{B.28}$$

and substituted into the pressure boundary condition (5.29) to obtain the surface pressure distribution on the fluid-structure interface

$$p_s(x,t) = -\left[\frac{\rho_f L}{2\pi} a_{,tt}(t) - \mu_f \Omega_z(0,t) + \frac{4\pi}{L}\mu_f a_{,t}(t) + \frac{4\pi}{L}\mu_f \int_{-\infty}^{0} \exp\left(\frac{2\pi}{L}s\right)\Omega_z(s,t)\,ds\right]\cos\left(\frac{2\pi}{L}x\right). \tag{B.29}$$

Equation (B.29) is applied to the right-hand side of the membrane problem (5.20) or beam problem (5.27). After substituting (B.11) and rearranging terms, the general form of the initial value problem may be expressed as

$$\hat{d}_{s,tt} + \frac{16\pi^2}{L^2}\frac{\nu_f}{1+\frac{1}{\alpha_{fs}}}\hat{d}_{s,t} + \omega_n^2 \hat{d}_s + \frac{8\pi^2}{L^2}\frac{\nu_f}{1+\frac{1}{\alpha_{fs}}}\int_{-\infty}^{0} \exp\left(\frac{2\pi}{L}s\right)\Omega_z(s,t)\,ds = 0, \tag{B.30}$$

$$\Omega_z(y,t) = \int_0^t \frac{2\sqrt{\pi}y}{L\sqrt{\nu_f(t-s)^3}} \exp\left(-\frac{4\pi^2\nu_f(t-s)}{L^2}\right) \exp\left(\frac{-y^2}{4\nu_f(t-s)}\right)\hat{d}_{s,t}(s)\,ds, \tag{B.31}$$

$$\hat{d}_s(0) = \hat{d}_{s0}, \tag{B.32}$$

$$\hat{d}_{s,t}(0) = \hat{v}_{s0}. \tag{B.33}$$

After substituting (B.31) into (B.30) and interchanging the integrals, the last term on the left-hand side of (B.30) becomes

$$-\frac{16\pi^3}{L^3}\frac{\nu_f}{1+\frac{1}{\alpha_{fs}}}\int_0^t \frac{1}{\sqrt{\pi\nu_f(t-s)^3}}\exp\left(-\frac{4\pi^2}{L^2}\nu_f(t-s)\right) \left(\int_0^\infty y\exp\left(-\frac{y^2}{4\nu_f(t-s)}\right)\exp\left(-\frac{2\pi}{L}y\right)dy\right)\hat{d}_{s,t}(s)\,ds. \tag{B.34}$$

The inner integral in (B.34) may be evaluated using standard Laplace transform techniques. The resulting initial value problem is

$$\hat{d}_{s,tt} + \frac{16\pi^2}{L^2}\frac{\nu_f}{1+\frac{1}{\alpha_{fs}}}\hat{d}_{s,t} + \omega_n^2\hat{d}_s - 4\frac{\nu_f^2}{1+\frac{1}{\alpha_{fs}}}\frac{16\pi^4}{L^4} \cdot \int_0^t \left[\frac{\exp\left(-\frac{4\pi^2}{L^2}\nu_f(t-s)\right)}{\sqrt{\pi\frac{4\pi^2}{L^2}\nu_f(t-s)}} - \operatorname{erfc}\sqrt{\frac{4\pi^2}{L^2}\nu_f(t-s)}\right]\hat{d}_{s,t}\,ds, \tag{B.35}$$

$$\hat{d}_s(0) = \hat{d}_{s0}, \tag{B.36}$$

$$\hat{d}_{s,t}(0) = \hat{v}_{s0}. \tag{B.37}$$

The dimensionless form of (B.35) is given by (5.32) with the dimensionless parameters defined in (5.33).

Bibliography

[1] H. Aboshosha, A. Elshaer, G. Bitsuamlak, and A.E. Damatty. "Consistent inflow turbulence generator for LES evaluation of wind-induced responses for tall buildings." In: *Journal of Wind Engineering and Industrial Aerodynamics* 142 (2015), pp. 198–216. DOI: 10.1016/j.jweia.2015.04.004.

[2] E. Achenbach. "Distribution of local pressure and skin friction around a circular cylinder in cross-flow up to $Re = 5 \times 10^6$." In: *Journal of Fluid Mechanics* 34 (1968), pp. 625–639. DOI: 10.1017/S0022112068002120.

[3] M. Andre. *Extension and Assessment of Kratos Multiphysics for Design Support in Computational Wind Engineering*. Internal Report for Abengoa. 2015.

[4] M. Andre. *WindGen*. https://github.com/msandre/WindGen. 2017.

[5] M. Andre, K.-U. Bletzinger, and R. Wüchner. "A complementary study of analytical and computational fluid-structure interaction." In: *Computational Mechanics* 55 (2015), pp. 345–357. DOI: 10.1007/s00466-014-1104-3.

[6] M. Andre, I. Hanzlicek, R. Wüchner, and K.-U. Bletzinger. "Performance of a weakly coupled fluid-structure interaction solver." In: *Conference Proceedings of the YIC GACM 2015*. Ed. by

S. Elgeti and J.-W. Simon. Publication Server of RWTH Aachen University, 2015.

[7] M. Andre, M. Mier-Torrecilla, and R. Wüchner. “Numerical simulation of wind loads on a parabolic trough solar collector using lattice Boltzmann and finite element methods.” In: *Journal of Wind Engineering and Industrial Aerodynamics* 146 (2015), pp. 185–194. DOI: 10.1016/j.jweia.2015.08.010.

[8] M. Andre, M. Péntek, K.-U. Bletzinger, and R. Wüchner. “Aeroelastic simulation of the wind-excited torsional vibration of a parabolic trough solar collector.” In: *Journal of Wind Engineering and Industrial Aerodynamics* 165 (2017), pp. 67–78. DOI: 10.1016/j.jweia.2017.03.005.

[9] S. Badia, F. Nobile, and C. Vergara. “Fluid-structure partitioned procedures based on Robin transmission conditions.” In: *Journal of Computational Physics* 227 (2008), pp. 7027–7051. DOI: 10.1016/j.jcp.2008.04.006.

[10] J.S. Baggett, J. Jiménez, and A.G. Kravchenko. *Resolution requirements in large-eddy simulations of shear flows*. Annual Research Briefs, Center for Turbulence Research, Stanford. 1997.

[11] F. Baily. “On the correction of a pendulum for the reduction to a vacuum: together with remarks on some anomalies observed in pendulum experiments.” In: *Philosophical Transactions of the Royal Society of London* 122 (1832), pp. 399–492.

[12] E. Balaras, C. Benocci, and U. Piomelli. “Two-layer approximate boundary conditions for large-eddy simulations.” In: *AIAA Journal* 34 (1996), pp. 1111–1119. DOI: 10.2514/3.13200.

[13] F. W. Bessel. *Untersuchungen über die Länge des einfachen Secundenpendels*. Druckerei der Königlichen Akademie der Wissenschaften, Berlin, 1828.

[14] B. Blocken. “50 years of computational wind engineering: past, present and future.” In: *Journal of Wind Engineering and Industrial Aerodynamics* 129 (2014), pp. 69–102. DOI: 10.1016/j.jweia.2014.03.008.

[15] A.J. Bronkhorst, C.A. van Bentum, and C.P.W. Geurts. “Results of a CFD benchmark for wind loads on a high-rise building.” In: *7th European and African Conference on Wind Engineering*. Liège, 2017.

[16] E. Burman and M. A. Fernández. “Stabilization of explicit coupling in fluid-structure interaction involving fluid incompressibility.” In: *Computer Methods in Applied Mechanics and Engineering* 198 (2009), pp. 766–784. DOI: 10.1016/j.cma.2008.10.012.

[17] W. Cabot and P. Moin. “Approximate wall boundary conditions in the large-eddy simulation of high Reynolds number flow.” In: *Flow, Turbulence and Combustion* 63 (2000), pp. 269–291. DOI: 10.1023/A:1009958917113.

[18] P. Causin, J.F. Gerbeau, and F. Nobile. “Added-mass effect in the design of partitioned algorithms for fluid-structure problems.” In: *Computer Methods in Applied Mechanics and Engineering* 194 (2005), pp. 4506–4527. DOI: 10.1016/j.cma.2004.12.005.

[19] D.R. Chapman. “Computational aerodynamics development and outlook.” In: *AIAA Journal* 17 (1979), pp. 1293–1313. DOI: 10.2514/3.61311.

[20] H. Choi, W.-P. Jeon, and J. Kim. “Control of flow over a bluff body.” In: *Annual Review of Fluid Mechanics* 40 (2008), pp. 113–139. DOI: 10.1146/annurev.fluid.39.050905.110149.

[21] J. Chung and G.M. Hulbert. “A time integration algorithm for structural dynamics with improved numerical dissipation: the generalized-α method.” In: *Journal of Applied Mechanics* 60 (1993), pp. 371–375. DOI: 10.1115/1.2900803.

[22] R. Codina. “Pressure stability in fractional step finite element methods for incompressible flows.” In: *Journal of Computational Physics* 170 (2001), pp. 112–140. DOI: 10.1006/jcph.2001.6725.

[23] R. Codina. “Stabilized finite element approximation of transient incompressible flows using orthogonal subscales.” In: *Computer Methods in Applied Mechanics and Engineering* 191 (2002), pp. 4295–4321. DOI: 10.1016/S0045-7825(02)00337-7.

[24] R. Codina and S. Badia. “On some pressure segregation methods of fractional-step type for the finite element approximation of incompressible flow problems.” In: *Computer Methods in Applied Mechanics and Engineering* 195 (2006), pp. 2900–2918. DOI: 10.1016/j.cma.2004.06.048.

[25] A. Collette. *HDF5 for Python*. http://www.h5py.org. 2008.

[26] O. Colomés, S. Badia, R. Codina, and J. Principe. “Assessment of variational multiscale models for the large eddy simulation of turbulent incompressible flows.” In: *Computer Methods in Applied Mechanics and Engineering* 285 (2015), pp. 32–63. DOI: 10.1016/j.cma.2014.10.041.

[27] J. Cotela. “Applications of turbulence modeling in civil engineering.” PhD thesis. Universitat Politècnica de Catalunya, 2016.

[28] P. Dadvand, R. Rossi, and E. Oñate. “An object-oriented environment for developing finite element codes for multi-disciplinary applications.” In: *Archives of Computational Methods in Engineering* 17 (2010), pp. 253–297. DOI: 10.1007/s11831-010-9045-2.

[29] J. Degroote. “On the similarity between Dirichlet-Neumann with interface artificial compressibility and Robin-Neumann schemes for the solution of fluid-structure interaction problems.” In: *Journal of Computational Physics* 230 (2011), pp. 6399–6403. DOI: 10.1016/j.jcp.2011.05.012.

[30] J. Degroote, R. Haelterman, S. Annerel, P. Bruggeman, and J. Vierendeels. “Performance of partitioned procedures in fluid-structure interaction.” In: *Computers and Structures* 88 (2010), pp. 446–457. DOI: 10.1016/j.compstruc.2009.12.006.

[31] W. G. Dettmer and D. Perić. “A new staggered scheme for fluid-structure interaction.” In: *International Journal for Numerical Methods in Engineering* 93 (2013), pp. 1–22. DOI: 10.1002/nme.4370.

[32] S. Dong, G.E. Karniadakis, and C. Chryssostomidis. “A robust and accurate outflow boundary condition for incompressible flow simulations on severely-truncated unbounded domains.” In: *Journal of Computational Physics* 261 (2014), pp. 83–105. DOI: 10.1016/j.jcp.2013.12.042.

[33] F. Dorigatti, C. Scollard, G. Larose, and P.O. Dallaire. “Wind tunnel tests and performance improvement of a conveyor suspension bridge.” In: *7th European and African Conference on Wind Engineering*. Liège, 2017.

[34] A. Elshaer, H. Aboshosha, G. Bitsuamlak, A.E. Damatty, and A. Dagnew. “LES evaluation of wind-induced responses for an isolated and a surrounded tall building.” In: *Engineering Structures* 115 (2016), pp. 179–195. DOI: 10.1016/j.engstruct.2016.02.026.

[35] EN 1991-1-4: Eurocode 1. *Actions on structures - Part 1-4: General actions - Wind actions*. 2005.

[36] A. Ern and J.-L. Guermond. *Theory and Practice of Finite Elements*. Vol. 159. Applied Mathematical Sciences. Springer, New York, 2004.

[37] C. Förster. “Robust methods for fluid-structure interaction with stabilised finite elements.” PhD thesis. Universität Stuttgart, 2007.

[38] C. Förster, W. A. Wall, and E. Ramm. “Artificial added mass instabilities in sequential staggered coupling of nonlinear structures and incompressible viscous flows.” In: *Computer Methods in Applied Mechanics and Engineering* 196 (2007), pp. 1278–1293. DOI: 10.1016/j.cma.2006.09.002.

[39] M. Frigo and S.G. Johnson. “The design and implementation of FFTW3.” In: *Proceedings of the IEEE* 93 (2005), pp. 216–231. DOI: 10.1109/JPROC.2004.840301.

[40] P. Gamnitzer, V. Gravemeier, and W. A. Wall. “Time-dependent subgrid scales in residual-based large eddy simulation of turbulent channel flow.” In: *Computer Methods in Applied Mechanics and Engineering* 199 (2010), pp. 819–827. DOI: 10.1016/j.cma.2009.07.009.

[41] J. R. Garratt. “The internal boundary layer - a review.” In: *Boundary-Layer Meteorology* 50 (1990), pp. 171–203. DOI: 10.1007/BF00120524.

[42] I. E. Garrick and W. H. Reed III. “Historical development of aircraft flutter.” In: *AIAA Journal* 18 (1981), pp. 897–912. DOI: 10.2514/3.57579.

[43] S. Gavrilakis. “Numerical simulation of low-Reynolds-number turbulent flow through a straight square duct.” In: *Journal of Fluid Mechanics* 244 (1992), pp. 101–129. DOI: 10.1017/S0022112092002982.

[44] B. Gong, Z. Wang, Z. Li, J. Zhang, and X. Fu. “Field measurements of boundary layer wind characteristics and wind loads of a parabolic trough solar collector.” In: *Solar Energy* 86 (2012), pp. 1880–1898. DOI: 10.1016/j.solener.2012.02.036.

[45] B. Hajra, G. Bitsuamlak, H. Aboshosha, and A. Elshaer. “Large eddy simulation of wind induced loads on a low rise building with complex roof geometry.” In: *Annual Conference of the Canadian Society for Civil Engineering*. London, 2016.

[46] M. Heil, A. L. Hazel, and J. Boyle. “Solvers for large-displacement fluid-structure interaction problems: segregated versus monolithic approaches.” In: *Computational Mechanics* 43 (2008), pp. 91–101. DOI: 10.1007/s00466-008-0270-6.

[47] N. Hosoya, J. A. Peterka, R. C. Gee, and D. Kearney. *Wind Tunnel Tests of Parabolic Trough Solar Collectors*. Tech. rep. NREL/SR-550-32282. National Renewable Energy Laboratory, 2008.

[48] G. Huang, H. Huang, and J. Guo. “A mesh deformation technique based on two-step solution of the elasticity equations.” In: *Computational Mechanics* 59 (2017), pp. 685–692. DOI: 10.1007/s00466-016-1367-y.

[49] S. H. Huang, Q. S. Li, and J. R. Wu. “A general inflow turbulence generator for large eddy simulation.” In: *Journal of Wind Engineering and Industrial Aerodynamics* 98 (2010), pp. 600–617. DOI: 10.1016/j.jweia.2010.06.002.

[50] T.J.R. Hughes. “Analysis of Transient Algorithms with Particular Reference to Stability Behavior.” In: *Computational Methods for Transient Analysis*. Ed. by T. Belytschko and T.J.R. Hughes. North-Holland, 1983, pp. 67–155.

[51] T.J.R. Hughes. “Multiscale phenomena: Green’s functions, the Dirichlet-to-Neumann formulation, subgrid scale models, bubbles and the origins of stabilized methods.” In: *Computer Methods in Applied Mechanics and Engineering* 127 (1995), pp. 387–401. DOI: 10.1016/0045-7825(95)00844-9.

[52] B. M. Irons and R. C. Tuck. “A version of the Aitken accelerator for computer iteration.” In: *International Journal for Numerical Methods in Engineering* 1 (1969), pp. 275–277. DOI: 10.1002/nme.1620010306.

[53] M.M. Joosten, W.G. Dettmer, and D. Perić. “On the temporal stability and accuracy of coupled problems with reference to fluid-structure interaction.” In: *International Journal for Numerical Methods in Fluids* 64 (2010), pp. 1363–1378. DOI: 10.1002/fld.2333.

[54] S. Jovic and D. M. Driver. *Backward-Facing Step Measurements at Low Reynolds Number, $Re_h = 5000$*. Tech. rep. NASA TM 108807. Ames Research Center, California, 1994.

[55] JR3. *Multi-Axis Load Cell Technologies*. URL: http://www.jr3.com. 2015.

[56] J. C. Kaimal, J. C. Wyngaard, Y. Izumi, and O. R. Coté. “Spectral characteristics of surface-layer turbulence.” In: *Quarterly Journal of the Royal Meteorological Society* 98 (1972), pp. 563–589. DOI: 10.1002/qj.49709841707.

[57] J.C. Kaimal and J.J. Finnigan. *Atmospheric Boundary Layer Flows: Their Structure and Measurement*. Oxford University Press, New York, 1994.

[58] T. von Kármán. “Progress in the statistical theory of turbulence.” In: *Proceedings of the National Academy of Sciences of the United States of America* 34 (1948), pp. 530–539.

[59] M. Kasperski and H.-J. Niemann. “The L.R.C. (load-response-correlation) - method: a general method of estimating unfavourable wind load distributions for linear and non-linear structural behaviour.” In: *Journal of Wind Engineering and Industrial Aerodynamics* 43 (1992), pp. 1753–1763. DOI: 10.1016/0167-6105(92)90588-2.

[60] S. Kawai and J. Larsson. “Wall-modeling in large eddy simulation: length scales, grid resolution, and accuracy.” In: *Physics of Fluids* 24 (2012), p. 015105. DOI: 10.1063/1.3678331.

[61] Kjkolb. *Parabolic trough solar thermal electric power plant at Kramer Junction*. https://commons.wikimedia.org (CC By 2.5), accessed 14-12-2017. 2005.

[62] D.A. Köse and E. Dick. “Prediction of the pressure distribution on a cubical building with implicit LES.” In: *Journal of Wind Engineering and Industrial Aerodynamics* 98 (2010), pp. 628–649. DOI: 10.1016/j.jweia.2010.06.004.

[63] U. Küttler and W. A. Wall. “Fixed-point fluid-structure interaction solvers with dynamic relaxation.” In: *Computational Mechanics* 43 (2008), pp. 61–72. DOI: 10.1007/s00466-008-0255-5.

[64] K.C.S. Kwok. “Wind-Induced Vibrations of Structures: With Special Reference to Tall Building Aerodynamics.” In: *Advanced Structural Wind Engineering*. Ed. by Y. Tamura and A. Kareem. Springer, Japan, 2014, pp. 121–155. DOI: 10.1007/978-4-431-54337-4_5.

[65] H. Lamb. *Hydrodynamics*. Cambridge University Press, Cambridge, 1993.

[66] H. Lamb. “On the vibrations of an elastic plate in contact with water.” In: *Proceedings of the Royal Society A* 98 (1920), pp. 205–216. DOI: 10.1098/rspa.1920.0064.

[67] H. Lettau. “Note on aerodynamic roughness-parameter estimation on the basis of roughness-element description.” In: *Journal of Applied Meteorology* 8 (1969), pp. 828–832. DOI: 10.1175/1520-0450(1969)008<0828:NOARPE>2.0.CO;2.

[68] C.L. Lu, Q.S. Li, S.H. Huang, F.B. Chen, and X.Y. Fu. “Large eddy simulation of wind effects on a long-span complex roof structure.” In: *Journal of Wind Engineering and Industrial Aerodynamics* 100 (2012), pp. 1–18. DOI: 10.1016/j.jweia.2011.10.006.

[69] E. Lüpfert, M. Geyer, W. Schiel, A. Esteban, R. Osuna, E. Zarza, and P. Nava. “Eurotrough design issues and prototype testing at PSA.” In: *Proceedings of the ASME International Solar Energy Conference - Forum 2001, Solar Energy: The Power to Choose*. Ed. by R. Campbell-Howe. Washington, DC, April 21-25, 2001, pp. 389–394.

[70] J. Mann. “The spatial structure of neutral atmospheric surface-layer turbulence.” In: *Journal of Fluid Mechanics* 273 (1994), pp. 141–168. DOI: 10.1017/S0022112094001886.

[71] J. Mann. “Wind field simulation.” In: *Probabilistic Engineering Mechanics* 13 (1998), pp. 269–282. DOI: 10.1016/S0266-8920(97)00036-2.

[72] A. Michalski. “Numerische Simulation leichter Flächentragwerke in einer numerisch generierten atmosphärischen Grenzschicht.” PhD thesis. Technische Universität München, 2010.

[73] A. Michalski, P. D. Kermel, E. Haug, R. Löhner, R. Wüchner, and K.-U. Bletzinger. “Validation of the computational fluid-structure interaction simulation at real-scale tests of a flexible 29 m umbrella in natural wind flow.” In: *Journal of Wind Engineering and Industrial Aerodynamics* 99 (2011), pp. 400–413. DOI: 10.1016/j.jweia.2010.12.010.

[74] M. Mier-Torrecilla, E. Herrera, and M. Doblaré. “Numerical calculation of wind loads over solar collectors.” In: *Energy Procedia* 49 (2014), pp. 163–173.

[75] T. Miyata. “Historical view of long-span bridge aerodynamics.” In: *Journal of Wind Engineering and Industrial Aerodynamics* 91 (2003), pp. 1393–1410. DOI: 10.1016/j.jweia.2003.09.033.

[76] S. Murakami. “Overview of turbulence models applied in CWE-1997.” In: *Journal of Wind Engineering and Industrial Aerodynamics* 74-76 (1998), pp. 1–24. DOI: 10.1016/S0167-6105(98)00004-X.

[77] E. Naudascher and D. Rockwell. *Flow-Induced Vibrations: An Engineering Guide*. Balkema, Rotterdam, 1994.

[78] A.W. Naylor and G.R. Sell. *Linear Operator Theory in Engineering and Science*. Vol. 40. Applied Mathematical Sciences. Springer, New York, 1982.

[79] N.M. Newmark. "A method of computation for structural dynamics." In: *Journal of the Engineering Mechanics Division* 85 (1959), pp. 67–94.

[80] K. Nozawa and T. Tamura. "Numerical prediction of pressure on a high-rise building immersed in a turbulent boundary layer using LES." In: *Summaries to Technical Papers of Annual Meeting, Japan Association for Wind Engineering* (2003), pp. 84–84. DOI: 10.14887/jaweam.2003.0.84.0.

[81] K.C. Park and C.A. Felippa. "Partitioned Analysis of Coupled Systems." In: *Computational Methods for Transient Analysis*. Ed. by T. Belytschko and T.J.R. Hughes. North-Holland, 1983, pp. 157–219.

[82] G. Parkinson. "Phenomena and modelling of flow-induced vibrations of bluff bodies." In: *Progress in Aerospace Sciences* 26 (1989), pp. 169–224. DOI: 10.1016/0376-0421(89)90008-0.

[83] J. Principe, R. Codina, and F. Henke. "The dissipative structure of variational multiscale methods for incompressible flows." In: *Computer Methods in Applied Mechanics and Engineering* 199 (2010), pp. 791–801. DOI: 10.1016/j.cma.2008.09.007.

[84] A. Prosperetti. "Viscous effects on small-amplitude surface waves." In: *Physics of Fluids* 19 (1976), pp. 195–203. DOI: 10.1063/1.861446.

[85] P. Råback, J. Ruokolainen, M. Lyly, and E. Järvinen. "Fluid-structure interaction boundary conditions by artificial compressibility." In: *ECCOMAS Computational Fluid Dynamics Conference*. Swansea, 2001.

[86] D. E. Randall, D. D. McBride, and R. E. Tate. *Steady-State Wind Loading on Parabolic-Trough Solar Collectors*. Tech. rep. SAND 79-2134. Sandia National Laboratories, 1980.

[87] M. Ricci, L. Patruno, I. Kalkman, B. Blocken, and S. Miranda. "Large eddy simulation for wind loads assessment: benchmark on a high-rise building." In: *7th European and African Conference on Wind Engineering*. Liège, 2017.

[88] M. Ricci, L. Patruno, and S. Miranda. "Wind loads and structural response: benchmarking LES on a low-rise building." In: *Engineering Structures* 144 (2017), pp. 26–42. DOI: 10.1016/j.engstruct.2017.04.027.

[89] E. J. Roschke. *Wind Loading on Solar Concentrators: Some General Considerations*. Tech. rep. NASA-CR-173896. 1984.

[90] R. Rossi, M. Lazzari, and R. Vitaliani. "Wind field simulation for structural engineering purposes." In: *International Journal for Numerical Methods in Engineering* 61 (2004), pp. 738–763. DOI: 10.1002/nme.1083.

[91] H. Ruscheweyh. Personal Communication. 2017.

[92] H. Ruscheweyh and T. Polyzoides. "Wirbelerregte Schwingung einer dreieckigen Anzeigetafel." In: *Windingenieurtechnik - Vom Bauteilnachweis bis zum Stadtklima*. Ed. by M. Krafczyk and H. Ruscheweyh. Vol. 14. WtG-Berichte. Windtechnologische Gesellschaft e.V., 2015, pp. 159–165.

[93] P.B. Ryzhakov, R. Rossi, S.R. Idelsohn, and E. Oñate. "A monolithic Lagrangian approach for fluid-structure interaction problems." In: *Computational Mechanics* 46 (2010), pp. 883–899. DOI: 10.1007/s00466-010-0522-0.

[94] J.W. Saunders and W.H. Melbourne. "Tall rectangular building response to cross-wind excitation." In: *Proceedings of the Fourth International Conference on Wind Effects on Buildings and Structures*. Ed. by K.J. Eaton. Heathrow: Cambridge University Press, 1975, pp. 369–379.

[95] R. H. Scanlan. "Aeroelastic simulation of bridges." In: *Journal of Structural Engineering* 109 (1983), pp. 2829–2837. DOI: 10.1061/(ASCE)0733-9445(1983)109:12(2829).

[96] R. H. Scanlan. "The action of flexible bridges under wind, I: flutter theory." In: *Journal of Sound and Vibration* 60 (1978), pp. 187–199.

[97] H. Schlichting. *Boundary-Layer Theory*. 7th. McGraw-Hill, 1979.

[98] T.-H. Shih, L. A. Povinelli, N.-S. Liu, M. G. Potapczuk, and J. L. Lumley. *A generalized wall function*. Tech. rep. NASA/TM-1999-209398. 1999.

[99] O.K. Smith. "Eigenvalues of a symmetric 3 x 3 matrix." In: *Communications of the ACM* 4 (1961), p. 168. DOI: 10.1145/355578.366316.

[100] P.R. Spalart. "Detached-eddy simulation." In: *Annual Review of Fluid Mechanics* 41 (2009), pp. 181–202. DOI: 10.1146/annurev.fluid.010908.165130.

[101] P.R. Spalart. *Young Person's Guide to Detached-Eddy Simulation Grids*. Tech. rep. NASA/CR-2001-211032. Langley Research Center, Hampton, 2001.

[102] P.R. Spalart, W.-H. Jou, M. Strelets, and S.R. Allmaras. "Comments on the feasibility of LES for wings, and on a hybrid RANS/LES approach." In: *Advances in DNS/LES*. Ed. by C. Liu and Z. Liu. Greyden Press, Columbus, 1997, pp. 137–147.

[103] K. Stein, T. Tezduyar, and R. Benney. "Mesh moving techniques for fluid-structure interactions with large displacements." In: *Journal of Applied Mechanics* 70 (2003), pp. 58–63. DOI: 10.1115/1.1530635.

[104] E. Süli and D. Mayers. *An Introduction to Numerical Analysis*. Cambridge University Press, Cambridge, 2003. ISBN: 978-0-521-81026-5.

[105] H. Sun, B. Gong, and Q. Yao. "A review of wind loads on heliostats and trough collectors." In: *Renewable and Sustainable Energy Reviews* 32 (2014), pp. 206–221. DOI: 10.1016/j.rser.2014.01.032.

[106] G. R. Tabor and M. H. Baba-Ahmadi. "Inlet conditions for large eddy simulation: a review." In: *Computers and Fluids* 39 (2010), pp. 553–567. DOI: 10.1016/j.compfluid.2009.10.007.

[107] T. Tamura, K. Nozawa, and K. Kondo. "AIJ guide for numerical prediction of wind loads on buildings." In: *Journal of Wind Engineering and Industrial Aerodynamics* 96 (2008), pp. 1974–1984. DOI: 10.1016/j.jweia.2008.02.020.

[108] H. Tanaka, N. Konno, K. Ohtake, and N. Tsuchiya. *Prediction accuracy of wind forces acting on high-rise buildings in urban areas by large eddy simulation*. The Sixth International Symposium on Computational Wind Engineering, Hamburg. 2014.

[109] G.I. Taylor. "The spectrum of turbulence." In: *Proceedings of the Royal Society A* 164 (1938), pp. 476–490. DOI: 10.1098/rspa.1938.0032.

[110] J. M. Terres-Nicoli, C. Mans, S. Farquhar, and G. A. Kopp. *Study of wind effects on the isolated parabolic collector*. Internal Report for Abengoa. 2013.

[111] The HDF Group. Hierarchical data format version 5, 2000-2018. http://www.hdfgroup.org/HDF5.

[112] A.A. Townsend. *The structure of turbulent shear flow*. 2nd. Cambridge University Press, Cambridge, 1976.

[113] S. Turek and J. Hron. "Proposal for numerical benchmarking of fluid-structure interaction between an elastic object and laminar incompressible flow." In: *Fluid-Structure Interaction: Modelling, Simulation, Optimisation*. Ed. by H.-J. Bungartz and M. Schäfer. Vol. 53. Lecture Notes in Computational Science and Engineering. Springer, 2006.

[114] I. Van der Hoven. "Power spectrum of horizontal wind speed in the frequency range from 0.0007 to 900 cycles per hour." In: *Journal of Meteorology* 14 (1957), pp. 160–164. DOI: 10.1175/1520-0469(1957)014<0160:PSOHWS>2.0.CO;2.

[115] P. P. Van, T. Nozu, H. Kikuchi, K. Hibi, and Y. Tamura. "Local wind pressure distributions on a building with a setback obtained by large eddy simulations." In: *Proceedings of National Symposium On Wind Engineering, Japan* 22 (2012), pp. 359–364. DOI: 10.14887/kazekosymp.22.0.359.0.

[116] K. Wang and T. Stathopoulos. "Exposure model for wind loading of buildings." In: *Journal of Wind Engineering and Industrial Aerodynamics* 95 (2007), pp. 1511–1525. DOI: 10.1016/j.jweia.2007.02.016.

[117] M. Wang and P. Moin. “Dynamic wall modeling for large-eddy simulation of complex turbulent flows.” In: *Physics of Fluids* 14 (2002), p. 2043. DOI: 10.1063/1.1476668.

[118] H. Werner and H. Wengle. *Large-eddy simulation of turbulent flow over and around a cube in a plate channel*. The Eighth International Symposium on Turbulent Shear Flows, Munich. 1991.

[119] J. Wieringa. “Representative roughness parameters for homogeneous terrain.” In: *Boundary-Layer Meteorology* 63 (1993), pp. 323–363. DOI: 10.1007/BF00705357.

[120] A. Winterstein (geb. Mini). “Implementation and evaluation of mesh-updating strategies for computational fluid-structure interaction.” MA thesis. Technische Universität München, 2014.

[121] L.R. Wootton. “The oscillations of large circular stacks in wind.” In: *Proceedings of the Institution of Civil Engineers* 43 (1969), pp. 573–598. DOI: 10.1680/iicep.1969.7314.

Bisherige Titel der Schriftenreihe

Band	Titel
1	Frank Koschnick, *Geometrische Lockingeffekte bei Finiten Elementen und ein allgemeines Konzept zu ihrer Vermeidung*, 2004.
2	Natalia Camprubi, *Design and Analysis in Shape Optimization of Shells*, 2004.
3	Bernhard Thomee, *Physikalisch nichtlineare Berechnung von Stahlfaserbetonkonstruktionen*, 2005.
4	Fernaß Daoud, *Formoptimierung von Freiformschalen - Mathematische Algorithmen und Filtertechniken*, 2005.
5	Manfred Bischoff, *Models and Finite Elements for Thin-walled Structures*, 2005.
6	Alexander Hörmann, *Ermittlung optimierter Stabwerkmodelle auf Basis des Kraftflusses als Anwendung plattformunabhängiger Prozesskopplung*, 2006.
7	Roland Wüchner, *Mechanik und Numerik der Formfindung und Fluid-Struktur-Interaktion von Membrantragwerken*, 2006.
8	Florian Jurecka, *Robust Design Optimization Based on Metamodeling Techniques*, 2007.
9	Johannes Linhard, *Numerisch-mechanische Betrachtung des Entwurfsprozesses von Membrantragwerken*, 2009.
10	Alexander Kupzok, *Modeling the Interaction of Wind and Membrane Structures by Numerical Simulation*, 2009.
11	Bin Yang, *Modified Particle Swarm Optimizers and their Application to Robust Design and Structural Optimization*, 2009.

Band	Titel
12	Michael Fleischer, *Absicherung der virtuellen Prozesskette für Folgeoperationen in der Umformtechnik*, 2009.
13	Amphon Jrusjrungkiat, *Nonlinear Analysis of Pneumatic Membranes - From Subgrid to Interface*, 2009.
14	Alexander Michalski, *Simulation leichter Flächentragwerke in einer numerisch generierten atmosphärischen Grenzschicht*, 2010.
15	Matthias Firl, *Optimal Shape Design of Shell Structures*, 2010.
16	Thomas Gallinger, *Effiziente Algorithmen zur partitionierten Lösung stark gekoppelter Probleme der Fluid-Struktur-Wechselwirkung*, 2011.
17	Josef Kiendl, *Isogeometric Analysis and Shape Optimal Design of Shell Structures*, 2011.
18	Joseph Jordan, *Effiziente Simulation großer Mauerwerksstrukturen mit diskreten Rissmodellen*, 2011.
19	Albrecht von Boetticher, *Flexible Hangmurenbarrieren: Eine numerische Modellierung des Tragwerks, der Hangmure und der Fluid-Struktur-Interaktion*, 2012.
20	Robert Schmidt, *Trimming, Mapping, and Optimization in Isogeometric Analysis of Shell Structures*, 2013.
21	Michael Fischer, *Finite Element Based Simulation, Design and Control of Piezoelectric and Lightweight Smart Structures*, 2013.
22	Falko Hartmut Dieringer, *Numerical Methods for the Design and Analysis for Tensile Structures*, 2014.
23	Rupert Fisch, *Code Verification of Partitioned FSI Environments for Lightweight Structures*, 2014.
24	Stefan Sicklinger, *Stabilized Co-Simulation of Coupled Problems Including Fields and Signals*, 2014.

Band	Titel
25	Madjid Hojjat, *Node-based parametrization for shape optimal design*, 2015.
26	Ute Israel, *Optimierung in der Fluid-Struktur-Interaktion - Sensitivitätsanalyse für die Formoptimierung auf Grundlage des partitionierten Verfahrens*, 2015.
27	Electra Stavropoulou, *Sensitivity analysis and regularization for shape optimization of coupled problems*, 2015.
28	Daniel Markus, *Numerical and Experimental Modeling for Shape Optimization of Offshore Structures*, 2015.
29	Pablo Suárez, *Design Process for the Shape Optimization of Pressurized Bulkheads as Components of Aircraft Structures*, 2015.
30	Armin Widhammer, *Variation of Reference Strategy - Generation of Optimized Cutting Patterns for Textile Fabrics*, 2015.
31	Helmut Masching, *Parameter Free Optimization of Shape Adaptive Shell Structures*, 2016.
32	Hao Zhang, *A General Approach for Solving Inverse Problems in Geophysical Systems by Applying Finite Element Method and Metamodel Techniques*, 2016.
33	Tianyang Wang, *Development of Co-Simulation Environment and Mapping Algorithms*, 2016.
34	Michael Breitenberger, *CAD-integrated Design and Analysis of Shell Structures*, 2016.
35	Önay Can, *Functional Adaptation with Hyperkinematics using Natural Element Method: Application for Articular Cartilage*, 2016.
36	Benedikt Philipp, *Methodological Treatment of Non-linear Structural Behavior in the Design, Analysis and Verification of Lightweight Structures*, 2017.